

**MANIPULATION OF ZEOLITE ACTIVE SITE ACIDITY  
AND ATOMIC STRUCTURE TO CONTROL  
HYDROCARBON CONVERSION AND SELECTIVITY**

by

Edward P. Schreiner

A dissertation submitted to the Faculty of the University of Delaware in partial fulfillment of the requirements for the degree of Doctor of Philosophy in Chemical Engineering

Fall 2017

© 2017 Edward P. Schreiner  
All Rights Reserved

**MANIPULATION OF ZEOLITE ACTIVE SITE ACIDITY  
AND ATOMIC STRUCTURE TO CONTROL  
HYDROCARBON CONVERSION AND SELECTIVITY**

by

Edward P. Schreiner

Approved: \_\_\_\_\_  
Eric M. Furst, Ph.D.  
Chair of the Department of Chemical and Biomolecular Engineering

Approved: \_\_\_\_\_  
Babatunde A. Ogunnaike, Ph.D.  
Dean of the College of Engineering

Approved: \_\_\_\_\_  
Ann L. Ardis, Ph.D.  
Senior Vice Provost for Graduate and Professional Education

I certify that I have read this dissertation and that in my opinion it meets the academic and professional standard required by the University as a dissertation for the degree of Doctor of Philosophy.

Signed:

---

Raul F. Lobo, Ph.D.  
Professor in charge of dissertation

I certify that I have read this dissertation and that in my opinion it meets the academic and professional standard required by the University as a dissertation for the degree of Doctor of Philosophy.

Signed:

---

Dionisios G. Vlachos, Ph.D.  
Member of dissertation committee

I certify that I have read this dissertation and that in my opinion it meets the academic and professional standard required by the University as a dissertation for the degree of Doctor of Philosophy.

Signed:

---

Bingjun Xu, Ph.D.  
Member of dissertation committee

I certify that I have read this dissertation and that in my opinion it meets the academic and professional standard required by the University as a dissertation for the degree of Doctor of Philosophy.

Signed:

---

Robert J. Kee, Ph.D.  
Member of dissertation committee

## ACKNOWLEDGMENTS

This thesis is the culmination of five years of learning and research in the Department of Chemical and Biomolecular Engineering at the University of Delaware. This work could not have been accomplished without the help, guidance, and support of others. There are many individuals that have been influential in my education and this thesis and I would like to express my gratitude for everything they have done for me.

I would like to thank my advisor, Dr. Raul Lobo, for his guidance throughout my graduate studies. I started my graduate studies without any knowledge of zeolites, but he taught me the intricacies of zeolite synthesis, characterization, alteration, and application as catalysts. I cannot adequately express my gratitude for your support and guidance during my time in the research group.

I would like to thank my committee members: Dr. Dionisios Vlachos, Dr. Bingjun Xu, and Dr. Robert Kee. Dr. Vlachos and Dr. Kee have been involved in my research from the beginning, working as members of the Air Force endothermic cooling initiative. Their intellectual guidance throughout that project has been influential to the work in this thesis. Dr. Xu joined our department when I did, and I am thankful for his insights as I have grown throughout my time in the program.

I would like to thank our collaborators on the Air Force endothermic cooling project. These include Dr. Stavros Caratzoulas and Andrew Black at the University of Delaware; the Dean, Kee, and Bogin groups at Colorado School of Mines; and Susanne Opalka, Tianli Zhu, and Meredith Colket at United Technologies Research

Center. Your feedback and advice have been instrumental to the production of this thesis.

I would like to acknowledge the Air Force Office of Scientific Research and the Department of Energy for funding the research that led to the production of this thesis.

I would like to thank the members of the Lobo group throughout the years: fellow graduate students Dr. Trong Pham, Dr. Jang Ho Yun, Dr. Jason Loiland, Dr. Bahar Ipek, Dr. Maura Koehle, Huibo Sheng, Hannah Nguyen, Trishelle Copland-Johnson, Chen-Yu Chou, and Muyuan Li, and postdoctoral researchers Dr. Weiqing Zheng, Dr. Qingling Liu, Dr. Adriana Aristizabal Castrillon, Dr. Na Ji, Dr. Matthew Wulfers, Dr. Shewangizaw Teketel, Dr. Marta Leon Garcia, Dr. Takahiko Moteki, Dr. Jelvehnaz Mirzababaei, Dr. Young Jin Kim, Dr. Ali Mehdad, Dr. Erisa Saraci, Dr. Efterpi Vasileiadou, and Dr. Ting Jiang. Specifically, I want to acknowledge the two postdoctoral researches who taught me many of the laboratory techniques used to complete this thesis: Dr. Matt Wulfers and Dr. Shewa Teketel. I am thankful for your guidance and patience when I was a greenhorn. I could not have completed this thesis without your help. I also want to acknowledge my fellow classmates, Molly and Huibo, for your companionship throughout our time in the Lobo group. It was an enjoyable experience to share with you.

I would like to thank my fellow graduate students that have aided me in my research that has led to this thesis. Brian Murphy and Matthew Gilkey have provided support in GC/MS acquisition and analysis, as well as intellectual discussion.

I would like to thank the support staff within the Department of Chemical and Biomolecular Engineering at the University of Delaware. George Whitmyre, Gary

Wellmaker, Alan Price, Neilsen Garrett, and Weihau Deng have been instrumental in setting up laboratories and experimental set ups. Rechilda Alba, Mary Walsh, and Kathleen Young have been so helpful throughout my time in the department. Our staff is excellent and deserves commendation for the support they provide for the department.

I would like to thank my fellow members of the Class of 2017 and other friends in the department I have gained throughout the years. It seems that many of my fondest memories center around food, from cookouts to potlucks, but these are memories I will never forget. I look forward to our continued friendship and seeing you all again in the future.

Finally, I would like to thank my family for their continued support, especially those who were able to attend my hooding ceremony: my Aunts Sis, Marie, and Helen, my Uncle Chip, my grandfather and grandmother, my Uncle Barry, Ray and Allena, and Michael Sloan, who is like a brother to me). My parents have always been supportive of my ambitions and for that, I am forever grateful. From giving me K'NEX sets and Legos to sending me to robotics camps as a child, without that continuous intellectual stimulation, I would have never attained the goals that I have to this day.

## TABLE OF CONTENTS

LIST OF TABLES .....	xi
LIST OF FIGURES .....	xii
ABSTRACT .....	xix

### Chapter

1	INTRODUCTION .....	1
1.1	Hydrocarbon Conversion Processes .....	1
1.1.1	Upgrading Petroleum Oil .....	3
1.1.2	Upgrading Natural Gas .....	3
1.1.3	Upgrading Bio-based Sources .....	4
1.1.4	Synthesis Gas .....	6
1.2	Hydrocarbon Conversion Catalysis .....	6
1.2.1	Zeolites and Other Crystalline Molecular Sieves .....	8
1.2.2	Zeolite Synthesis .....	9
1.2.3	Zeolite Catalysis .....	11
1.3	Challenges in Modern Catalysis .....	14
1.4	Scope of this Thesis .....	15
2	EXPERIMENTAL TECHNIQUES .....	18
2.1	Catalyst Characterization .....	18
2.1.1	Powder X-ray Diffraction .....	18
2.1.2	Solid State Nuclear Magnetic Resonance Spectroscopy (SSNMR) .....	20
2.1.3	Ultraviolet-Visible Spectroscopy (UV/Vis) .....	23
2.1.4	Infrared Spectroscopy .....	23
2.1.5	X-ray Fluorescence Spectroscopy .....	24
2.1.6	X-ray Absorption Spectroscopy .....	25
2.1.7	Scanning Electron Microscopy .....	26
2.1.8	Sample Texture Analysis .....	27

2.1.9	Inductively Coupled Plasma Atomic Emission Spectroscopy ....	28
2.2	Catalyst Testing.....	28
2.2.1	Flow Reactor Design .....	28
2.2.2	Design Safety Considerations.....	31
2.2.3	Chromatography .....	31
2.2.4	Mass Spectrometry .....	34
3	CATALYTIC <i>n</i> -PENTANE CONVERSION ON H-ZSM-5 AT HIGH PRESSURE .....	35
3.1	Introduction .....	35
3.2	Experimental Section.....	39
3.2.1	Materials .....	39
3.2.2	Characterization.....	39
3.2.3	Catalytic Testing.....	40
3.3	Results .....	41
3.3.1	Catalyst Characterization.....	41
3.3.2	Catalytic Conversion of <i>n</i> -Pentane .....	43
3.4	Discussion.....	46
3.5	Conclusions .....	53
4	HIGH-PRESSURE CATALYTIC DEHYDROGENATION OF ALKANES ON MOLYBDENUM CARBIDE SUPPORTED ON METAL OXIDES AND LOW-ACIDITY ZEOLITES .....	54
4.1	Introduction .....	54
4.2	Experimental Section.....	57
4.2.1	Materials .....	57
4.2.2	Characterization.....	60
4.2.3	Catalytic Tests .....	61
4.3	Results .....	62
4.3.1	Zeolite Characterization .....	62
4.3.2	Catalyst Screening.....	65
4.3.3	Catalytic Dehydrogenation of <i>n</i> -Pentane.....	67
4.3.4	Catalytic Dehydrogenation of <i>n</i> -Hexane and <i>n</i> -Heptane.....	69

4.4	Discussion.....	70
4.5	Conclusion.....	76
5	METHANOL CONVERSION TO HYDROCARBONS ON FERRISILICATE [FE]BETA .....	78
5.1	Introduction .....	78
5.2	Experimental Section.....	85
5.2.1	Materials .....	85
5.2.2	Characterization.....	87
5.2.3	Catalytic Testing.....	87
5.3	Results .....	89
5.3.1	Catalyst Characterization.....	89
5.3.2	Catalytic Testing.....	92
5.4	Discussion.....	99
5.5	Conclusion.....	107
6	RECOMMENDATIONS AND CONCLUSIONS.....	109
6.1	Suggestions for Future Work.....	110
6.1.1	Enhancing Aircraft Endothermic Cooling.....	110
6.1.1.1	Selective Heteroatom Site Incorporation.....	113
6.1.2	Further Improvements on Mo/H-[B]ZSM-5 .....	115
6.1.2.1	Active Site Structure Elucidation .....	115
6.1.2.2	Alternative Applications.....	118
6.1.3	Increasing Yield of Heavier Hydrocarbons in MTO.....	118
6.1.4	Identifying Species Produced during Dimethyl Ether Conversion.....	120
6.2	Concluding Remarks .....	121
	REFERENCES .....	123

## Appendix

A	DETAILED PRODUCT SELECTIVITY FOR <i>n</i> -PENTANE CONVERSION ON H-[Al]ZSM-5 .....	135
B	X-RAY DIFFRACTION PATTERNS AND SEM IMAGES OF BOROSILICATES .....	137
C	GAS CHROMATOGRAPHY / MASS SPECTROMETRY OF DME CONVERSION ON H-[Fe]BETA.....	144
D	REPRODUCTION OF MATERIAL RIGHTS .....	164

## LIST OF TABLES

Table 4.1: Si/B ratios and micropore volumes of zeolite supports; samples with F-1/F-2 and OH-1/OH-2 indicate synthesized in fluoride and hydroxide media respectively .....	63
Table 4.2: Consumption of <i>n</i> -pentane and carbon selectivity to pentenes on different metal loadings of Mo/ $\gamma$ -Al <sub>2</sub> O <sub>3</sub> and Mo/H-[B]ZSM-5. Reaction conditions: $T = 723$ K, $P = 40$ bar, and $WHSV = 188 \text{ g}_{C5}\text{g}_{cat}^{-1}\text{h}^{-1}$ .....	66
Table 4.3: Consumption of <i>n</i> -pentane, <i>n</i> -hexane, and <i>n</i> -heptane and selectivity to primary dehydrogenation product and olefins lighter than the primary dehydrogenation products on Mo/H-[B]ZSM-5, Mo/ $\gamma$ -Al <sub>2</sub> O <sub>3</sub> , and Mo/[B]Beta. $T = 723$ K, $P = 40$ bar, $WHSV = 188 \text{ g}_{C5}/\text{g}_{cat}\text{-hr}$ , $196 \text{ g}_{C6}/\text{g}_{cat}\text{-hr}$ and $205 \text{ g}_{C7}/\text{g}_{cat}\text{-hr}$ .....	70
Table 5.1 Carbon selectivity and research octane number (RON) of species identified via GC/MS from DME conversion on H-[Fe]Beta. Reaction conditions: $T = 593$ K, $P = 1$ atm, $P_{DME} = 0.14$ atm, $F_{N2} = 60$ mL/min, and $WHSV =$ and $5.7 \text{ g}_{DME}\text{g}_{cat}^{-1}\text{h}^{-1}$ .....	100
Table 5.2: Comparison of carbon selectivity of dimethyl ether conversion on H-[Fe]Beta and H-[Al]Beta. Reaction conditions: <sup>a</sup> $T = 573$ K, $P = 1$ atm, $P_{DME} = 0.14$ atm, $F_{N2} = 60$ mL/min, and $WHSV = 11.3 \text{ g}_{DME}\text{g}_{cat}^{-1}\text{h}^{-1}$ and <sup>b</sup> $T = 473$ K, $P = 10$ atm, $P_{DME} = 1.2$ atm, $F_{N2} = 16.7$ mL/min, and $WHSV = 0.7 \text{ g}_{DME}\text{g}_{cat}^{-1}\text{h}^{-1}$ .....	102
Table A.1: Product carbon selectivity at 15 min time on stream from high pressure conversion of <i>n</i> -pentane on H-[Al]ZSM-5. Reaction conditions: $T = 633 - 723$ K, $P = 40$ bar, and $WHSV = 1120 \text{ g}_{C5}\text{g}_{cat}^{-1}\text{h}^{-1}$ .....	135
Table C.1: Carbon selectivity of species identified via GC/MS from DME conversion on H-[Fe]Beta. Reaction conditions: $T = 593$ K, $P = 1$ atm, $P_{DME} = 0.14$ atm, $F_{N2} = 60$ mL/min, and $WHSV =$ and $5.7 \text{ g}_{DME}\text{g}_{cat}^{-1}\text{h}^{-1}$ .....	144

## LIST OF FIGURES

Figure 1.1: Example of reactions used in hydrocarbon conversion processes .....	2
Figure 1.2: Example of fuels, chemicals, and materials produced from biomass through furanic intermediates.....	5
Figure 1.3: Hydrolysis of triglyceride to produce soaps (top) and transesterification of triglyceride to produce biodiesel (bottom).....	6
Figure 1.4: Palladium organometallic complex formed during aryl-aryl bond formation .....	7
Figure 1.5: Depiction of zeolite ZSM-5 channels with an approximate relationship to the size of benzene molecules .....	8
Figure 1.6: Example of siliceous framework (left), trivalent aluminum substitution into the zeolite framework creating a negatively charge framework accompanied by a proton for charge balance (middle), and tetravalent titanium substitution (right).....	9
Figure 1.7: Illustration of zeolite synthesis procedure .....	10
Figure 1.8: Transalkylation of toluene on H-[Al]ZSM-5 selectively producing <i>p</i> -xylene over <i>m</i> -xylene .....	12
Figure 1.9: Rate of methanol dehydration to dimethyl ether with varying heteroatom substitution in the zeolite framework. Reprinted from Journal of Catalysis, Vol. 312, A.J. Jones, R.T. Carr, S.I. Zones, and E. Iglesia, <i>Acid strength and solvation in catalysis by MFI zeolites and effects of the identity, concentration and location of framework heteroatoms</i> , 56-68, 2014, with permission from Elsevier [49].....	13
Figure 1.10: Comparison of aluminum and boron substituted into a zeolite framework .....	14
Figure 2.1: X-ray diffraction pattern of [Al]ZSM-5.....	19

Figure 2.2	$^{29}\text{Si}$ NMR of zeolite NaY that has been dehydrated, hydrated, or ion exchanged with ammonium nitrate (a, c, and e) and steam treated NaY under the same conditions (b, d, f). Reprinted from Microporous and Mesoporous Materials, Vol. 90, J. Jiao, W. Wang, B. Sulikowski, J. Weitkamp, and M. Hunger, <i><math>^{29}\text{Si}</math> and <math>^{27}\text{Al}</math> MAS NMR characterization of non-hydrated zeolites Y upon adsorption of ammonia</i> , 246-250, 2006, with permission from Elsevier. [60].....	21
Figure 2.3:	$^{27}\text{Al}$ NMR of zeolite NaY that has been dehydrated, hydrated, or ion exchanged with ammonium nitrate (a, c, and e) and steam treated NaY under the same conditions (b, d, f). Reprinted from Microporous and Mesoporous Materials, Vol. 90, J. Jiao, W. Wang, B. Sulikowski, J. Weitkamp, and M. Hunger, <i><math>^{29}\text{Si}</math> and <math>^{27}\text{Al}</math> MAS NMR characterization of non-hydrated zeolites Y upon adsorption of ammonia</i> , 246-250, 2006, with permission from Elsevier. [60].....	22
Figure 2.4:	IR spectra showing the O-H stretching bands of molybdenum impregnated ZSM-5 samples with different framework compositions...	24
Figure 2.5:	Example of XAS setup at a synchrotron light source ( <i>top</i> ) and XAS spectra of molybdenum carbide ( <i>bottom</i> ).....	26
Figure 2.6:	Process flow diagram of the experimental setup used for high pressure experiments .....	29
Figure 2.7:	Example of reactor tube containing catalyst packed bed.....	30
Figure 2.8:	Simplified schematic of gas chromatograph.....	32
Figure 2.9:	Example GC chromatogram from catalytic dehydrogenation of <i>n</i> -pentane using a polar alumina column for separation.....	33
Figure 3.1:	Simplified process flow diagram for proposed aircraft endothermic cooling .....	36
Figure 3.2:	SEM image of CBV3024E ( <i>top</i> ), $^{29}\text{Si}$ NMR ( <i>left</i> ), and $^{27}\text{Al}$ NMR ( <i>right</i> ) of the ZSM-5 catalyst. ....	42
Figure 3.3:	Conversion of <i>n</i> -pentane over 6.5 h time on stream during high pressure conversion on H-[Al]ZSM-5. Reaction conditions: $T = 633 - 723$ K, $P = 40$ bar, and $\text{WHSV} = 1120 \text{ g}_{\text{C5cat}}^{-1}\text{h}^{-1}$ .....	43

Figure 3.4: Conversion of <i>n</i> -pentane ( <i>left</i> ) and selectivity to product groups ( <i>right</i> ) during high pressure conversion on H-[Al]ZSM-5. Reaction conditions: $T = 633 - 723 \text{ K}$ , $P = 40 \text{ bar}$ , and $\text{WHSV} = 1120 \text{ g}_{\text{C}_5\text{g}_{\text{cat}}}^{-1}\text{h}^{-1}$ .....	44
Figure 3.5: Conversion of <i>n</i> -pentane ( <i>left</i> ) and selectivity to product groups ( <i>right</i> ) during high pressure conversion on H-[Al]ZSM-5. Reaction conditions: $T = 673 \text{ K}$ , $P = 10 - 60 \text{ bar}$ , and $\text{WHSV} = 1120 \text{ g}_{\text{C}_5\text{g}_{\text{cat}}}^{-1}\text{h}^{-1}$ .	45
Figure 3.6: Conversion of <i>n</i> -pentane ( <i>left</i> ) and selectivity to product groups ( <i>right</i> ) during high pressure conversion on H-[Al]ZSM-5. Reaction conditions: $T = 673 \text{ K}$ , $P = 40 \text{ bar}$ , and $\text{WHSV} = 375 - 1500 \text{ g}_{\text{C}_5\text{g}_{\text{cat}}}^{-1}\text{h}^{-1}$ .	46
Figure 3.7: Selectivity of products within the lights fraction at various temperatures ( <i>left</i> ), pressures ( <i>middle</i> ), and WHSV ( <i>right</i> ). Reaction conditions: $T = 633 - 723 \text{ K}$ , $P = 10 - 60 \text{ bar}$ , and $\text{WHSV} = 375 - 1500 \text{ g}_{\text{C}_5\text{g}_{\text{cat}}}^{-1}\text{h}^{-1}$ .....	49
Figure 3.8: Simplified reaction network demonstrating the production of propane and butane.....	50
Figure 3.9: Activation energies at 10 bar ( <i>square</i> ), 20 bar ( <i>circle</i> ), and 40 bar ( <i>triangle</i> ). Reaction conditions: $T = 633 - 673 \text{ K}$ , $P = 10 - 40 \text{ bar}$ , and $\text{WHSV} = 1120 \text{ g}_{\text{C}_5\text{g}_{\text{cat}}}^{-1}\text{h}^{-1}$ .....	52
Figure 4.1: SEM image of [B]ZSM-5 (OH-1) ( <i>top</i> ) and [B]ZSM-5 (F-1) ( <i>bottom</i> ) ....	64
Figure 4.2: Consumption of <i>n</i> -pentane ( <i>left</i> ) and carbon selectivity to pentenes ( <i>right</i> ) on various molybdenum carbide catalysts (5.8% Mo/support). Reaction conditions: $T = 723 \text{ K}$ , $P = 40 \text{ bar}$ , and $\text{WHSV} = 188 \text{ g}_{\text{C}_5\text{g}_{\text{cat}}}^{-1}\text{h}^{-1}$ .....	65
Figure 4.3: Consumption of <i>n</i> -pentane ( <i>checkered</i> ) and production of pentenes ( <i>white</i> ) on Mo/H-[B]ZSM-5 with different Si/B ratios. Reaction conditions: $T = 673 - 798 \text{ K}$ , $P = 40 \text{ bar}$ , and $\text{WHSV} = 188 \text{ g}_{\text{C}_5\text{g}_{\text{cat}}}^{-1}\text{h}^{-1}$ .	67
Figure 4.4: Consumption of <i>n</i> -pentane ( <i>left</i> ) and production of pentenes ( <i>right</i> ) on unloaded supports and Mo/H-[B]ZSM-5. Reaction conditions: $T = 673 - 798 \text{ K}$ , $P = 40 \text{ bar}$ , and $\text{WHSV} = 188 \text{ g}_{\text{C}_5\text{g}_{\text{cat}}}^{-1}\text{h}^{-1}$ .....	68
Figure 4.5: Consumption of <i>n</i> -pentane and production of pentenes on Mo/H-[B]ZSM-5 during varying pressures ( <i>left</i> ) and space velocities ( <i>right</i> ). Reaction conditions: $T = 723 \text{ K}$ , $P = 10 - 60 \text{ bar}$ , $\text{WHSV} = 188 \text{ g}_{\text{C}_5\text{g}_{\text{cat}}}^{-1}\text{h}^{-1}$ and $T = 723 \text{ K}$ , $P = 40 \text{ bar}$ , $\text{WHSV} = 94 - 376 \text{ g}_{\text{C}_5\text{g}_{\text{cat}}}^{-1}\text{h}^{-1}$ , respectively.....	69

Figure 4.6: Example product distribution of <i>n</i> -pentane conversion on Mo/H-[B]ZSM-5 ( <i>top</i> ) and Mo/H-[Al]ZSM-5 ( <i>bottom</i> ). Reaction conditions: $T = 723 \text{ K}$ , $P = 40 \text{ bar}$ , and $\text{WHSV} = 188 \text{ g}_{\text{C}_5}\text{g}_{\text{cat}}^{-1}\text{h}^{-1}$ .....	73
Figure 4.7: Consumption of <i>n</i> -pentane, <i>n</i> -hexane, and <i>n</i> -heptane and selectivity to primary dehydrogenation product and olefins lighter than the primary dehydrogenation products on Mo/H-[B]ZSM-5, Mo/ $\gamma$ -Al <sub>2</sub> O <sub>3</sub> , and Mo/[B]Beta. $T = 673 - 798 \text{ K}$ , $P = 40 \text{ bar}$ , $\text{WHSV} = 188 \text{ g}_{\text{C}_5}\text{g}_{\text{cat}}^{-1}\text{hr}$ , $196 \text{ g}_{\text{C}_6}\text{g}_{\text{cat}}^{-1}\text{hr}$ and $205 \text{ g}_{\text{C}_7}\text{g}_{\text{cat}}^{-1}\text{hr}$ .....	74
Figure 4.8: Rates of consumption of <i>n</i> -pentane ( <i>square</i> ), <i>n</i> -hexane ( <i>circle</i> ), and <i>n</i> -heptane ( <i>triangle</i> ) on Mo/H-[B]ZSM-5 and <i>n</i> -pentane on H-[Al]ZSM-5 ( <i>diamond</i> ) at various temperatures. Reaction conditions: $T = 673 - 798 \text{ K}$ , $P = 40 \text{ bar}$ , and $\text{WHSV} = 188 \text{ g}_{\text{C}_5}\text{g}_{\text{cat}}^{-1}\text{hr}$ , $196 \text{ g}_{\text{C}_6}\text{g}_{\text{cat}}^{-1}\text{hr}$ and $205 \text{ g}_{\text{C}_7}\text{g}_{\text{cat}}^{-1}\text{hr}$ for Mo/H-[B]ZSM-5 and $T = 633 - 723 \text{ K}$ , $P = 40 \text{ bar}$ , and $\text{WHSV} = 1120 \text{ g}_{\text{C}_5}\text{g}_{\text{cat}}^{-1}\text{hr}$ for H-[Al]ZSM-5 .....	75
Figure 5.1: Hydrocarbon pool mechanism for methanol conversion to hydrocarbons showing an alkene cycle ( <i>left</i> ) and arene cycle ( <i>right</i> ). Recreated from review by Olsbye et al. [27] .....	80
Figure 5.2: Example catalytic cycle of propylene methylation by dimethyl ether on a zeolite acid site .....	81
Figure 5.3: Reaction network for methanol conversion on H-[Al]Beta. Recreated from publication by Hazari et al. [154] .....	83
Figure 5.4: X-ray diffraction pattern of NH <sub>4</sub> -[Fe]Beta .....	90
Figure 5.5: UV/Vis spectra of [Fe]Beta throughout the synthesis process ( <i>left</i> ) and UV/Vis of as made [Fe]Beta magnified ( <i>right</i> ).....	91
Figure 5.6: SEM of [Fe]Beta ( <i>left</i> ) with silicon EDS ( <i>top right</i> ) and iron EDS ( <i>bottom right</i> ) .....	91
Figure 5.7: Comparison of carbon selectivity of dimethyl ether conversion on H-[Al]ZSM-5 and H-[Fe]Beta. Reaction conditions: $T = 573 \text{ K}$ , $P = 1 \text{ atm}$ , $P_{\text{DME}} = 0.14 \text{ atm}$ , $F_{\text{N}_2} = 60 \text{ mL/min}$ , and $\text{WHSV} = 11.3 \text{ g}_{\text{DME}}\text{g}_{\text{cat}}^{-1}\text{h}^{-1}$ (ZSM-5) and $5.7 \text{ g}_{\text{DME}}\text{g}_{\text{cat}}^{-1}\text{h}^{-1}$ (Beta).....	93

Figure 5.8: Comparison of fresh and regenerated H-[Fe]Beta with regard to dimethyl ether consumption rates (a) and carbon selectivity to methane (b), ethylene (c), propylene (d), C <sub>4</sub> compounds (e), C <sub>5</sub> compounds (f), C <sub>6</sub> compounds (g), and C <sub>7</sub> compounds (h) as a function of time on stream. Reaction conditions: $T = 573$ K, $P = 1$ atm, $P_{\text{DME}} = 0.14$ atm, $F_{\text{N}_2} = 60$ mL/min, and $\text{WHSV} =$ and $5.7 \text{ g}_{\text{DME}}\text{g}_{\text{cat}}^{-1}\text{h}^{-1}$ .....	95
Figure 5.9: Comparison of carbon selectivity of dimethyl ether conversion on H-[Fe]Beta at different reaction temperatures. Reaction conditions: $T = 573 - 603$ K, $P = 1$ atm, $P_{\text{DME}} = 0.14$ atm, $F_{\text{N}_2} = 60$ mL/min, and $\text{WHSV} =$ and $5.7 \text{ g}_{\text{DME}}\text{g}_{\text{cat}}^{-1}\text{h}^{-1}$ .....	96
Figure 5.10: Comparison of carbon selectivity of dimethyl ether conversion on H-[Fe]Beta at different DME partial pressures. Reaction conditions: $T = 573$ K, $P = 1$ atm, $P_{\text{DME}} = 0.14 - 0.40$ atm, $F_{\text{N}_2} = 60$ mL/min, and $\text{WHSV} =$ and $5.7 \text{ g}_{\text{DME}}\text{g}_{\text{cat}}^{-1}\text{h}^{-1}$ .....	97
Figure 5.11: Comparison of carbon selectivity of dimethyl ether conversion on H-[Fe]Beta and Ni/H-[Fe]Beta. Reaction conditions: $T = 573$ K, $P = 1$ atm, $P_{\text{DME}} = 0.14$ atm, $F_{\text{N}_2} = 60$ mL/min, and $\text{WHSV} =$ and $5.7 \text{ g}_{\text{DME}}\text{g}_{\text{cat}}^{-1}\text{h}^{-1}$ .....	98
Figure 5.12: Comparison of carbon selectivity of dimethyl ether conversion on Ni/H-[Fe]Beta at different DME partial pressures. Reaction conditions: $T = 573$ K, $P = 1$ atm, $P_{\text{DME}} = 0.14 - 0.25$ atm, $F_{\text{N}_2} = 60$ mL/min, and $\text{WHSV} =$ and $5.7 \text{ g}_{\text{DME}}\text{g}_{\text{cat}}^{-1}\text{h}^{-1}$ .....	99
Figure 5.13: Most energetically favorable species, based on the stability of the carbocation intermediate and subsequent olefin formed from deprotonation, produced by successive methylation of propylene.....	104
Figure 5.14: Reaction network for methanol conversion on H-[Al]Beta modified to reflect the high selectivity to olefins (particularly isobutene, 2-methyl-2-pentene, and triptene) and low selectivity to paraffins on H-[Fe]Beta. Recreated from publication by Hazari et al. [154] .....	106
Figure 6.1: Process flow diagram of endothermic test rig used to measure endothermicity of a reactant and catalyst. Adapted from Huang et al. [172]. .....	111
Figure 6.2: Comparison of heat absorbed by thermal decomposition of <i>n</i> -dodecane and conversion of <i>n</i> -dodecane with Mo/H-[B]ZSM-5 as a function of temperature .....	113

Figure 6.3: Depiction of mordenite structure with 12 member ring straight channels connected via 8 member ring side pockets.....	114
Figure 6.4: Representation of three possible molybdenum oxide anchored sites: bridged ( <i>left</i> ), single aluminum ( <i>middle</i> ), and silanol ( <i>right</i> ).....	116
Figure 6.5: In situ XANES of 1% Mo/H-[B]ZSM-5 showing the transition from isolated molybdenum oxide to molybdenum carbide species .....	117
Figure 6.6: Example of the crystal structure of a standard zeolite ( <i>top</i> ), a hierarchical zeolite with mesoporous channels ( <i>middle</i> ), and a hierarchical pillared zeolite ( <i>bottom</i> ) .....	119
Figure B.1: X-ray diffraction pattern of [B]ZSM-5 (F-1) with silicon metal added..	137
Figure B.2: X-ray diffraction pattern of [B]ZSM-5 (F-2) .....	138
Figure B.3: X-ray diffraction pattern of [B]ZSM-5 (OH-1).....	138
Figure B.4: X-ray diffraction pattern of [B]ZSM-5 (OH-2).....	139
Figure B.5: X-ray diffraction pattern of Silicalite-1 (MFI Topology) .....	139
Figure B.6: X-ray diffraction pattern of [B]Beta.....	140
Figure B.7: SEM image of [B]ZSM-5 (F-1) .....	140
Figure B.8: SEM image of [B]ZSM-5 (F-2) .....	141
Figure B.9: SEM image of [B]ZSM-5 (OH-1).....	141
Figure B.10: SEM image of [B]ZSM-5 (OH-2).....	142
Figure B.11: SEM image of Silicalite-1 .....	142
Figure B.12: SEM image of deboronated [B]ZSM-5 (OH-1) .....	143
Figure B.13: SEM image of [B]Beta.....	143
Figure C.1: GC/MS data with peak labeled matching Table C.1 .....	146
Figure C.2: Mass spectrometer fragmentation pattern for isobutane peak.....	147
Figure C.3: Mass spectrometer fragmentation pattern for isobutene peak.....	148

Figure C.4: Mass spectrometer fragmentation pattern for <i>n</i> -butane peak .....	149
Figure C.5: Mass spectrometer fragmentation pattern for 2-butene peak .....	150
Figure C.6: Mass spectrometer fragmentation pattern for 2-methyl-1-butene peak ..	151
Figure C.7: Mass spectrometer fragmentation pattern for 2-methylbutane peak .....	152
Figure C.8: Mass spectrometer fragmentation pattern for 2-pentene peak .....	153
Figure C.9: Mass spectrometer fragmentation pattern for 2-pentene peak .....	154
Figure C.10: Mass spectrometer fragmentation pattern for 2-methyl-2-butene peak	155
Figure C.11: Mass spectrometer fragmentation pattern for 2,3-dimethyl-1-butene peak .....	156
Figure C.12: Mass spectrometer fragmentation pattern for 2-methylpentane peak ...	157
Figure C.13: Mass spectrometer fragmentation pattern for 2-methyl-1-pentene peak	158
Figure C.14: Mass spectrometer fragmentation pattern for 2-methyl-2-pentene peak	159
Figure C.15: Mass spectrometer fragmentation pattern for 3-hexene peak .....	160
Figure C.16: Mass spectrometer fragmentation pattern for 3-methyl-2-pentene peak	161
Figure C.17: Mass spectrometer fragmentation pattern for 2,3-dimethyl-2-butene peak .....	162
Figure C.18: Mass spectrometer fragmentation pattern for 2,3,3-trimethyl-1-butene peak .....	163

## ABSTRACT

Hydrocarbon conversion processes change the molecular weight, structure, and H/C ratio of the feed stream and are vital for supplying fuels, petrochemicals, and many other valuable molecules to the world. These processes include cracking, isomerization, dehydrogenation, hydrotreating, polymerization, and many more. Zeolites – nanoporous crystalline aluminosilicates that have molecular-sized pores and channels – are among the most frequently used catalysts. They can be prepared from just silicon and oxygen – a purely siliceous sample – or with heteroatom substitution into the framework. If the heteroatom is trivalent, such as aluminum, the framework becomes negatively charged and a cation must be added for charge balance. When a proton is used for charge balance, a Brønsted acid site is generated, and the acid strength of the proton can be modulated by the trivalent heteroatom substituted into the framework, affecting the relative rates of the hydrocarbon conversion processes. In this thesis, we investigated the influence of acid strength on high-pressure catalytic cracking and dehydrogenation for aircraft endothermic cooling, as well as methanol conversion to hydrocarbons (MTH), by changing the heteroatom substituted into the zeolite framework.

The first process investigated was high-pressure catalytic cracking of *n*-pentane on acidic H-[Al]ZSM-5 to produce light olefins. Although ethylene and propylene were the targeted products, these were rapidly consumed via secondary bimolecular reactions, such as hydride transfer and oligomerization, leading to a reduction in reaction endothermicity. The second process investigated was high-

pressure dehydrogenation of C<sub>5</sub>-C<sub>7</sub> normal paraffins using supported molybdenum carbide nanoparticles. To reduce the secondary bimolecular reactions described above, weakly acidic H-[B]ZSM-5 was used as a support for molybdenum. By using H-[B]ZSM-5 as a support instead of  $\gamma$ -Al<sub>2</sub>O<sub>3</sub>, we were able to maintain high selectivity to the primary dehydrogenation product (>90%), while observing over a 100 percent increase in reactant consumption rates.

The final process investigated was methanol conversion to produce olefins, with the intent of producing olefins larger than ones formed by zeolites such as H-SAPO-34 and H-[Al]ZSM-5. H-[Fe]Beta was selected for this reaction as iron zeolites have an acid strength sufficiently strong to catalyze methanol conversion, but slowly catalyzes hydride transfer reactions, a necessary condition to minimize aromatics formation. By using H-[Fe]Beta for the conversion of dimethyl ether, olefins were produced with greater than 90 percent selectivity with isobutene being the major product.

Our research has shown that by changing the heteroatom substituted into the zeolite framework, we can adjust the acidity of the catalyst and alter the chemistry of hydrocarbon conversion processes to enhance selectivity and yield.

## **Chapter 1**

### **INTRODUCTION**

This thesis addresses controlling the product selectivity of hydrocarbon conversions by altering the acidity of zeolite catalysts. Solid acid catalyzed hydrocarbon conversion processes are found in a variety of industries and are especially critical in petrochemical production. A main challenge of acid catalyzed hydrocarbon conversion is having fast reaction rates that consume the reactant molecule(s) and produce the desired products while suppressing side reactions that produce undesirable products or consume desired ones. Through adjustments in operating conditions and catalyst design, these undesirable side reactions can be mitigated and product selectivity controlled.

#### **1.1 Hydrocarbon Conversion Processes**

Hydrocarbon conversion processes change the molecular weight, structure, and H/C ratio of a specific molecular species or more frequently, a mixture of hydrocarbons of similar molecular weight. These conversions involve hydrocarbons containing just hydrogen and carbon, or can also involve species containing heteroatoms, such as oxygen, nitrogen, and sulfur as these are present in fossil fuels in different amounts. Many types of reactions are utilized to produce fuels and petrochemicals in refineries and other chemical processes. Figure 1.1 illustrates just a few.

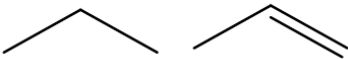
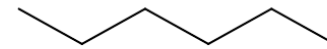
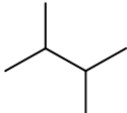
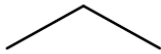
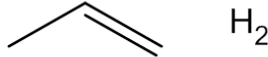
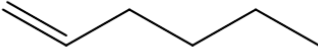
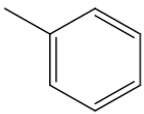
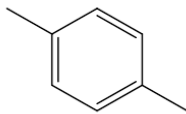
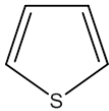
Reaction	Reactants	Products
Cracking		
Isomerization		
Dehydrogenation		
Oligomerization	3 	
Alkylation	 CH <sub>3</sub> OH	 H <sub>2</sub> O
Hydrotreating	 H <sub>2</sub>	 H <sub>2</sub> S

Figure 1.1: Example of reactions used in hydrocarbon conversion processes

Conversion processes are used to upgrade low value hydrocarbon sources into higher value commodity products, fuels, and chemicals. Many hydrocarbon feeds originate from fossil fuels, such as oil, natural gas, and coal, but these streams can also be derived from bio-based materials, such as lignocellulosic biomass and fats, or synthesis gas products. There are numerous end products generated through hydrocarbon conversion processes, including fuels, polymers/plastics, surfactants, drugs, food additives, and many more [1–9].

### **1.1.1 Upgrading Petroleum Oil**

Following distillation to separate petroleum oil into different fractions based on boiling point temperatures, the individual fractions can be upgraded to increase production of valuable products. Referred to as the “heart of a refinery,” fluidized catalytic cracking units (FCC) take heavy gas oil from distillation and crack high molecular weight species into lower molecular weight compounds in the gasoline fraction, as well as light olefins, ethylene, propylene, and butenes [10]. These light olefins are then used as feedstocks for polyolefin production [11].

Increasing the octane number of a hydrocarbon feed is required to produce higher value gasoline and is accomplished in two ways: isomerization and alkylation. First, straight chain *n*-paraffins are isomerized, producing branched chain alkanes which have higher octane number than their parent *n*-paraffins [12]. Second, light olefins, such as butenes and pentenes, are alkylated, increasing molecular weight and branching [13].

Hydrotreating units are used primarily to remove O, N and S from a hydrocarbon stream and to meet emission standards for fuels set by government agencies. In particular, there are limits to the amount of benzene and sulfur allowed in fuels, such as gasoline and diesel. Hydrogen is used to saturate aromatics to form cyclic paraffins and to remove the heteroatoms sulfur, nitrogen, and oxygen.

### **1.1.2 Upgrading Natural Gas**

Natural gas consists primarily of methane, but also contains ethane, propane, and to a lesser extent, heavier hydrocarbons [14]. Because ethylene and propylene are

by-products of fluidized catalytic cracking, there is an economic balance between altering selectivity to produce more light olefins over gasoline [15]. Alternatively, ethane and propane from natural gas can be dehydrogenated to produce the corresponding olefins and meet demand for these polymer precursors. Of recent interest has been the direct conversion of methane to value added chemicals. Direct methane conversion to aromatics is being investigated to provide precursors for polymers production [16–19]. Another direct conversion of methane is partial oxidation to methanol, although this process is not practiced at high methane consumption rates [20–24]. Methanol can then be converted via methanol-to-hydrocarbon (MTH) processes producing olefins, aromatics, or gasoline [25–27].

### **1.1.3 Upgrading Bio-based Sources**

A renewable form of carbon-based feedstocks is biomass (mostly from plant origin), a material that encompasses a broad group of compounds. For the purpose of this thesis, the most relevant source of biomass-derived carbon is lignocellulosic biomass, a material that is formed primarily of cellulose (a polysaccharide) and lignin (a phenolic-based polymer) [28]. Once polysaccharides are broken down into their basic building units (sugars), these sugars can be transformed into valuable chemicals. For example, ethanol is produced from glucose via fermentation with yeast and can be blended with gasoline. Another example is production of furans from fructose [29–32]. These furans can then be converted into a variety of other useful chemicals (Fig 1.2).

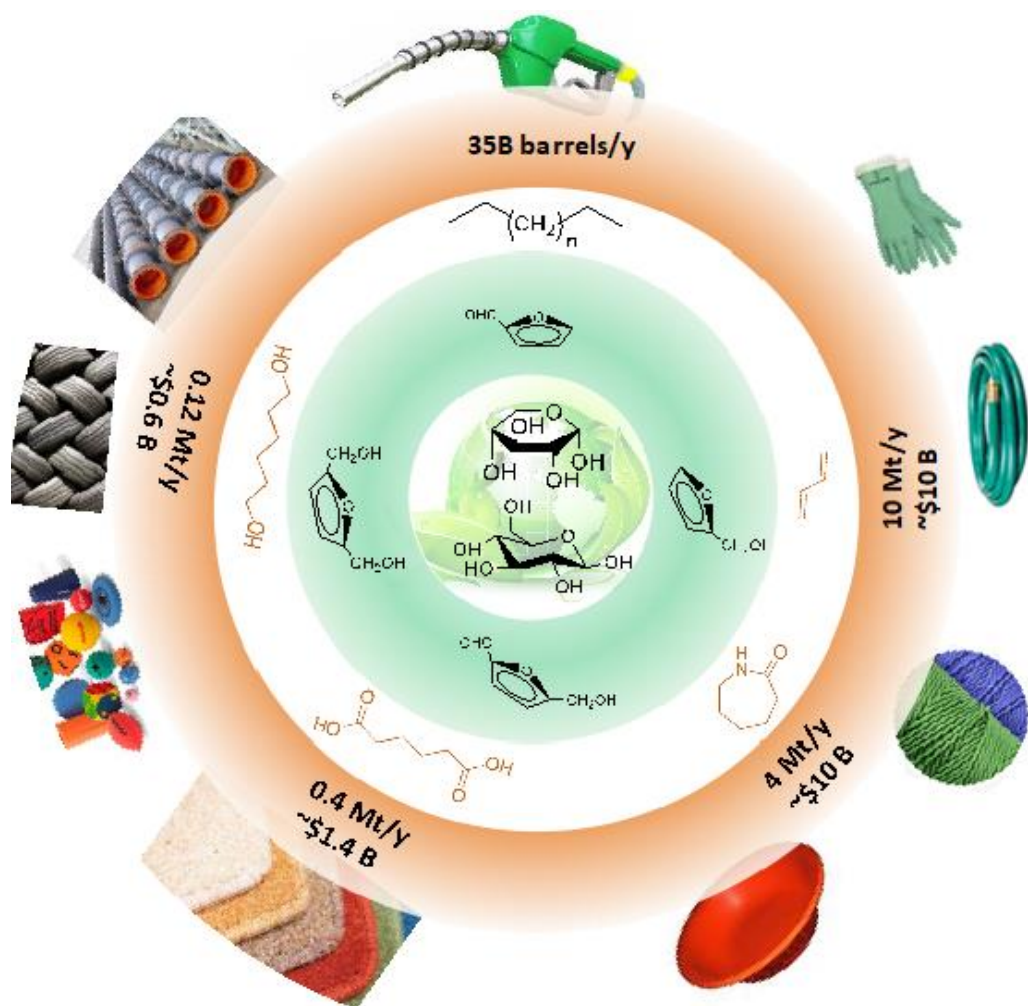


Figure 1.2: Example of fuels, chemicals, and materials produced from biomass through furanic intermediates

Biomass-derived triglycerides can be broken down via hydrolysis, producing glycerol and fatty acid salts [33]. Fatty acid salts are surfactants, containing a hydrophilic carboxylic group and hydrophobic hydrocarbon chains, and are typical component soaps. Triglycerides can also be upgraded through transesterification with an alcohol, such as methanol or ethanol, to produce biodiesel [34].

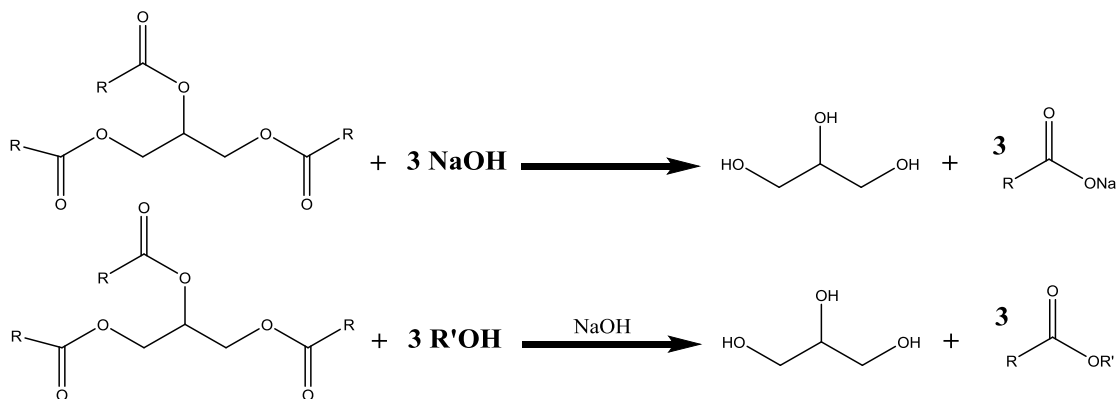


Figure 1.3: Hydrolysis of triglyceride to produce soaps (top) and transesterification of triglyceride to produce biodiesel (bottom)

#### 1.1.4 Synthesis Gas

Through steam reforming, hydrocarbons can be transformed into synthesis gas (syngas) consisting of mostly carbon monoxide and hydrogen [35,36]. Syngas can then be converted into hydrocarbons in the Fischer-Tropsch process [37,38]. Alternatively, the syngas can be converted to methanol, which can then be transformed in MTH processes [39]. Through these two methods, syngas represents a pathway to produce valuable hydrocarbons from low cost coal, natural gas, and biomass in areas that do not have readily available petroleum sources.

#### 1.2 Hydrocarbon Conversion Catalysis

Nearly all hydrocarbon conversion processes are enhanced using catalysts. Catalysts are divided into two main groups: homogeneous and heterogeneous. Homogeneous catalysts are, by definition, in the same phase that the liquid or gas phase reactions are investigated. Homogeneous catalysts can be as simple as sulfuric acid or sodium hydroxide, which are used in acid/base chemistry, or more complex as

in organometallic complexes important in pharmaceuticals production (Figure 1.4) [40].

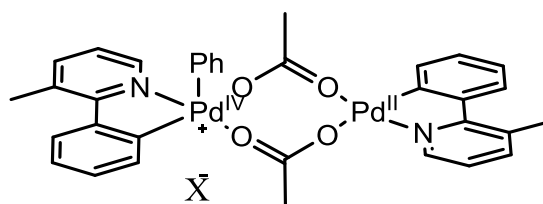


Figure 1.4: Palladium organometallic complex formed during aryl-aryl bond formation

Heterogeneous catalysts are present as a different phase than the reactants and products. Heterogeneous catalysis has been used in this thesis to convert gases and liquids to produce more valuable species. Simple heterogeneous catalysts are bulk metals, such as iron in the reverse water gas shift reaction [41], or metal oxides, such as alumina or silica used in the first catalytic cracking units [10]. Increasing surface area of a metal catalyst is accomplished by supporting the metal on a porous medium. The formation of metal nanoparticles allows more active sites to be present per mass of metal, increasing reaction rates. Another class of catalysts is zeolites, which play an important role in hydrocarbon conversion processes used industrially and under investigation for future applications.

### 1.2.1 Zeolites and Other Crystalline Molecular Sieves

Zeolites are crystalline aluminosilicates that have molecular-sized pores and channels (Figure 1.5). Zeolites are both naturally occurring and synthetic, with over 200 known structures [42]. Zeolites are also known as molecular sieves, as they can separate molecules based on molecular size or shape. Zeolites are used in a variety of applications, including as adsorbents and they are, as a class, the most widely used solid acid catalyst in the petrochemical industry.

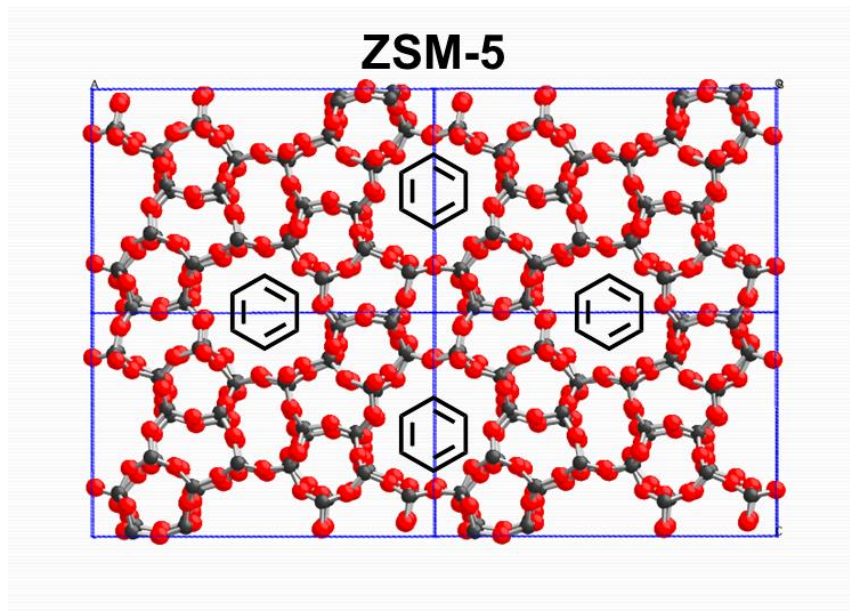


Figure 1.5: Depiction of zeolite ZSM-5 channels with an approximate relationship to the size of benzene molecules

The multitude of applications of zeolites as catalysts arises from their unique structure, variable composition, and thermal stability. Zeolites can be prepared in a siliceous form – containing only silicon and oxygen – or a heteroatom can be

substituted in place of silicon. If that heteroatom is trivalent, the framework becomes negatively charged, and a cation must be added to balance the charge. If the cation is a proton, a Brønsted acid site is formed. On the other hand, if a tetravalent transition metal is substituted into the framework, that metal site can act as a Lewis acid.

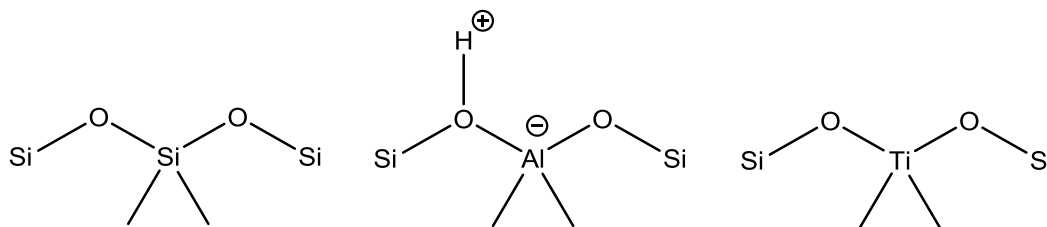


Figure 1.6: Example of siliceous framework (left), trivalent aluminum substitution into the zeolite framework creating a negatively charge framework accompanied by a proton for charge balance (middle), and tetravalent titanium substitution (right)

### 1.2.2 Zeolite Synthesis

Zeolites are normally produced via autogenous hydrothermal synthesis processes. In this method, a synthesis gel is prepared by mixing a silica source, a metal source (if necessary), an organic structural directing agent (SDA), and a mineralizing agent [43]. Typical silica sources include fumed silica, such as Cab-o-sil, or sodium silicate. Heteroatom sources include metal hydroxides, chlorides, or nitrates. Structural directing agents, also known as templates, are quaternary ammonium compounds, such as tetramethylammonium. Hydroxide or fluoride anions are used as mineralizing agents. All ingredients are mixed together and loaded into a Teflon-lined autoclave. The autoclave is then heated at a pre-specified temperature and duration of time, known as crystallization.

During the heating process, the mineralizer breaks down the silica. The silica then begins to coalesce around the organic template, directing the formation of the zeolite structure.

When a trivalent heteroatom is incorporated, the framework becomes negatively charged and the SDA, as well as cation accompanying the mineralizer, aids in stabilizing the negative charge. Upon completion of crystallization, the resulting zeolite is filtered, dried, and calcined in air to decompose and remove the SDA.

Following calcination, an ion exchange must be performed to change the cation balancing the negative charge of the framework. If a proton is desired, the zeolite is ion exchanged with an ammonium solution. The resulting ammonium form is heated to decompose and release ammonia, leaving behind a proton. If a metal cation is desired, a second ion exchange is performed with the ammonium for zeolite in a metal salt solution.

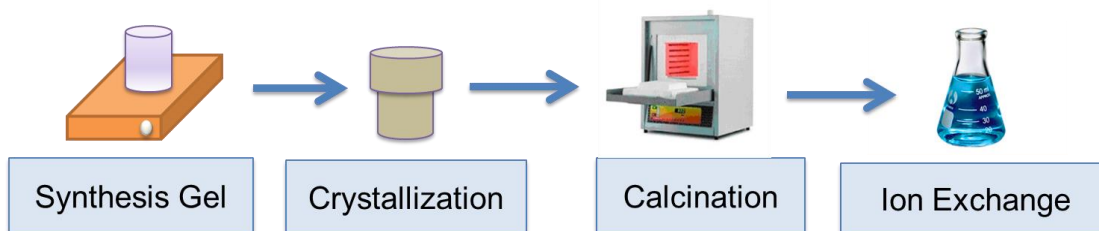


Figure 1.7: Illustration of zeolite synthesis procedure

There are many factors that affect which zeolite structure is formed. The SDA plays a major role as it is the “porogen”, that is, the species that the dissolved silica polymerizes around. Other factors include temperature, time, molar ratios of materials

in the synthesis gel, pH, and cations that accompany the mineralizing agent (Na, K, or H if fluoride is used) [44–47].

### 1.2.3 Zeolite Catalysis

Zeolites are thermally stable materials (up to temperatures of 1000 °C or more), able to withstand the harsh conditions of industrial processes, and tunable, giving rise to their versatility. Three main attributes of zeolites can be altered to influence their catalytic activity: zeolite structure (size and shape of pores and channels), framework heteroatom substitution, and the identity of the cation for charge balance.

Size and shape of pores and channels influence selectivity of reactions based on transition state. If the transition state is too large, then these reactions are suppressed. An example of shape selectivity is the transalkylation of toluene to form benzene and xylene (Figure 1.8). In this case, H-[Al]ZSM-5 is used to catalyze the reaction. Because of the size of the channels in ZSM-5, *p*-xylene is the favored product, as the transition states required to form *o*-xylene or *m*-xylene are larger than *p*-xylene [48].

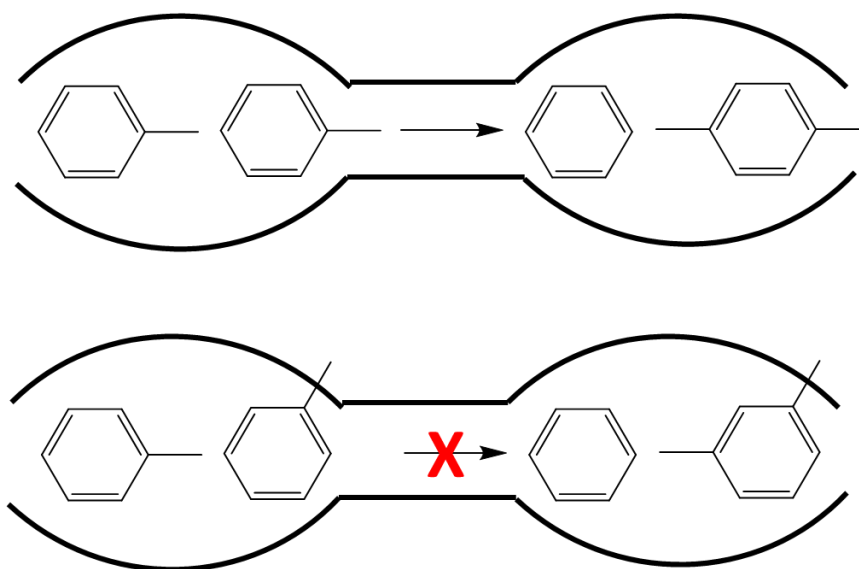


Figure 1.8: Transalkylation of toluene on H-[Al]ZSM-5 selectively producing *p*-xylene over *m*-xylene

Heteroatom substitution into the framework influences the acidity of the site. For the number of possible trivalent heteroatom substitutions, this leads to varying the Brønsted acid strength of the proton added for charge balance. Four trivalent heteroatoms commonly substituted into the framework are aluminum, gallium, iron, and boron. Figure 1.9 shows the rate of methanol dehydration to dimethyl ether on various ZSM-5 catalysts [49]. This probe reaction illustrates the acidity of the zeolite and how different heteroatom substitution affects acidity.

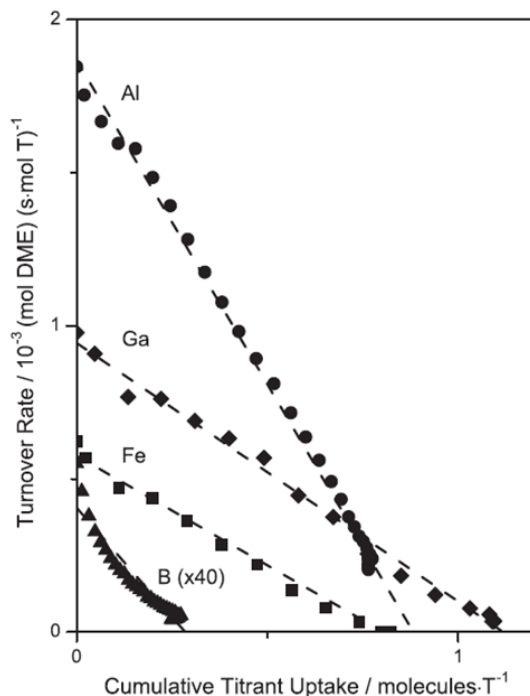


Figure 1.9: Rate of methanol dehydration to dimethyl ether with varying heteroatom substitution in the zeolite framework. Reprinted from Journal of Catalysis, Vol. 312, A.J. Jones, R.T. Carr, S.I. Zones, and E. Iglesia, *Acid strength and solvation in catalysis by MFI zeolites and effects of the identity, concentration and location of framework heteroatoms*, 56-68, 2014, with permission from Elsevier [49].

Aluminum is close in size to silicon allowing for a stable substitution. In addition, aluminum-substituted zeolites to have the strongest acidity. On the other hand, boron is much smaller than silicon and does not incorporate well into the framework. Boron remains trigonally bound in the framework instead of tetrahedrally required to produce the strong Brønsted acid site (Figure 1.10).

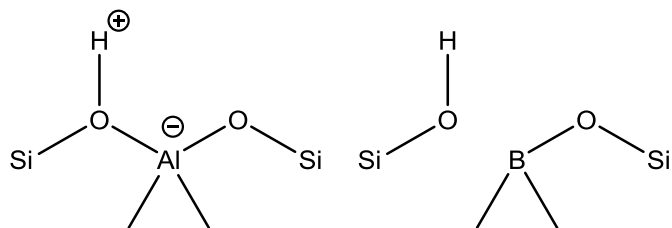


Figure 1.10: Comparison of aluminum and boron substituted into a zeolite framework

Finally, the cation added for charge balance can affect reactions. Cations can be monovalent, like sodium, or divalent, like zinc. Copper exchanged zeolites are used for selective catalytic reduction of NO<sub>x</sub> for exhaust gas cleanup [50]. Nickel exchanged zeolites can be used to promote oligomerization [51]. Sodium exchanged zeolites can be used as Lewis acids, such as catalyzing dehydration of methyl lactate [52].

### 1.3 Challenges in Modern Catalysis

While major hydrocarbon conversion processes today exist primarily in petroleum refining and polymer production, there remain numerous opportunities to introduce innovations in catalysis and chemicals productions. Many of these opportunities exist in producing fuels and chemicals from sources other than petroleum, such as biomass or methane, and environmental applications, such as carbon dioxide capture/conversion or NO<sub>x</sub> reduction in exhaust. Other opportunities exist in niche applications or process energy reduction as exemplified below.

With the large amount of methane reserves held within shale in the United States, continued investigation on direct methane conversion, whether through methanol conversion, Fischer-Tropsch, or MDA, provides a route to utilize natural gas reserves other than heat production. Conversion of carbon dioxide into chemicals or

fuels represents a means to reduce atmospheric amounts of the greenhouse gas. Two main routes have been proposed: heterogeneous catalytic and electrocatalytic processes. Using current technologies, carbon dioxide can be converted to fuels through the reverse water gas shift reaction followed by Fischer-Tropsch, but a single process has been demonstrated using Fe<sub>3</sub>O<sub>4</sub>/H-[Al]ZSM-5, converting carbon dioxide and hydrogen directly into gasoline fuel [53]. For electrocatalytic processes, acidic solutions act as a hydrogen source for converting carbon dioxide to carbon monoxide or hydrocarbons [54–56].

Besides hydrocarbon conversion processes, catalysts can be employed to enhance other energy intensive processes. The Haber-Bosch process supplies ammonia for fertilizer production, but consumes 1-2% of global energy demand and 3-5% of methane as a hydrogen source [57]. Reductions in energy consumption through improved catalysts or switching to electrochemical routes would have a large global impact [58]. Separation processes also consume a large amount of energy in fuels and chemicals production. Improvements in absorbents or molecular filters, which are similar, if not the same as catalysts, would represent another reduction in energy consumption.

#### **1.4 Scope of this Thesis**

The focus of this thesis is to investigate the control of selectivity of hydrocarbon conversions by using zeolite catalysts. The acidity of the zeolite catalysts was altered by varying the trivalent heteroatom substituted into the framework. Catalytic activity was further altered by changing the cation added to balance the framework charge. In this thesis, three hydrocarbon conversions were investigated:

catalytic cracking of *n*-pentane with H-[Al]ZSM-5, catalytic dehydrogenation of C<sub>5</sub>-C<sub>7</sub> alkanes on Mo/H-[B]ZSM-5, and methanol to hydrocarbons with H-[Fe]Beta.

The first process investigated was high-pressure catalytic cracking of *n*-pentane on acidic H-[Al]ZSM-5 for aircraft endothermic cooling (Chapter 3). The goal is to use endothermic reactions to act as a heat sink for excess thermal energy produced during combustion. Although ethylene and propylene were the targeted products, these were rapidly consumed via secondary bimolecular reactions, such as hydride transfer and oligomerization, leading to a reduction in reaction endothermicity.

The second process investigated was high-pressure dehydrogenation of C<sub>5</sub>-C<sub>7</sub> normal paraffins using supported molybdenum carbides (Chapter 4). To reduce the secondary bimolecular reactions described above, weakly acidic H-[B]ZSM-5 was used as a support for molybdenum. By using H-[B]ZSM-5 as a support instead of  $\gamma$ -Al<sub>2</sub>O<sub>3</sub>, we were able to maintain high selectivity to the primary dehydrogenation product (>90%), while observing upwards of a two-fold increase in reactant consumption rates.

The final process investigated was methanol conversion to produce olefins, with the intent of producing olefins larger than ones formed by zeolites such as H-SAPO-34 and H-[Al]ZSM-5 (Chapter 5). H-[Fe]Beta was selected for this process as iron zeolites have an acid strength sufficiently strong to catalyze methanol conversion, but slowly catalyzes hydride transfer reactions, a necessary condition to minimize aromatics formation. By using H-[Fe]Beta, conversion of dimethyl ether produced olefins with greater than 90 percent selectivity. Our research has shown that by changing the heteroatom substituted into the zeolite framework, we can adjust the

acidity of the catalyst and alter the chemistry of hydrocarbon conversion processes to enhance selectivity and yield.

## Chapter 2

### EXPERIMENTAL TECHNIQUES

Many experimental and analytical techniques can be used to characterize zeolites and the reactions they catalyze. Most catalyst characterization techniques involve spectroscopy, using infrared, visible, ultraviolet, or x-ray radiation. Other techniques involve adsorption and desorption of molecules to test porosity or acidity. Catalyst activity is tested by using a reactor to probe a given reaction and analyzing products through chromatography, mass spectrometry, and spectroscopic techniques, many which overlap with catalyst characterization. Techniques used to characterize catalysts and analyze products of hydrocarbon conversions in this thesis are described below.

#### 2.1 Catalyst Characterization

##### 2.1.1 Powder X-ray Diffraction

X-ray diffraction (XRD) is a spectroscopic technique used to determine a zeolite's structure. Incident x-ray beams are scattered by the crystal structure according to Bragg's Law (Eq 2.1), where  $\lambda$  is the wavelength of light,  $d$  is the atomic spacing, and  $\theta$  is the angle of diffraction [59].

$$n\lambda = 2d\sin(\theta) \quad (\text{Eq. 2.1})$$

When the angle of the incident beam satisfies Bragg's Law, constructive inference occurs and a peak is recorded. The peaks are based on the unique d-spacing

of a given crystal structure and therefore able to determine which zeolite structure is present based on the diffraction pattern. X-ray diffraction can also be used to determine unit cell dimensions and atomic position with the crystal structure.

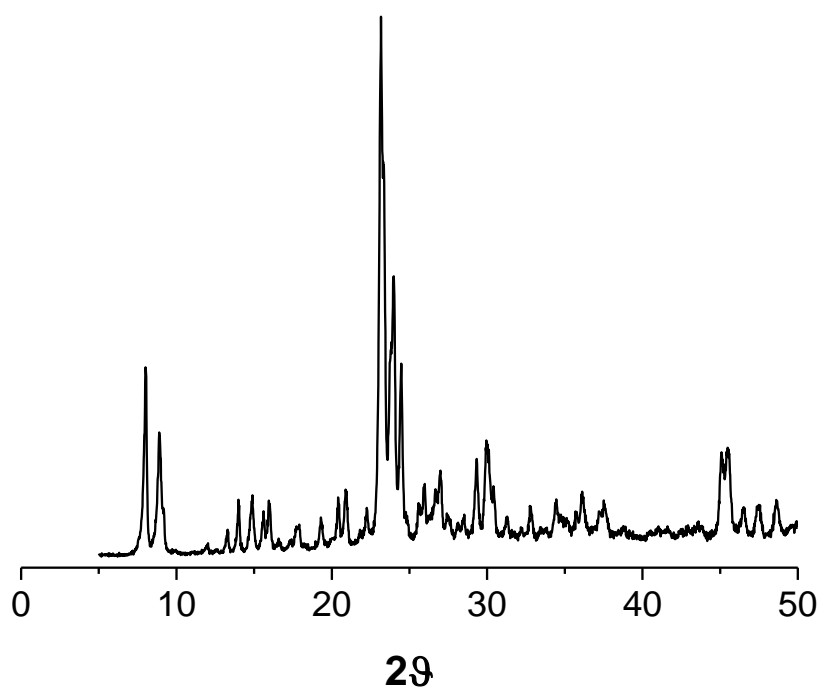


Figure 2.1: X-ray diffraction pattern of [Al]ZSM-5

Each peak recorded during X-ray diffraction corresponds to a specific lattice plane. If the crystal symmetry is known (i.e., cubic or orthorhombic) then the angles of diffraction at which the peaks occur can be used to determine the unit cell parameters

and volume. In Rietveld refinement, a simulated X-ray diffraction pattern is fitted with a recorded pattern, usually from synchrotron radiation, to determine atomic positions within the unit cell of a zeolite.

### **2.1.2 Solid State Nuclear Magnetic Resonance Spectroscopy (SSNMR)**

Solid state  $^{29}\text{Si}$  NMR spectroscopy is used to determine the degree of heteroatom incorporation into the framework. If only silicon is present, one peak will be detected in the Q(4) position, represented as Si(0Al) in Figure 2.2. If a heteroatom is substituted into the framework, an upfield shift in the NMR signal will be detected and the area of the peak, through peak deconvolution, is proportional to the amount of the heteroatom substituted into the framework. One neighboring Al would be Q(3) or Si(1Al) and so on. Solid state NMR can also be used to detect whether the heteroatoms are bound in the framework or in extra-framework positions, as in the case of  $^{27}\text{Al}$  NMR (Fig 2.3).

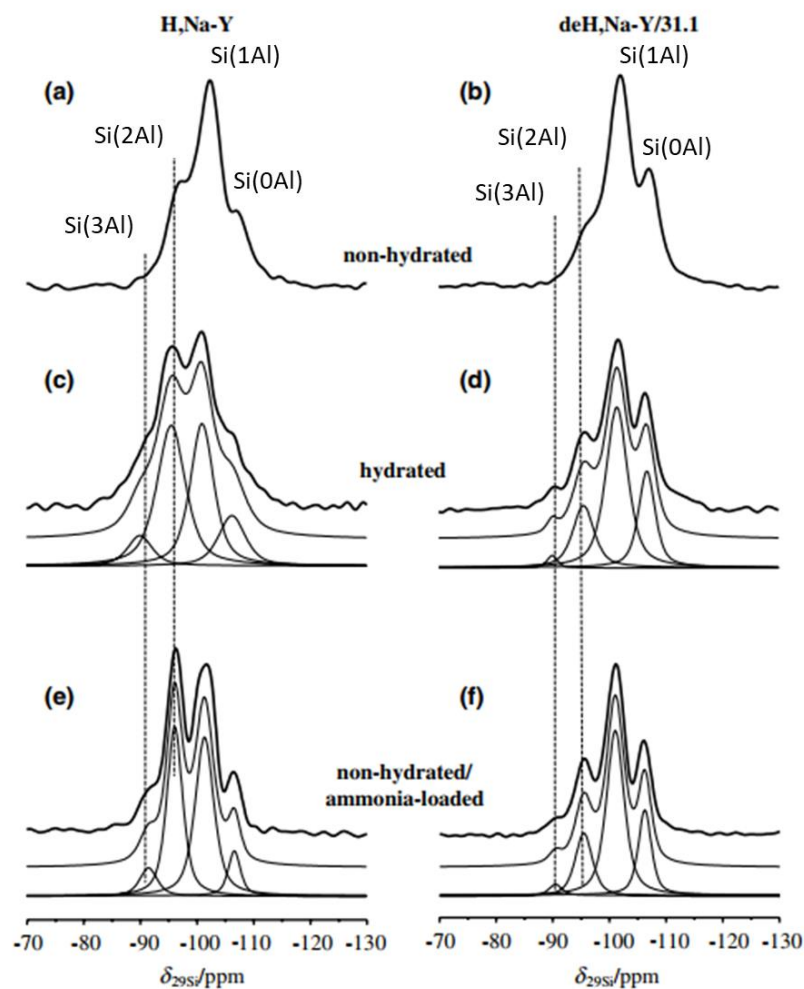


Figure 2.2  $^{29}\text{Si}$  NMR of zeolite NaY that has been dehydrated, hydrated, or ion exchanged with ammonium nitrate (a, c, and e) and steam treated NaY under the same conditions (b, d, f). Reprinted from *Microporous and Mesoporous Materials*, Vol. 90, J. Jiao, W. Wang, B. Sulikowski, J. Weitkamp, and M. Hunger,  *$^{29}\text{Si}$  and  $^{27}\text{Al}$  MAS NMR characterization of non-hydrated zeolites Y upon adsorption of ammonia*, 246-250, 2006, with permission from Elsevier. [60]

Hydration and cation exchange affects the Si and Al NMR spectra. When a sample is exposed to water, some of the Si-Al bonds can be hydrated leading to formation of octahedral aluminum (Al VI) and shifts from Q(2) to Q(3) for example.

Cation exchange aids in stabilizing heteroatom substitution in the framework and also causes shifts in NMR spectra.

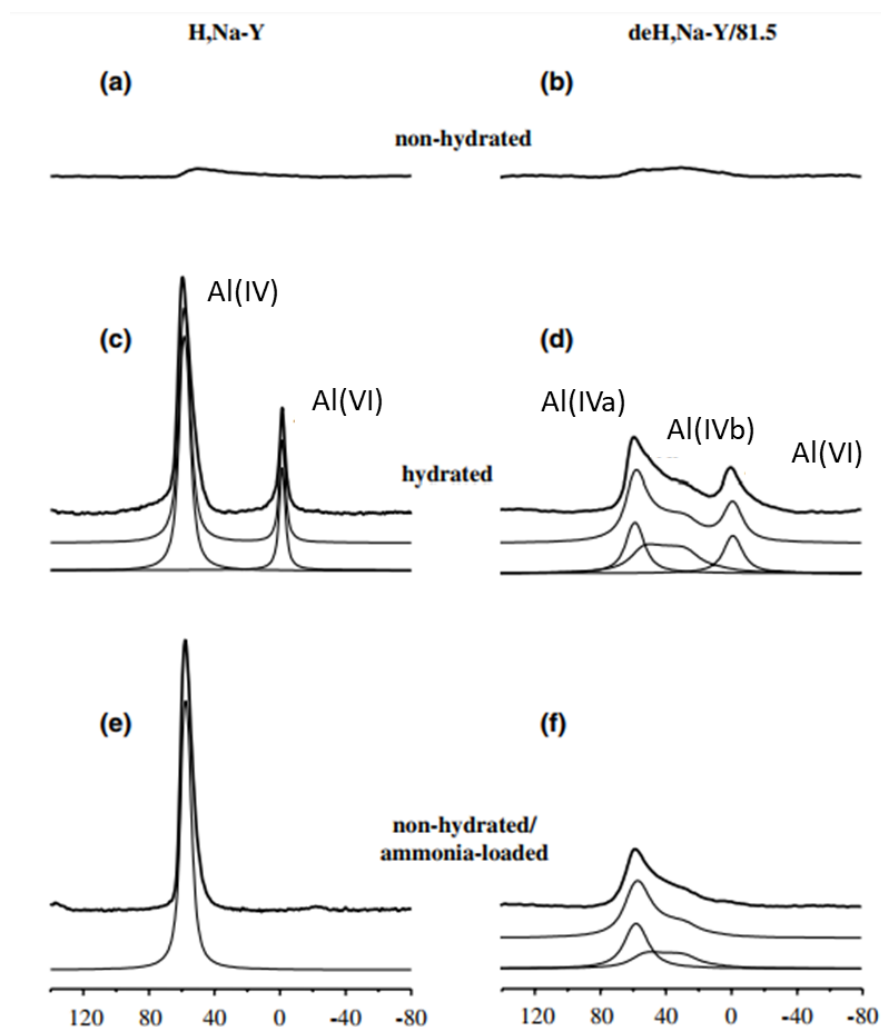


Figure 2.3:  $^{27}\text{Al}$  NMR of zeolite NaY that has been dehydrated, hydrated, or ion exchanged with ammonium nitrate (a, c, and e) and steam treated NaY under the same conditions (b, d, f). Reprinted from *Microporous and Mesoporous Materials*, Vol. 90, J. Jiao, W. Wang, B. Sulikowski, J. Weitkamp, and M. Hunger,  *$^{29}\text{Si}$  and  $^{27}\text{Al}$  MAS NMR characterization of non-hydrated zeolites Y upon adsorption of ammonia*, 246-250, 2006, with permission from Elsevier. [60]

### **2.1.3 Ultraviolet-Visible Spectroscopy (UV/Vis)**

UV/Vis spectroscopy is used to detect transition metal incorporation into the framework. When transition metals are bound tetrahedrally in the framework, ligand-to-metal charge transfer occurs between oxygen and the metal.

### **2.1.4 Infrared Spectroscopy**

Infrared (IR) spectroscopy is valuable in determining species adsorbed to the catalyst surface. An IR beam interacts with the bonds of molecules at given wavelengths based on the resonant frequency of the bond between two atoms and the vibrational mode that is activated (i.e. stretching or bending). By measuring what fraction of the IR beam is absorbed at each wavelength, a spectrum is obtained. This spectrum can aid in elucidating the structure of adsorbed surface species by comparing the wavenumbers at which the beam is absorbed to those of known bond vibrational modes.

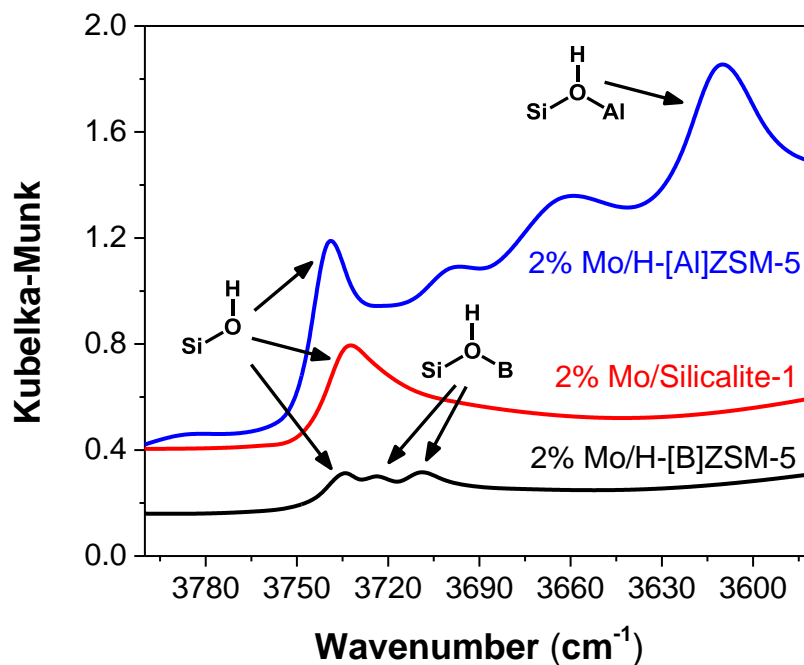


Figure 2.4: IR spectra showing the O-H stretching bands of molybdenum impregnated ZSM-5 samples with different framework compositions

### 2.1.5 X-ray Fluorescence Spectroscopy

X-ray fluorescence spectroscopy (XRF) is used to determine elemental composition of materials. X-rays of varying energy are shined onto a sample. The x-rays excite an inner electron to a higher orbital and when the electron falls back down (relaxes), a photon is released related to the energy difference between the two orbitals. Each element has specific energy levels based on their electronic structure, allowing for elemental identification from energy levels released from the excited sample.

### **2.1.6 X-ray Absorption Spectroscopy**

X-ray absorption spectroscopy (XAS) operates in a similar method of x-ray fluorescence, but instead of measuring the energy of the photon released from the fluorescence, the number of photons absorbed by the material is measured. X-rays are passed through a sample and the energy of the beam is slowly increased. When the incident beam energy reaches the binding energy of an electron, there is a drastic increase in the amount of photons absorbed. The binding energy is determined by the element and oxidation state of the atom.

The analysis of the region surrounding the binding energy is known as x-ray absorption near edge spectroscopy (XANES), where the edge region is the area of drastic increase in photon absorption. Following the edge region, is a region analyzed as extended x-ray absorption fine structure (EXAFS). In this region, the secondary photon emitted from the excited atom is absorbed by a neighboring atom. The successive emission and reabsorption gives a pattern known as “wiggles” and is determined by the first neighbor shell surrounding the atom initially excited. X-ray absorption is commonly used to determine the oxidation state of metals in catalysts through XANES and the coordination sphere of metals through EXAFS under reaction conditions.

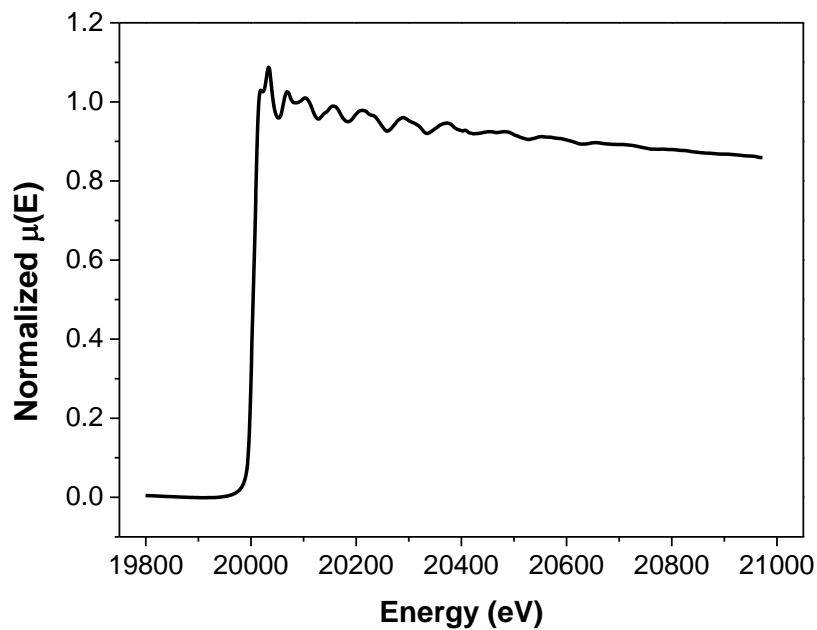
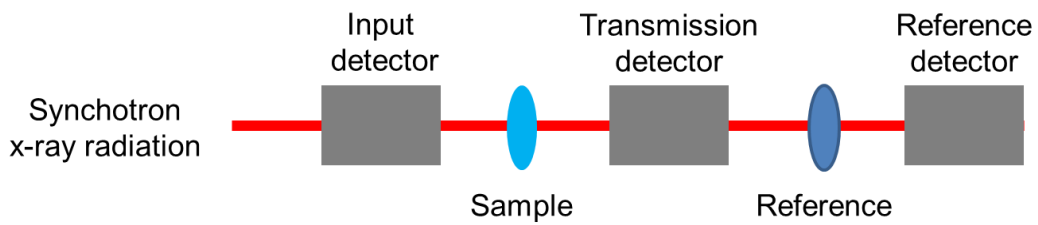


Figure 2.5: Example of XAS setup at a synchrotron light source (*top*) and XAS spectra of molybdenum carbide (*bottom*)

### 2.1.7 Scanning Electron Microscopy

Scanning electron microscopy (SEM) is useful to visualize crystal morphology and size with a resolution on the order of nanometers. A concentrated electron beam is accelerated at a sample under vacuum. Electrons in the beam excite electrons of atoms on or near the surface of the sample and as these electrons relax, photons are released

and detected to form an image. Also, electrons can be scattered and collected to form an image.

Coupled with SEM is energy dispersive X-ray spectroscopy (EDS). EDS operates on the same principle as x-ray absorption techniques with electrons of the SEM beam exciting electrons of atoms in the sample and the relaxation energy is characteristic to each element. The difference between the two techniques is x-ray absorption or fluorescence yields a bulk composition, whereas EDS yields a map of elemental distribution on the surface of the sample.

### **2.1.8 Sample Texture Analysis**

Nitrogen adsorption is a technique used to determine surface area, pore volume, and pore type of materials. As defined by IUPAC, there are three pore types: micropores, which are less than 2 nm in width, mesopores, which are 2 nm to 50 nm in width, and macropores, which are larger than 50 nm in width [61]. Depending on the shape of the isotherm, the type of pore and fraction of porosity contributed can be determined.

Zeolites are microporous materials and therefore exhibit a Type I adsorption isotherm, where the internal surface area of the pores is much greater than the external surface area of the crystals. A large uptake of nitrogen occurs at low partial pressures as the micropores are filled, followed by a slow increase in nitrogen uptake at higher partial pressures as the external surface is covered. Zeolites can be modified to contain mesopores, which results in a Type IV isotherm, where a monolayer forms in the mesopores before the micropores become saturated as in a Type I isotherm [62].

### **2.1.9 Inductively Coupled Plasma Atomic Emission Spectroscopy**

It is important to understand the exact elemental composition of a catalyst. While x-ray absorption works well for most elements, the lightest elements are undetectable by x-ray techniques. Inductively coupled plasma atomic emission spectroscopy (ICP-AES) is a method to determine elemental composition that is sensitive to all elements. A sample is ionized in a plasma argon flame. As ionized atoms from the sample recombine with electrons, photons are emitted. The wavelength of photons is characteristic of the element and the intensity is proportional to amount present. In particular for zeolites and other silicates, samples must first be digested with hydrofluoric acid to obtain an accurate elemental composition. This specialized ICP analysis with HF digestion requires the use of outside labs, such as Galbraith Laboratories, Inc.

## **2.2 Catalyst Testing**

### **2.2.1 Flow Reactor Design**

In this thesis, a lab scale packed bed microreactor was used to test catalyst activity for three hydrocarbon conversions. Figure 2.6 depicts the configuration of the experimental setup used in this work.

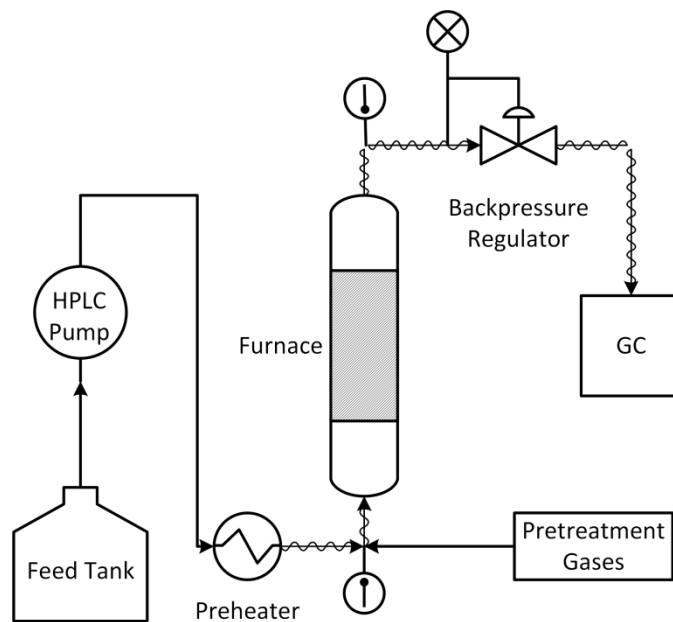


Figure 2.6: Process flow diagram of the experimental setup used for high pressure experiments

For high-pressure conversion of *n*-pentane on H-[Al]ZSM-5 (Chapter 3), a high-pressure liquid chromatography (HPLC) pump (Chromtech Series I) was used to feed pentane, which was contained in a pressurized tank (1L), into the system. Based on feed flow rates, the feed tank volume constrained reaction time on streams to under 9 hours. For high-pressure catalytic dehydrogenation of alkanes on supported molybdenum carbides (Chapter 4), two syringe pumps (Teledyne Isco 260D) equipped with switching valves, which allow continuous flow operation, were used to supply *n*-pentane, *n*-hexane, and *n*-heptane to the system. For methanol conversion on H-[Fe]Beta (Chapter 5), a single syringe pump was used to supply dimethyl ether to the system.

The system pressure was controlled by a backpressure regulator (Swagelok, KPB series). The reactor consisted of the catalyst supported by quartz wool inside a 316 SS tube (4.6 mm ID) and the catalyst bed length ranged from approximately 10 mm to 30 mm depending on the amount of catalyst used. Two thermocouples were installed, one at the bottom and one at the top of the catalyst bed, to monitor the temperature difference across the bed; the thermocouples also helped maintain the position of the bed within the reactor tube (Figure 2.7). A preheater (coiled 1/8" tube wrapped with heating tape) and tubular furnace (Lindberg Blue M) were used to control the reaction temperature. Gas transfer lines were heated to 453 K using heating tape to avoid condensation of products. The reactor effluent was analyzed using an online gas chromatograph (GC) (Agilent 7890B) equipped with a flame ionization detector (FID).

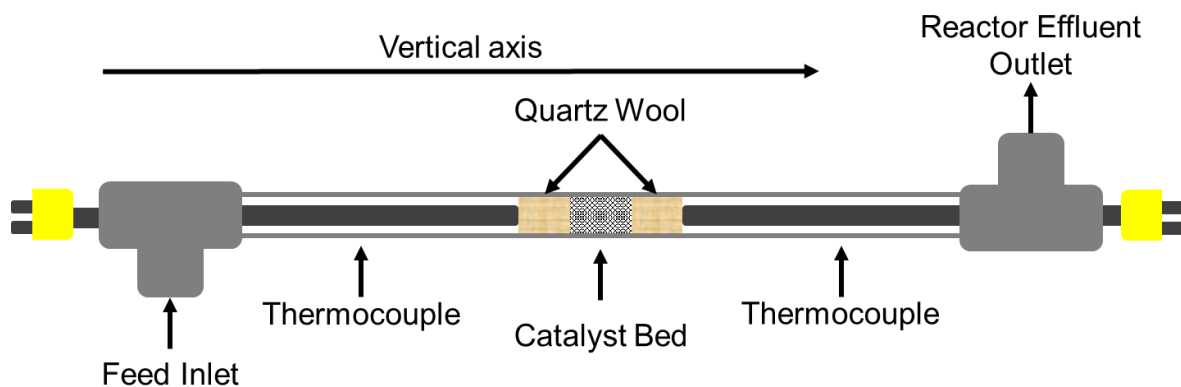


Figure 2.7: Example of reactor tube containing catalyst packed bed

### **2.2.2 Design Safety Considerations**

Before construction, strength and chemical compatibility of all materials that could come into contact with reactants and potential products must be reviewed. All tubing and valve bodies are made of 316 stainless steel (SS), which has an “excellent” chemical compatibility rating for hydrocarbons. Swagelok was the manufacturer of the tubing and valves and reports pressure ratings for each component up to a temperature of 810 K. 316 SS tubing (0.635 cm O.D.) had the lowest pressure rating at a temperature of 810 K of approximately 267 bar. This pressure rating is 4 times the highest pressure tested with the experimental setup. Chemical compatibility of seals in the valves and back-pressure regulator must also be considered. All valves had polytetrafluoroethylene (PTFE) seals, which are resistant to hydrocarbons, and the back-pressure regulator had high temperature, chemically resistant Kalrez seals.

After ensuring no undesirable reactions will occur with materials used to construct the experimental setup and those materials are structurally sound under experimental conditions, steps must be taken to avoid over pressurization. A pressure relief valve was installed with a relief setting 10% greater than highest pressure tested. Pumps which supply reactants to the system were programmed to turn off in case of over-pressurization. Finally, connections were leak tested by pressurizing the experimental setup with inert nitrogen and a flammables leak detector was used during experimental testing to ensure no leaks had formed.

### **2.2.3 Chromatography**

Chromatography is an analytical technique used to separate chemical compounds in a feed stream. In the experimental setup, the feed stream is the effluent of the reactor and a gas chromatograph (GC) is used for analysis. Reactor effluent is

constantly fed through a sample loop (150  $\mu\text{L}$ ) in a 6-way valve. When an injection is taken, the contents of the sample loop are introduced to a GC column with helium, which is a diluent and mobile phase. A GC column consists of a stationary phase with which the compounds of the reactor effluent interact. Stronger interaction of a compound with the stationary phase results in increased time it takes for a compound to elute out of the GC column creating the separation needed for analysis. After leaving the GC column, compounds are analyzed with a flame ionization detector (FID).

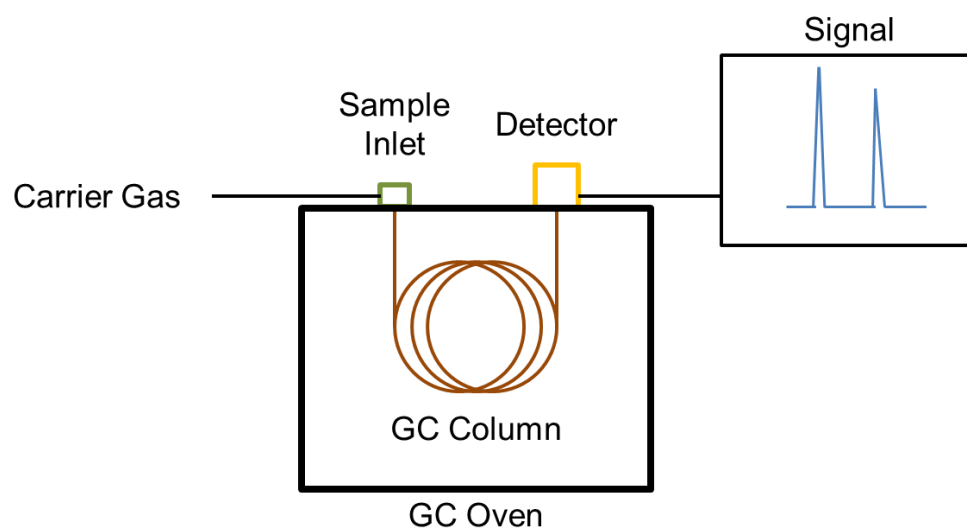


Figure 2.8: Simplified schematic of gas chromatograph

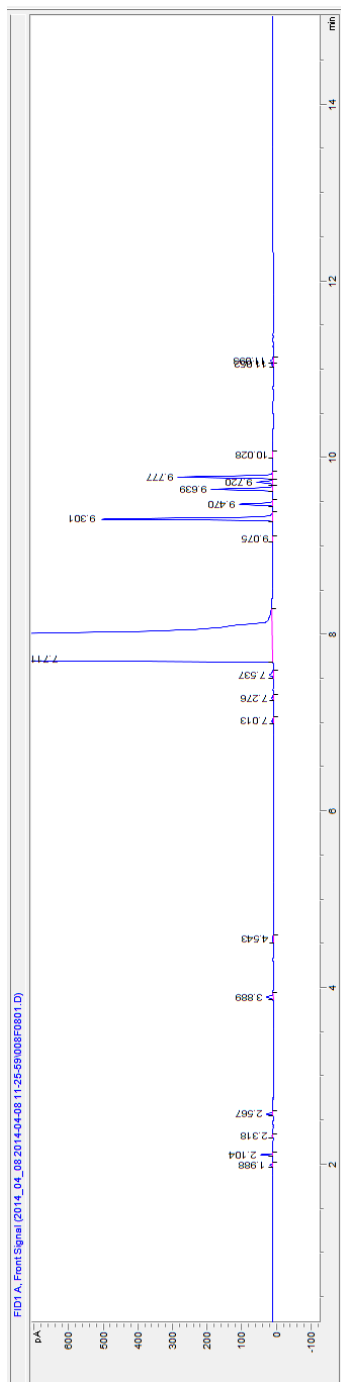


Figure 2.9: Example GC chromatogram from catalytic dehydrogenation of *n*-pentane using a polar alumina column for separation

A FID consists of a hydrogen-fueled flame that burns the compounds as they leave the GC column. Burning of hydrocarbons creates charged ions that pass through a pair of electrodes creating a current. Measured current is proportional to the amount of a compound and strongly influenced by carbon number of the compound. Because FID analysis relies on combustion, only hydrocarbons can be analyzed. Another common detector utilized is a thermal conductivity detector (TCD) which can be added to detect non-hydrocarbon compounds, such as hydrogen and carbon dioxide. A TCD operates by detecting the decrease in thermal conductivity of the mobile phase (usually argon or helium) and is proportional to the concentration of the compound present.

#### **2.2.4 Mass Spectrometry**

Mass spectrometry (MS) uses electrons to break apart molecules and measures mass to charge ratios of the fragments formed. Hard ionization causes extensive fragmentation of the parent molecule and the resulting fragmentation pattern acts as a “fingerprint”. Comparing this “fingerprint” to fragmentation pattern databases allows for identification of the parent molecule. Mass spectrometry is commonly paired with gas chromatography, where GC provides separation and quantification and MS provides identification of the compound.

## Chapter 3

### CATALYTIC *n*-PENTANE CONVERSION ON H-ZSM-5 AT HIGH PRESSURE

In this chapter, catalytic conversion of *n*-pentane on H-[Al]ZSM-5 is discussed as a potential reactant/catalyst system for aircraft endothermic cooling. H-[Al]ZSM-5 is a strong solid acid catalyst utilized in a variety of hydrocarbon conversions. Specifically, cracking reactions were targeted with the production of light olefins ethylene and propylene.

#### 3.1 Introduction

This investigation is motivated by the need to develop more efficient cooling technologies for the practical use of new hypersonic engines. The flight of aircraft and missiles at hypersonic speeds (greater than Mach 5) is hindered by overheating of the engine and electronic components caused by the high rate of fuel combustion and air friction [63]. Aircraft are currently cooled by passive and active methods: when passive cooling is used, cold air from the atmosphere is passed through the engine, whereas when active cooling is used, onboard jet fuel is used as a heat sink [64]. In such cases, the maximum amount of heat that can be removed is determined by the heat capacity, thermal stability, and initial temperature of the fuel. Chemical additives (e.g. 1,2,3,4-tetrahydroquinoline and tetralin) and special fuels (e.g. exo-tetrahydrodicyclopentadiene) with greater heat capacity and thermal stability have been designed for this purpose, but future hypersonic vehicles will exceed the cooling capacity of these special fuels [65,66].

Cooling capacity can be improved by utilizing so-called *endothermic fuels*, which undergo endothermic chemical reactions driven by the thermal energy removed from the aircraft [67,68] and a target endothermic reaction is the cracking of hydrocarbons on solid catalysts. For several decades, zeolites have been used as catalysts for cracking of crude oil [69,70], but there are only a few reports of zeolite-based high-pressure cracking for endothermic fuel applications [71–74]. To maximize endothermicity, the selective cracking of alkanes to produce an alkene and a smaller alkane is the preferred reaction. It is also desired to further crack the alkene and alkane to produce hydrogen, ethene, and methane, as these have better mixing and combustion characteristics than larger molecules [75].

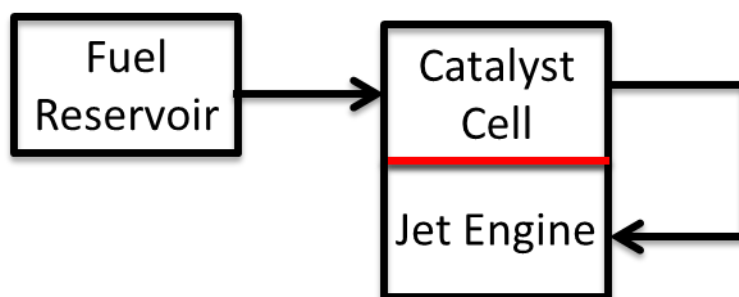


Figure 3.1: Simplified process flow diagram for proposed aircraft endothermic cooling

Zeolite catalyzed cracking of alkanes proceeds via two major mechanisms: monomolecular and bimolecular [76]. Monomolecular (i.e. protolytic) cracking reactions typically occur at low pressures and high temperatures [77–83]. In this mechanism, a proton from the zeolite acid site is transferred to the adsorbed alkane to form a pentacoordinated alkanium ion that immediately undergoes protolytic cracking to form a neutral paraffin or molecular hydrogen and a surface alkoxide. The surface

alkoxide can desorb to produce an olefin and reform the zeolite acid site [84–88]. This sequence leads to a predictable, but approximate, product distribution. For example, the protolytic cracking of butane can only yield three product pairs: hydrogen and butene, methane and propene, or ethane and ethene. Surface alkoxides can also undergo further cracking through  $\beta$ -scission reactions.

Alkoxides may also participate in bimolecular reactions, such as hydride transfer, oligomerization, and alkylation [70]. In bimolecular reactions, a molecule in the gas phase reacts with a chemisorbed olefin on the surface of the zeolite. The simplest way to detect bimolecular reactions is to observe molecules that cannot be formed from monomolecular cracking; for example, the production of pentane from hexane. Methane and pentene can be produced from protolytic cracking of hexane. Pentene then can be converted to pentane through hydride transfer. Pentane can also be formed by cracking larger molecules that formed through oligomerization.

There have been a few investigations of the supercritical cracking of hydrocarbons on zeolites. Dardas et al. investigated the effects of supercritical pressures on the conversion and selectivity of *n*-heptane cracking on Y-type zeolites. The supercritical pressures increased the conversion and paraffin yield and decreased the amount of deactivation observed when compared to subcritical pressures [71]. Xian et al. studied supercritical cracking of *n*-dodecane on wall-coated H-[Al]ZSM-5 catalysts and reported that nanocrystalline catalyst particles produced higher conversions and higher selectivity to ethylene and propylene than microcrystal size particles [72]. Kim et al. found that high pressure conversion of methylcyclohexane on H-[Al]ZSM-5 yielded higher heats of reactions as compared to H-[Al]Beta and H-[Al]Y [89]. Luo et al. have investigated the cracking of *n*-hexane on various zeolites.

H-[Al]ZSM-5 exhibited a higher pressure dependency on rates and higher activation energies than H-[Al]USY, H-[Al]Mordenite, and H-[Al]Beta, but had better selectivity towards olefins and lower susceptibility to deactivation [73,74]. In addition, the cracking of hexane on ZSM-5 exhibited monomolecular-like reaction kinetics under all pressures, but at high pressures on USY, mordenite, and zeolite beta, bimolecular reactions were the dominant reaction channels. Finally, Wang et al. found that heavily branched *iso*-dodecane (mainly 2,2,4,6,6-pentamethylheptane) could affect conversion of *n*-dodecane on H-[Al]ZSM-5 by acting as an inert diluent (positive) or by resisting diffusion (negative) [90].

The solid acid zeolite H-[Al]ZSM-5 was chosen as the catalyst because it is thermally stable, readily available, and known to increase the yield of light olefins in industrial fluidized catalytic cracking units [91]. Pentane was selected because it is the simplest liquid hydrocarbon at STP and has a high cooling potential (pentane cracking to ethane and propylene has a heat of reaction of 1.15 MJ/kg). In addition, *n*-pentane cannot form neutral aromatic species by cyclization and dehydrogenation without molecular weight growth [92]. It was found that under all reaction conditions investigated, bimolecular reactions were the dominant reaction channels for the high-pressure conversion of pentane on H-[Al]ZSM-5. Smaller alkanes (C<sub>3</sub>, C<sub>4</sub>) with higher H/C ratios than pentane were produced, while larger species (C<sub>6+</sub>) with lower H/C ratios than pentane were necessarily produced to close the hydrogen and carbon balance. This group of products has lower endothermic potential than direct monomolecular cracking of the alkane.

## 3.2 Experimental Section

### 3.2.1 Materials

NH<sub>4</sub>-[Al]ZSM-5 (CBV3024E) was purchased from Zeolyst International and the material was used without further treatment for the catalytic investigations. *n*-pentane (Fisher, 99.7% purity) was used as the feed for the catalytic tests. The following gases were used for calcination and gas chromatograph operation: Air (Keen, Grade 0.1), Nitrogen (Keen, Grade 5.0), Hydrogen (Keen, Grade 5.0), and Helium (Keen, Grade 5.0).

### 3.2.2 Characterization

Solid state <sup>29</sup>Si MAS NMR (99.83 MHz, 10 kHz rotational speed, 2048 scans, and 30 s relaxation delay) and <sup>27</sup>Al MAS NMR (130.29 MHz, 10 kHz rotational speed, and 512 scans) spectra of hydrated NH<sub>4</sub>-[Al]ZSM-5 were recorded with a Bruker AVIII500 NMR spectrometer. Surface area and micropore volumes (calculated using the t-plot method) were determined through N<sub>2</sub> adsorption isotherms measured using a Micromeritics ASAP 2020 instrument. The samples were pretreated at a temperature of 623 K and a reduced pressure of 0.5 torr for 6 h to remove any adsorbed species. Powder X-ray diffraction patterns (PXRD) were measured using a Phillips X'Pert X-ray diffractometer with a CuK $\alpha$  source ( $\lambda = 1.542 \text{ \AA}$ ). Diffraction patterns were obtained using a step size of 0.02° 2 $\Theta$  with 2 s counting time at each step. Diffraction patterns were measured between 5° and 50° 2 $\Theta$ . SEM images were taken with a JSM-7400F scanning electron microscope with an accelerating voltage of 3.00 kV. Zeolite chemical compositions were determined through inductively coupled plasma mass spectrometry (ICP-MS) from Galbraith Laboratories, Inc.

### 3.2.3 Catalytic Testing

The catalyst powder was pressed, gently crushed and sieved to particle sizes between 250 and 425  $\mu\text{m}$  (40 – 60 mesh). Each experiment was performed using 50 mg of catalyst powder. Prior to each experiment, the catalyst was calcined *in situ* at a temperature of 823 K for 5 hours in zero air (Keen, 60 mL/min). A variety of reaction conditions were investigated: pressure was investigated up to 60 bar and reaction temperature was studied in the range of 633 – 723 K. Most experiments were performed in the supercritical regime of *n*-pentane ( $T_c = 470$  K and  $P_c = 34$  bar)[93]. The weight hourly space velocity (WHSV, defined as grams of pentane fed per gram of catalyst per hour) ranged from 375 – 1500  $\text{g}_{\text{C5}}\text{g}_{\text{cat}}^{-1}\text{h}^{-1}$  and was controlled by changing the pentane liquid flow rates in the range of 0.5 - 2.0 mL/min. Conversion of *n*-pentane was defined as 100% minus the percentage of unreacted pentane (all isomers included) in the product stream. Product carbon selectivity was defined as the fraction of carbon (*C*) in each product (*i*) as compared to the total amount of carbon in the effluent that was not pentane.

$$\textit{Selectivity} = \frac{C_i}{\sum_{i=1}^{i=n} C_i} \quad (\text{Eq. 3.1})$$

Product analysis was performed via online GC analysis. Separation of chemical species within the reactor effluent was performed in the GC with an Alumina column (Agilent, 50 m x 530  $\mu\text{m}$  ID). Helium was used as the carrier gas and nitrogen was used as the makeup gas. The following temperature program was used for product detection: a 5 minute hold at 373 K, a ramp to 473 K at a rate of 20 K/min, and a final 30 min hold at 473 K.

### 3.3 Results

The conversion of *n*-pentane over zeolite H-[Al]ZSM-5 (Si/Al = 15) was investigated considering the effect of temperature (633-723 K), pressure (10-60 bar), and weight hourly space velocity (WHSV) (375-1500 g<sub>C5</sub>g<sub>cat</sub><sup>-1</sup>h<sup>-1</sup>). The reaction kinetics were measured using a packed-bed laboratory microreactor and reaction products were analyzed via online gas chromatography.

#### 3.3.1 Catalyst Characterization

The XRD patterns of the zeolite samples showed that the zeolite samples were highly crystalline and did not reveal the presence of any amorphous material or other crystalline impurities. The SEM image (Figure 3.2) shows that the material was an aggregate of particles smaller than 2 μm. Presence of only one signal at 55 ppm on the <sup>27</sup>Al MAS NMR spectra of the hydrated samples showed that nearly all aluminum atoms were in tetrahedral coordination (Figure 3.2). Only a small fraction (1%) was observed near 0 ppm and was assigned to extra-framework octahedral aluminum. The nominal Si/Al ratio of this commercial sample determined by ICP (Si/Al = 15.7) was consistent with the aluminum concentrations determined by other studies on similar samples (Si/Al = 15-17) [77,94]. <sup>29</sup>Si MAS NMR spectra from this sample indicated that the sample contained predominantly Si(4Si) groups and 4.2% of Si(3Si, Al), resulting in an estimated framework Si/Al of 23. The aluminum concentration is slightly less than the amount observed by ICP, and confirms that only a small fraction of the Al is located in extra-framework positions.

The micropore volume, obtained from N<sub>2</sub> adsorption isotherms and analyzed using the t-plot method, was 0.11 cm<sup>3</sup>/g. This micropore volume is slightly smaller than observed for high quality samples (usually ~0.14 cm<sup>3</sup>/g) and suggest that some

extra-framework species may be present in the zeolite pores or that a non-porous phase (undetected by XRD) is present in the sample. The observed BET surface area ( $380 \text{ m}^2/\text{g}$ ) and micropore volume are in agreement with previous reports for the same material [94].

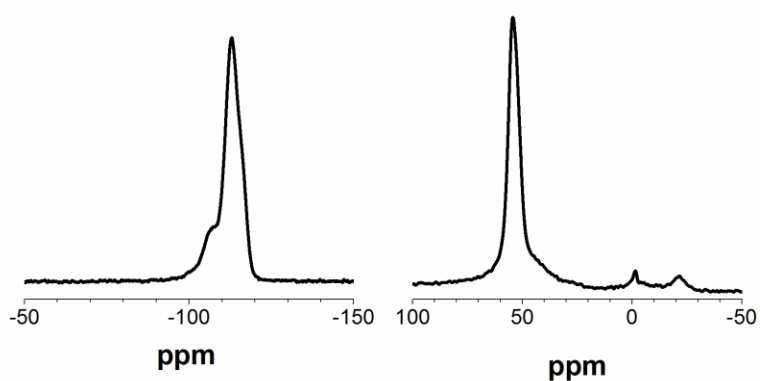
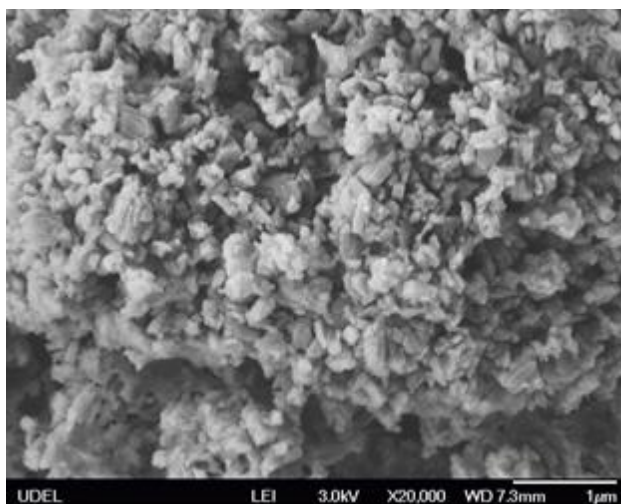


Figure 3.2: SEM image of CBV3024E (*top*),  $^{29}\text{Si}$  NMR (*left*), and  $^{27}\text{Al}$  NMR (*right*) of the ZSM-5 catalyst.

### 3.3.2 Catalytic Conversion of *n*-Pentane

Conversion of *n*-pentane on H-[Al]ZSM-5 at high pressures was performed in a packed-bed reactor. Reactor effluent was analyzed via an online GC with injections being taken approximately every 40 min. As seen in Figure 3.3, reactor conversion remained stable during the 6 h of time on stream at temperatures up to 673 K. Deactivation was observed at temperatures above 673 K, with the greatest amount at the highest reaction temperature of 723 K. Conversion and selectivity data were calculated from the average of the GC measurements over the 6.5 h time on stream.

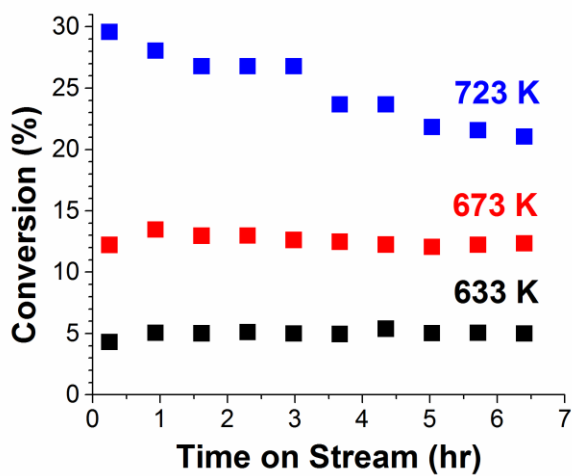


Figure 3.3: Conversion of *n*-pentane over 6.5 h time on stream during high pressure conversion on H-[Al]ZSM-5. Reaction conditions:  $T = 633 - 723$  K,  $P = 40$  bar, and  $\text{WHSV} = 1120 \text{ g}_{\text{C}_5\text{g}_{\text{cat}}^{-1}\text{h}^{-1}}$

Figure 3.4 shows the conversion of *n*-pentane and product carbon selectivity at temperatures between 633 K and 723 K ( $P = 40$  bar and  $\text{WHSV}$  of  $1120 \text{ g}_{\text{C}_5\text{g}_{\text{cat}}^{-1}\text{h}^{-1}}$ ). Conversion increased rapidly with increasing temperature. The major products of the

reaction were propane and butane (~6:4 *n:iso* isomeric ratio). At all experimental conditions investigated, the selectivity to methane, ethane, ethene, propene and butenes was low (<10%), hence these fractions were combined and reported as ‘lights’. This fraction never exceeded 10% of the overall carbon in the product stream. A typical carbon composition of the lights was 1% methane, 5-10% ethane, 4-8% ethylene, 20-30% propylene, and 50-70% butenes. As temperature increased, selectivity to propane increased, while selectivity to butane remained nearly constant. On the other hand, selectivity to higher molecular weight products ( $C_{6+}$ ) decreased with increasing temperature. A small (<2%) increase in selectivity to light products was observed with increasing temperature.

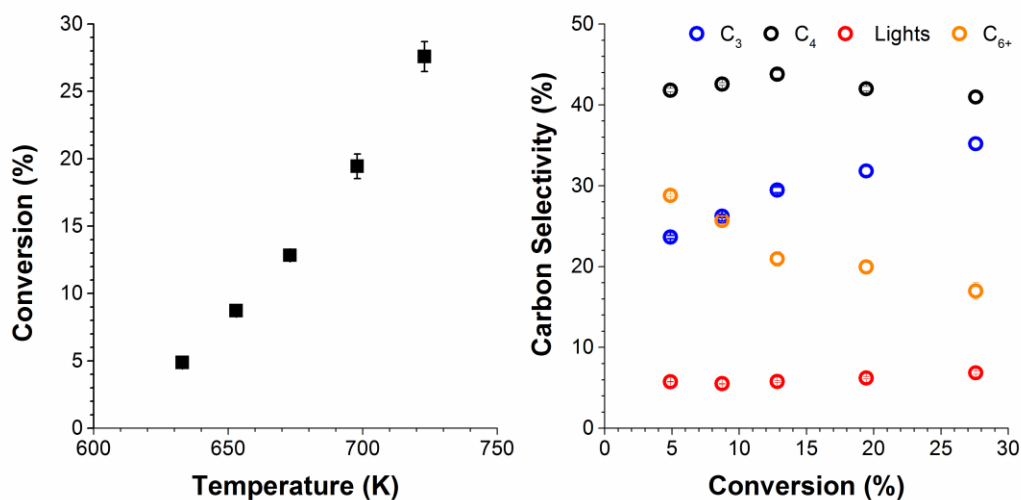


Figure 3.4: Conversion of *n*-pentane (*left*) and selectivity to product groups (*right*) during high pressure conversion on H-[Al]ZSM-5. Reaction conditions:  $T = 633 - 723$  K,  $P = 40$  bar, and  $WHSV = 1120$   $g_{C5}g_{cat}^{-1}h^{-1}$

Clear changes in conversion and carbon selectivity were observed as the pressure was increased at a temperature of 673 K and  $\text{WHSV} = 1120 \text{ g}_{\text{C}_5}\text{g}_{\text{cat}}^{-1}\text{h}^{-1}$ . Increasing the pressure of the system from 10 bar up to a total pressure of 30 bar, which is before the transition to the supercritical phase (34 bar), caused an increase in conversion. Further increases in pressure up to 60 bar did not increase the total conversion of pentane. Pressure changes had little effect on carbon selectivity of the major products: propane and butane. Conversely, increases in pressure decreased selectivity to the light products and increased selectivity to the  $\text{C}_{6+}$  fraction.

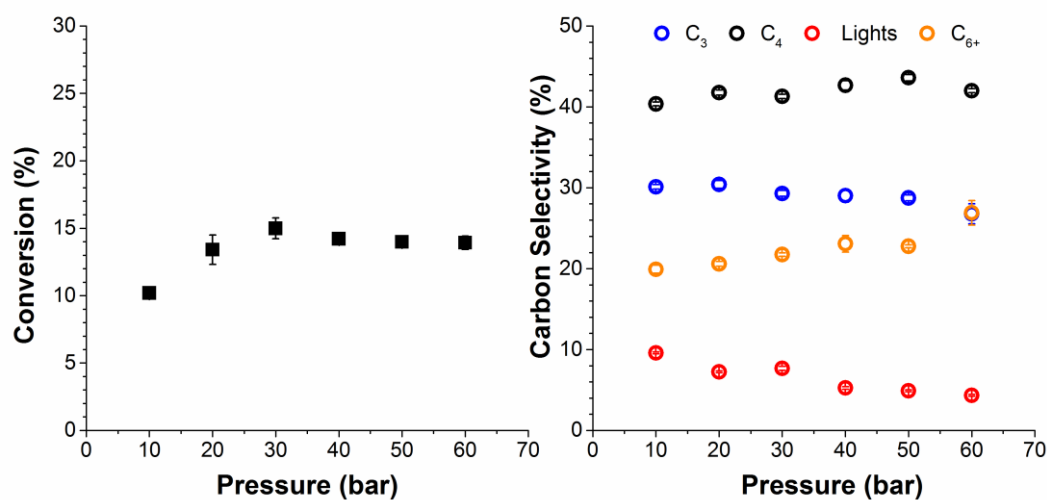


Figure 3.5: Conversion of *n*-pentane (*left*) and selectivity to product groups (*right*) during high pressure conversion on H-[Al]ZSM-5. Reaction conditions:  $T = 673 \text{ K}$ ,  $P = 10 - 60 \text{ bar}$ , and  $\text{WHSV} = 1120 \text{ g}_{\text{C}_5}\text{g}_{\text{cat}}^{-1}\text{h}^{-1}$

Figure 3.6 shows the conversion and carbon selectivity during the *n*-pentane reaction at a temperature of 673 K and a pressure of 40 bar as a function of WHSV ( $375 - 1500 \text{ g}_{\text{C}_5}\text{g}_{\text{cat}}^{-1}\text{h}^{-1}$ ). Conversion of pentane increased with decreasing WHSV, or in other words, increased as the residence time increased. Selectivity of the major products (propane and butane) and  $\text{C}_{6+}$  fraction did not change appreciably with changes in WHSV, but carbon selectivity of the light products increased with increasing WHSV.

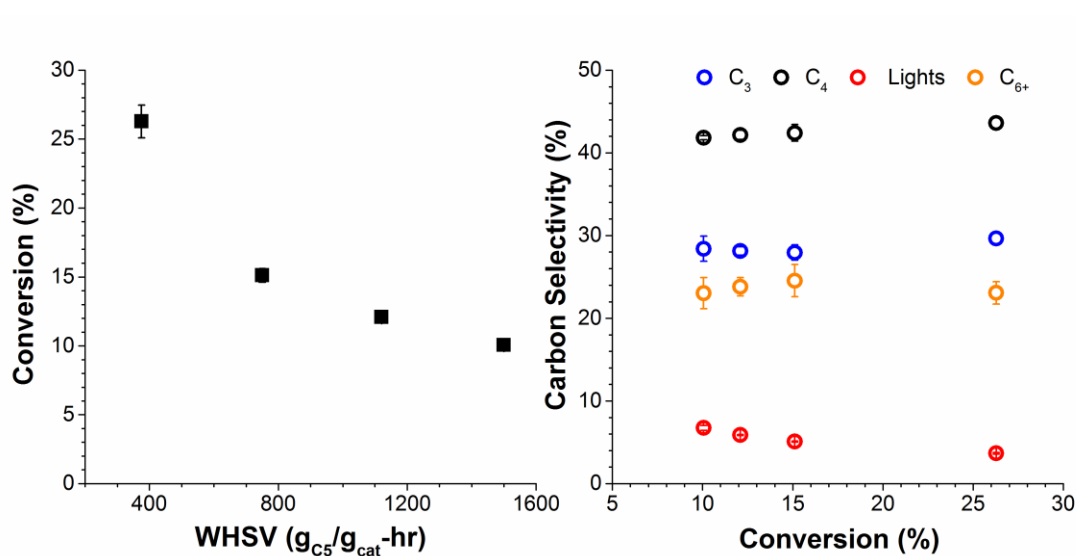


Figure 3.6: Conversion of *n*-pentane (*left*) and selectivity to product groups (*right*) during high pressure conversion on H-[Al]ZSM-5. Reaction conditions:  $T = 673 \text{ K}$ ,  $P = 40 \text{ bar}$ , and  $\text{WHSV} = 375 - 1500 \text{ g}_{\text{C}_5}\text{g}_{\text{cat}}^{-1}\text{h}^{-1}$

### 3.4 Discussion

The formation of more than 50 different species upon the reaction of *n*-pentane on H-[Al]ZSM-5, including many compounds heavier than pentane, is clear evidence of secondary bimolecular reactions controlling the product distribution at high

pressure. In addition, the ratios of  $C_3/C_2$  and  $C_4/C_1$  products were greater than 1 under all conditions, which further indicates a role of bimolecular reactions in the catalyst. If monomolecular cracking were occurring, the average H/C ratio of the cracked products would equal that of the feed (*n*-pentane H/C = 2.4), while the average H/C of products lighter than pentane was between 2.5 – 2.6. Since the observed  $C_1$ - $C_5$  species had an average H/C greater than the feed, either the olefins produced from monomolecular cracking were consumed in secondary reactions or the paraffins were produced via a reaction other than *n*-pentane cracking.

The consumption of olefins lighter than pentane through secondary bimolecular reactions is consistent with changes in the carbon selectivity of the light olefins: ethene, propene, and butene (Figure 3.7). Carbon selectivity of the light olefins decreased with increasing pressure, with the change being most clear at pressures below ~ 30 bar, where pentane is gas-like. Although pentane conversion did not change above 30 bar, product selectivity continued to change with increasing pressure. Elevated pressures promote oligomerization of olefins [95–97], a reaction also observed here. Increasing pressure decreased light olefin production and increased formation of  $C_{6+}$  compounds. Although elevated pressures promote oligomerization, the larger compounds in the  $C_{6+}$  fraction eventually become more reactive and crack at high temperatures as seen in Figure 3.4. As reaction temperature increases, cracking rates of the  $C_{6+}$  fraction become greater than oligomerization rates, leading to an increase in the production of propane. Carbon selectivity of the light olefins also increased with increasing WHSV. With less time to react, a greater percentage of light olefins formed through monomolecular cracking of pentane survived without undergoing further bimolecular reactions. From the observed trends

in carbon selectivity of the light olefins, a simplified reaction network can be proposed to illustrate the formation of the major products: propane and butane.

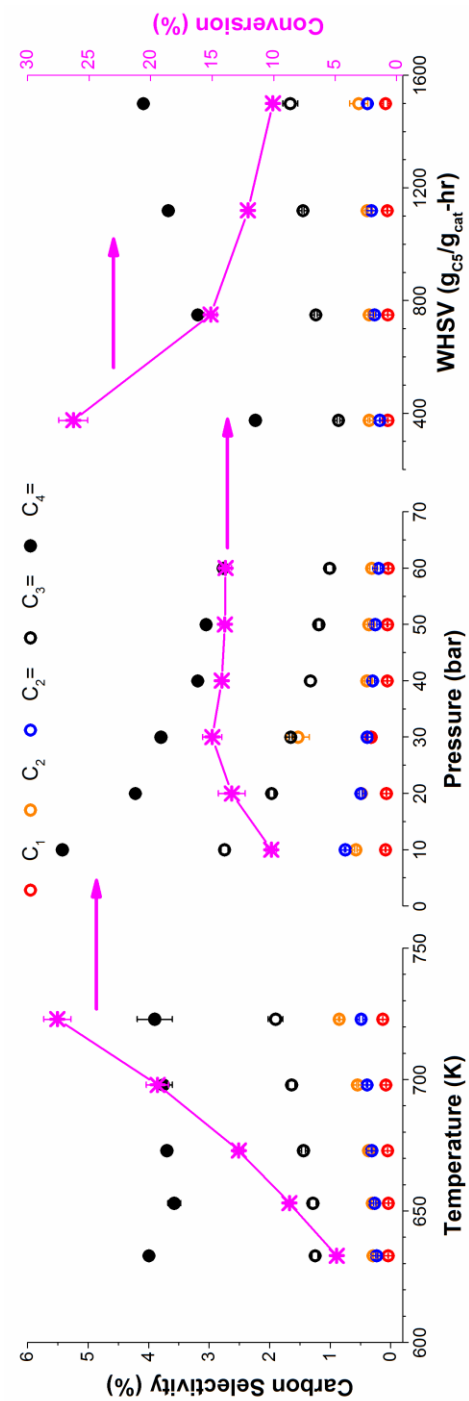


Figure 3.7: Selectivity of products within the lights fraction at various temperatures (*left*), pressures (*middle*), and WHSV (*right*). Reaction conditions:  $T = 633 - 723 \text{ K}$ ,  $P = 10 - 60 \text{ bar}$ , and  $\text{WHSV} = 375 - 1500 \text{ g}_{\text{C}_5}/\text{g}_{\text{cat}}\text{-hr}^{-1}$

Figure 3.8 displays a simplified reaction network consistent with the observed formation of propane and butane. After protolytic cracking of *n*-pentane, propene and ethane are formed and the propene then can react with another pentane via hydride transfer. This forms one of the major products, propane. The pentene can crack via beta scission to form another molecule of propene and ethene. Any ethene that is formed can dimerize to form butene. The butene can react with another pentane via hydride transfer yielding the second major product, butane. Through oligomerization, compounds heavier than pentane can form and subsequently crack to form lighter products or cyclize and aromatize. In reality, a more complex reaction network of monomolecular and bimolecular reactions exists, as evidenced by the product distribution and trends in activation energy.

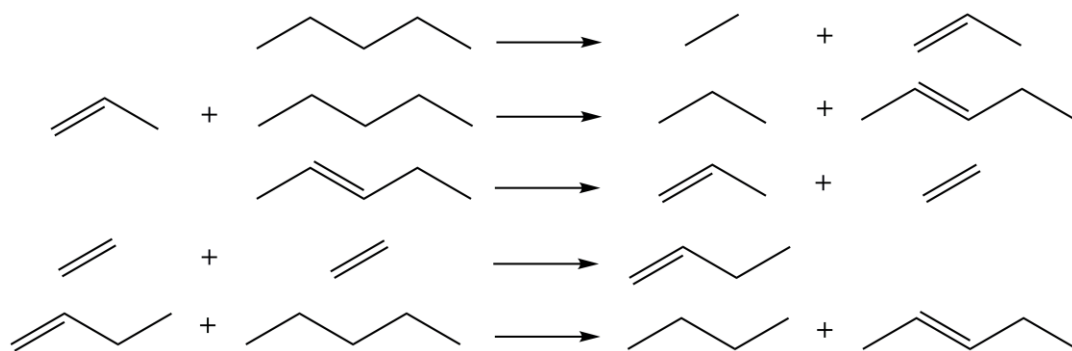


Figure 3.8: Simplified reaction network demonstrating the production of propane and butane

If monomolecular cracking were the dominant reaction channel, as pressure increases, the apparent activation energy should also increase and approach the

intrinsic activation energy. This trend occurs because saturation kinetics are reached at elevated pressures, reducing the effect of adsorption enthalpy on the apparent activation energy [73]. As seen in Figure 3.9, the apparent activation energy based on consumption of *n*-pentane decreases with increasing pressure, which is opposite of the expected trend for monomolecular cracking. Furthermore, Luo et al. reported the intrinsic activation energy of *n*-hexane cracking on ZSM-5 to be 170 kJ/mol, while Gounder et al. reported the intrinsic activation energy of propane cracking on ZSM-5 to be 204 kJ/mol [73,77]. Based on these observations, it is expected that the activation energy above the saturation pressure of *n*-pentane (>30 bar) to be near those of propane and hexane [77]. At 40 bar, the apparent activation energy for the consumption of *n*-pentane was 86 kJ/mol, which was much less than expected for monomolecular cracking, but consistent with the results obtained using other zeolite frameworks as solid acid catalysts.

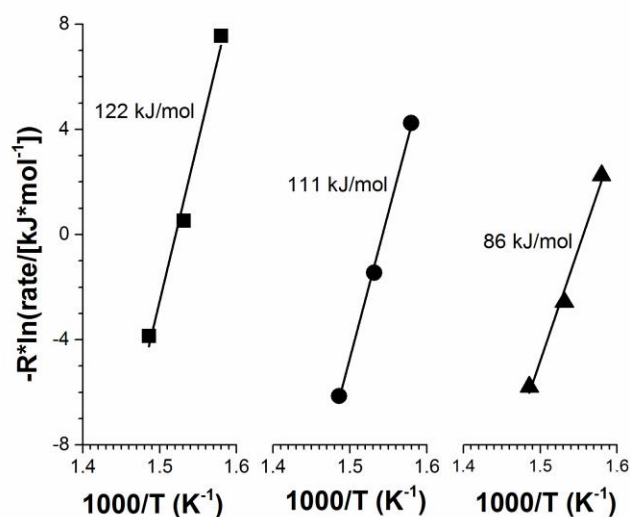


Figure 3.9: Activation energies at 10 bar (*square*), 20 bar (*circle*), and 40 bar (*triangle*). Reaction conditions:  $T = 633 - 673 \text{ K}$ ,  $P = 10 - 40 \text{ bar}$ , and  $\text{WHSV} = 1120 \text{ g}_{\text{C5}}\text{g}_{\text{cat}}^{-1}\text{h}^{-1}$

Luo et al. recently investigated the high pressure cracking of *n*-hexane on H-USY, H-Beta, and H-Mordenite. In the work, the apparent activation energy for cracking on zeolite beta (63 kJ/mol) and USY (55 kJ/mol) did not change with pressure, while the apparent activation energy on mordenite decreased from 77 kJ/mol at 1 bar to 66 kJ/mol at 137 bar [74]. The activation energies observed from the cracking of hexane on USY, zeolite beta, and mordenite are consistent with those for the cracking of *n*-pentane on ZSM-5, but differ from the cracking of *n*-hexane on ZSM-5.

Luo et al. also investigated the product selectivity for the cracking of *n*-hexane on ZSM-5 [74]. With increasing conversion under isothermal conditions, an increase in selectivity to higher molecular weight species was observed. For the conversion of *n*-pentane on ZSM-5, increasing conversion under isothermal conditions did not result

in any significant change in selectivity to higher molecular weight species. However, there were two trends in product selectivity that were similar between the conversion of pentane and hexane on ZSM-5. First, the major products of hexane conversion were butanes and pentanes, analogous to propane and butanes for pentane conversion. Second, increasing pressure caused a decrease in selectivity to light olefins for the conversion of both pentane and hexane on ZSM-5.

The decrease in activation energy with increasing pressure is evidence of a shift from a higher activation energy reaction channel to a lower activation energy reaction channel. While the conversion of pentane and hexane on ZSM-5 have similar trends in product selectivity with changing pressure, the differences in apparent activation energy suggest the conversion occurs via alternative reaction pathways.

### 3.5 Conclusions

The high selectivity (>70%) to propane and butane, along with the observed changes in the selectivity to lights and C<sub>6+</sub> compounds, indicate that bimolecular reactions, such as hydride transfer and alkylation, control product distribution. While the product distribution from the high pressure conversion of pentane resulted in an endothermic process, hydride transfer reactions led to the transformation of high energy olefins into lower energy paraffins and aromatics, resulting in a decrease of the process endothermicity from a target of 1.1 MJ/kg of *n*-pentane converted to an estimated 0.6 MJ/kg. Hydride transfer occurs readily on H-[Al]ZSM-5 and other zeolites, and an alternative catalyst that suppresses these reactions should improve selectivity to light olefins, which will increase cooling capacity of the endothermic fuel.

## Chapter 4

### HIGH-PRESSURE CATALYTIC DEHYDROGENATION OF ALKANES ON MOLYBDENUM CARBIDE SUPPORTED ON METAL OXIDES AND LOW-ACIDITY ZEOLITES

In this chapter, high-pressure dehydrogenation of *n*-pentane, *n*-hexane, and *n*-heptane on supported molybdenum catalysts was investigated as an alternative to high-pressure cracking on H-[Al]ZSM-5 for endothermic cooling applications.

Dehydrogenation of alkanes is preferable to cracking as the reaction is more endothermic (pentane cracking to ethane and propene has a heat of reaction of 1.15 MJ/kg, whereas pentane dehydrogenation to hydrogen and *trans*-2-pentene has a heat of reaction of 1.59 MJ/kg) and dehydrogenation catalysts do not promote secondary bimolecular reactions that lead to molecular weight growth.

#### 4.1 Introduction

Practical use of hypersonic vehicles has been hindered by overheating of aircraft engines and electronic components caused by high fuel combustion rates and air friction [63]. Military aircraft use onboard jet fuel as a heat sink, but future hypersonic aircraft will exceed the cooling capacity of the fuel [65,66]. Cooling capacity can be increased using endothermic fuels, which remove heat through endothermic chemical reactions [67,68]. Based on the design and operating conditions of jet engines, future use of endothermic fuels will require the reactions to take place under high pressure. Conversion of *n*-pentane and *n*-hexane on H-[Al]ZSM-5 has been investigated as a system for endothermic cooling applications [73,74,98]. While

reaction rates are high, the desired olefinic products are consumed via secondary, bimolecular reactions, such as oligomerization and dehydroaromatization, which led to a decrease in reaction endothermicity. By utilizing catalytic dehydrogenation instead of catalytic cracking, selectivity to light olefins should be increased resulting in increased reaction endothermicity.

Two major types of catalysts are used for catalytic dehydrogenation: platinum-based and chromia-based [99]. Platinum is desirable because it can selectively activate C-H bonds over C-C bonds [100]. Activity, selectivity, and stability are further enhanced by addition of tin as a promoter [101–105]. Supported chromia catalysts have been used industrially since World War II [106], and while they have been studied extensively, the oxidation state of the active species and reaction mechanism are still unknown [107]. While these two catalysts have been used industrially for decades, a number of issues affect these catalysts, including susceptibility to poisoning, high cost of platinum, and toxicity of chromia, creating an opportunity to discover suitable alternatives [100].

Besides chromia-based catalysts, vanadium oxide, gallium oxide, and molybdenum oxide, have also been shown to catalytically dehydrogenate alkanes [108–110]. Similarly to chromia, Lewis acid dopants are added to increase stability and reduce the amount of Brønsted acid sites, resulting in increased selectivity, but at the cost of reduced conversion [100]. Additionally, CO<sub>2</sub> is co-fed as a mild oxidant to remove coke precursors and to react with surface hydrogen via the reverse water-gas shift reaction, increasing conversion [111,112]. Of these transition metal oxides, molybdenum has potential for dehydrogenation if it is converted into molybdenum carbide.

Density-functional theory calculations have shown transition metal carbides to have an electronic structure resembling platinum, leading to their ability to catalyze similar reactions [113,114]. Molybdenum carbide based catalysts have shown to catalyze a variety of reactions including cracking, dehydrogenation, cyclization, and hydrodeoxygenation [115,116]. Solymosi et al., for example, has shown that bulk  $\text{Mo}_2\text{C}$  and  $\text{Mo}_2\text{C}/\text{SiO}_2$  catalyze the dehydrogenation and cyclization of hydrocarbons up to octane [117,118]. Molybdenum carbide also catalyzes the hydrodeoxygenation of a variety of biomass-derived compounds [119].

Methane dehydroaromatization on  $\text{Mo}_2\text{C}/\text{H}-[\text{Al}]\text{ZSM}-5$  is a potential method to produce aromatics from less expensive methane [120]. Molybdenum carbide anchored within the pores of the zeolite catalyzes the carbon-carbon coupling of methane to produce ethene and hydrogen [16,121]. Ethene then reacts on a Brønsted acid site within the zeolite pores through a series of oligomerization, isomerization, cyclization and dehydrogenation reactions to produce aromatic species [122,123]. If the strong Brønsted acid site created by incorporating aluminum into the framework were removed, the catalytic activity of molybdenum carbide could be isolated. Incorporating boron into the framework instead of aluminum creates an acid site that is much weaker and may afford a mechanism for anchoring molybdenum carbide precursors without the generation of strong acid sites [49,124–126].

It was found that under high-pressures, dehydrogenation of *n*-pentane on  $\text{Mo}/\gamma\text{-Al}_2\text{O}_3$  and  $\text{Mo}/\text{H}-[\text{B}]\text{ZSM}-5$  produced pentenes with up to 90% selectivity, while  $\text{Mo}/\text{H}-[\text{B}]\text{ZSM}-5$  exhibited consumption rates more than two times higher than  $\text{Mo}/\gamma\text{-Al}_2\text{O}_3$ . As the molecular weight of the feed increased, selectivity to the primary dehydrogenation product decreased, while selectivity to all olefins lighter than the

feed remained nearly constant. Dehydrogenation was the primary reaction pathway, leading to an increase in reaction endothermicity in comparison to cracking on H-[Al]ZSM-5. The role of framework Al acid sites is confirmed since Mo/H-[B]ZSM-5 produced benzene in only minute amounts.

## 4.2 Experimental Section

### 4.2.1 Materials

*n*-pentane (Fisher, 99+% purity), *n*-hexane (Acros, 99+% purity), and *n*-heptane (Fisher, 99+% purity) were used as received. For calcination, carburization, and gas chromatograph operation, the following gases were used: Air (Keen, Grade 0.1), Helium (Keen, Grade 5.0), Hydrogen (Keen, Grade 5.0), Methane (Matheson, Grade 5), and Nitrogen (Keen, Grade 5.0).

Zirconia (99% trace metals, Sigma Aldrich) and magnesia (99.999%, Sigma Aldrich) were used as received for molybdenum impregnation.  $\gamma$ -Alumina (10 g, Alfa Aesar) was washed overnight at a temperature of 298 K in 1 L LiNO<sub>3</sub> (0.1 M, Fisher), filtered, and dried overnight in air at a temperature of 353 K. The ammonium form of [Al]ZSM-5 (CBV3024E) was purchased from Zeolyst International and used as received.

[B]ZSM-5 was synthesized using hydroxide and fluoride methods. For the hydroxide synthesis, the gel was made by incorporating the materials at a molar ratio of  $x\text{B}(\text{OH})_3:100\text{SiO}_2:15\text{NaOH}:13\text{TPABr}:4400\text{H}_2\text{O}$ . Two zeolites were synthesized with  $x$  equal to 5 (OH-1) and 6.65 (OH-2). In a 100 mL gel synthesis (OH-2), boric acid (0.52 g, Sigma Aldrich), sodium hydroxide (0.76 g, Fisher), and tetrapropylammonium bromide (4.37 g, Sigma Aldrich) were added to deionized water

(100 g) while stirring constantly. Once completely dissolved, silicon dioxide (7.58 g, Cabosil M5) was slowly added to the solution. When all of the silicon dioxide was incorporated, the gel was stirred for 15 min. The resulting gel was then placed into the Teflon liner of a Parr 4744 autoclave and heated statically at a temperature of 423 K for 3 days. The zeolite particles were filtered and washed with deionized water until the filtrate reached neutral pH. After drying overnight at a temperature of 353 K, the zeolite was calcined in air using the following temperature program: a ramp from room temperature to 393 K in 1 h, a hold at 393 K for 2 h, a ramp from 393 K to 823 K in 3 h, and a final hold at 823 K for 5 h. Following calcination, an ion exchange was carried out overnight at a temperature of 298 K in 0.05 M  $\text{NH}_4\text{NO}_3$  (Sigma Aldrich). The amount of ammonium nitrate used was five times that of the boric acid added to the gel on a molar basis (approximately 6.5 g  $\text{NH}_4\text{NO}_3$  per 1 g  $\text{B}(\text{OH})_3$  in the gel). The zeolite was then filtered and rinsed three times in deionized water and dried overnight at a temperature of 353 K.

For the fluoride synthesis, the synthesis gel was prepared by forming a gel with composition of  $x\text{B}(\text{OH})_3:10\text{SiO}_2:9\text{KF}:1.25\text{TPABr}:330\text{H}_2\text{O}$  [127]. Two zeolites were synthesized with  $x$  equal to 0.5 (F-1) and 6 (F-2). In a 40 mL gel synthesis (F-2), boric acid (2.50 g, Sigma Aldrich), potassium fluoride (3.52 g, Alfa Aesar), and tetrapropylammonium bromide (2.24 g, Sigma Aldrich) were added to deionized water (40 g) under constant mixing. Once the solids were completely dissolved, silicon dioxide (4.04 g, Cabosil M5) was slowly added to the solution. The synthesis gel was then added to the Teflon liner of a Parr 4744 autoclave, and heated statically at a temperature of 443 K for 4 days. The crystallization product was separated, calcined

and ion-exchanged as indicated above, with the exception of ammonium acetate being used instead of  $\text{NH}_4\text{NO}_3$  as the ammonium source.

Two siliceous ZSM-5 samples were also synthesized. Silicalite-1 was synthesized utilizing the hydroxide method above without adding any boric acid to the gel. In addition, a hydroxide-synthesized [B]ZSM-5 zeolite ( $x = 6.65$ , OH-1) was deboronated by mixing at a temperature of 353 K for 3 h in 0.01  $\text{HNO}_3$  (Fisher, 0.1 L per 100 mg of zeolite). The zeolite was filtered, rinsed with deionized water three times, rinsed with 0.4 M  $\text{K}_2\text{CO}_3$  (0.25 L, Alfa Aesar), rinsed two times with deionized water, and dried overnight at a temperature of 353 K.

[B]Beta was synthesized by forming a gel with the following composition:  $5\text{B}(\text{OH})_3:73\text{SiO}_2:20\text{TEAOH}:1000\text{H}_2\text{O}$ . Boric acid (Sigma Aldrich) and tetraethylammonium hydroxide (35% w/w aqueous solution, Alfa Aesar) were added to deionized water while stirring constantly. Once the boric acid was completely dissolved, silicon dioxide (Cabosil M5) was slowly added to the solution. When all of the silicon dioxide was incorporated, the gel was stirred for 15 min. [B]Beta seed crystals (2% w/w of  $\text{SiO}_2$  in gel) were added to the gel and stirred for 5 min. The resulting gel was then placed into the Teflon liner of a Parr 4744 autoclave and heated statically at a temperature of 423 K for 14 days. Following crystallization, the synthesis proceeded via the same method as [B]ZSM-5, except ammonium acetate was for the ion exchange.

*Molybdenum Impregnation:* Supports were impregnated with molybdenum using the incipient wetness technique. The desired mass of ammonium heptamolybdate (Fisher) was weighed to yield a metal loading of 2-25% (w/w) Mo/support. A molybdenum loading of 5.8% was used in the majority of tests.

Ammonium heptamolybdate (AHM) was dissolved in the least amount of water possible at a temperature of 298 K. Once AHM was completely dissolved, the support was added to this solution and the mixture was heated at a temperature of 343 K (stirring constantly) until all water had evaporated. The solubility of AHM in water is sensitive to low pH and if the mixture turned green, indicating precipitation of AHM, ammonium acetate (Fisher) was added as a buffer until the mixture returned to a white color. Once dry, the sample was calcined in air using the following temperature profile: a ramp from 298 K to 393 K over 1 hr, a 2 hr hold at 393 K, a ramp from 393 K to 823 K over 3 hrs, and a final hold at 823 K for 5 hrs.

*Carburization:* Bulk  $\beta$ -Mo<sub>2</sub>C was synthesized by carburizing MoO<sub>3</sub> (Alfa Aesar) in 20% CH<sub>4</sub>/H<sub>2</sub> (20 mL/min total flow) with the following temperature program: a ramp from 298 K to 723 K at a rate of 5 K/min, a 10 min hold at 723 K, a ramp from 723 K to 923 K at a rate of 1 K/min, and a final hold at 923 K for 4 hrs. Carburization was performed within the experimental setup described previously [98] and conditions were similar to those reported from other groups [116]. This procedure was also used to carburize Mo-impregnated samples.

#### **4.2.2 Characterization**

Sample chemical compositions were determined by inductively coupled plasma mass spectrometry (ICP-MS) at Galbraith Laboratories, Inc (Knoxville, TN). Surface area and microporous volumes (calculated using the t-plot method) were determined from N<sub>2</sub> adsorption isotherms measured using a Micromeritics ASAP 2020 instrument. The samples were pretreated at a temperature of 423 K and a pressure of 0.5 torr overnight to remove any adsorbed species. X-ray powder diffraction patterns (PXRD) were measured using a Bruker D8 X-ray diffractometer with a CuK $\alpha$  source

( $\lambda = 1.542\text{\AA}$ ). Diffraction patterns were obtained using a step size of  $0.02^\circ 2\theta$  with 1 s counting time at each step and were measured between  $5^\circ$  and  $50^\circ 2\theta$ . SEM images were taken with a JSM-7400F scanning electron microscope with an accelerating voltage of 3.00 kV.

### 4.2.3 Catalytic Tests

The reactor system used for catalyst performance testing was the same as described in a previous report [98], except that a syringe pump (Teledyne Isco 260D) was used instead of a HPLC pump to feed the reactants into the system. An online gas chromatograph (GC) (Agilent 7890B) equipped with a flame ionization detector (FID) was used to analyze reactor effluent. Separation of chemical species within the reactor effluent was performed in the GC with an Alumina column (Agilent, 50 m x 530  $\mu\text{m}$  ID). Helium was used as the carrier gas and nitrogen was used as the makeup gas. The following temperature program was used for product detection: a 5 minute hold at 373 K, a ramp to 473 K at a rate of 20 K/min, and a final hold at 473 K. The duration of the final hold depended on the reactor feed: 15 min for *n*-pentane, 20 min for *n*-hexane, and 25 min for *n*-heptane.

The catalyst powder was pressed (5000 psi, 13 mm dye), gently crushed and sieved to particle sizes between 250 and 425  $\mu\text{m}$  (40 – 60 mesh). Each experiment was performed using 100-200 mg of the sieved catalyst. Prior to each experiment, the catalyst was carburized *in situ* as detailed in Section 4.2.1. At the end of the carburization, reactor temperature was lowered to the experiment temperature over 2 h.

A variety of reaction conditions were investigated: pressure was investigated from 10 bar to 60 bar and reaction temperature was studied in the range of 673 – 798

K. Most experiments were performed in the supercritical regime of the reactants ( $T_c = 470$  K and  $P_c = 34$  bar for *n*-pentane,  $T_c = 508$  K and  $P_c = 30$  bar for *n*-hexane, and  $T_c = 540$  K and  $P_c = 27$  bar for *n*-heptane) [93]. Weight hourly space velocity (WHSV, defined as grams of pentane fed per gram of catalyst per hour) ranged from 94 – 376  $\text{g}_{\text{C5}}\text{g}_{\text{cat}}^{-1}\text{h}^{-1}$  for *n*-pentane, 98 - 393  $\text{g}_{\text{C6}}\text{g}_{\text{cat}}^{-1}\text{h}^{-1}$  for *n*-hexane, and 102 - 408  $\text{g}_{\text{C7}}\text{g}_{\text{cat}}^{-1}\text{h}^{-1}$  for *n*-heptane. WHSV was controlled by changing the reactant liquid flow rates in the range of 0.5 - 2.0 mL/min. Conversion of reactant was defined as 100% minus the percentage of unreacted feed (all isomers included) in the product stream. Product carbon selectivity was defined as the fraction of carbon in each product as compared to the total amount of carbon in the effluent that was not reactant (See Equation 3.1).

### 4.3 Results

#### 4.3.1 Zeolite Characterization

The XRD patterns (Appendix B) of the zeolite samples showed that the materials were highly crystalline and did not reveal the presence of any amorphous material or other crystalline impurities. Micropore volumes and Si/B ratios of the zeolite frameworks are shown in Table 4.1. The ZSM-5 samples synthesized using the hydroxide anion had micropore volumes of 0.13 – 0.14  $\text{cm}^3/\text{g}$ , typical of MFI-type samples. By using fluoride as the anion during synthesis, more boron was incorporated into the framework but micropore volume decreased. This decrease in micropore volume could be caused by twinning within the crystal [128], since the XRD patterns reveal a very crystalline sample. While the XRD pattern of the deboronated [B]ZSM-5 (OH-1) exhibited no change in the crystal structure, a decrease in micropore volume from 0.14  $\text{cm}^3/\text{g}$  to 0.11  $\text{cm}^3/\text{g}$  was observed. SEM images show [B]ZSM-5 (OH-1)

samples have a crystal size ranging from 2 – 4  $\mu\text{m}$  (Figure 4.11) and [B]Beta (Appendix B) has a crystal size of 0.5  $\mu\text{m}$ . The typical catalyst used throughout this investigation was H-[B]ZSM-5 (OH-1) loaded with 5.8% (w/w) Mo, resulting in Mo/B of approximately 3.

Table 4.1: Si/B ratios and micropore volumes of zeolite supports; samples with F-1/F-2 and OH-1/OH-2 indicate synthesized in fluoride and hydroxide media respectively

Sample	Si/B	Micropore Volume ( $\text{cm}^3/\text{g}$ )
[B]ZSM-5 (F-1)	21	0.111
[B]ZSM-5 (F-2)	63	0.100
[B]ZSM-5 (OH-1)	73	0.141
[B]ZSM-5 (OH-2)	82	0.130
Deboronated	>1000	0.107
Silicalite-1	>1000	0.132
[B]Beta	18	0.200

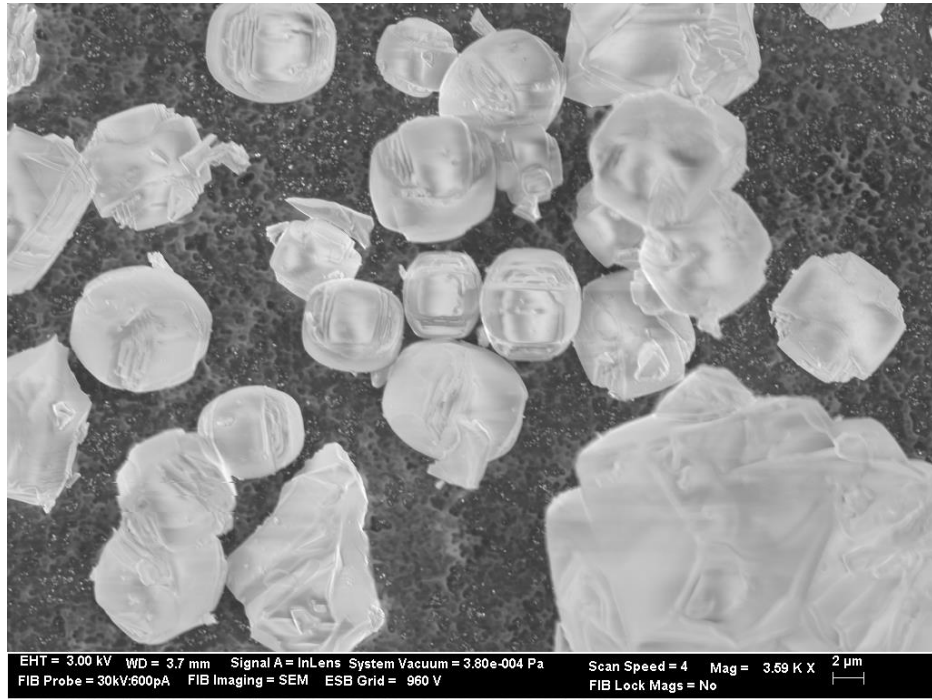


Figure 4.1: SEM image of [B]ZSM-5 (OH-1) (*top*) and [B]ZSM-5 (F-1) (*bottom*)

### 4.3.2 Catalyst Screening

Several materials were tested as supports for molybdenum and compared to bulk molybdenum carbide for catalytic dehydrogenation of *n*-pentane. Figure 4.2 shows the rate of *n*-pentane consumption on various molybdenum carbide catalysts and the carbon selectivity to pentenes (sum of all isomers). Molybdenum supported on zirconia and magnesia exhibited similar conversion and carbon selectivity to bulk molybdenum carbide.  $\gamma$ -Alumina had twice the consumption rate as bulk molybdenum carbide and 80-90% carbon selectivity to pentenes.  $\gamma$ -Alumina had twice the consumption rate as bulk molybdenum carbide and 80-90% carbon selectivity to pentenes. Molybdenum supported on H-[B]ZSM-5 exhibited the same high selectivity to the dehydrogenation product as  $\text{Mo}/\gamma\text{-Al}_2\text{O}_3$ , but consumption rates were over two times higher (see Figure 4.2).

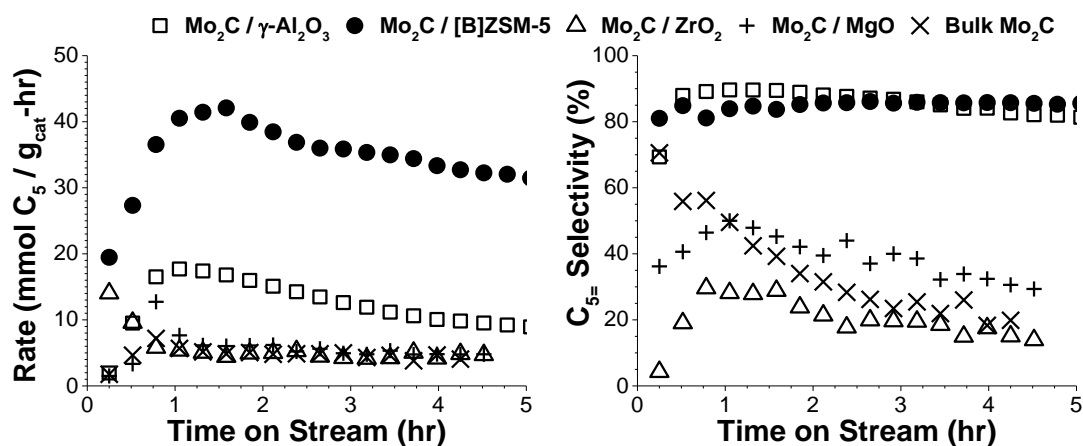


Figure 4.2: Consumption of *n*-pentane (*left*) and carbon selectivity to pentenes (*right*) on various molybdenum carbide catalysts (5.8% Mo/support). Reaction conditions:  $T = 723$  K,  $P = 40$  bar, and  $\text{WHSV} = 188 \text{ g}_{\text{C}_5}\text{g}_{\text{cat}}^{-1}\text{h}^{-1}$

Table 4.2 lists rates and carbon selectivity for different metal loadings of  $\text{Mo}/\gamma\text{-Al}_2\text{O}_3$  and  $\text{Mo}/\text{H-[B]ZSM-5}$ . Conversion and carbon selectivity to the

dehydrogenation product increase with increasing molybdenum loading until the loading reaches 4% w/w, at which point metal loading has little effect on catalyst reaction rates.

Table 4.2: Consumption of *n*-pentane and carbon selectivity to pentenes on different metal loadings of Mo/ $\gamma$ -Al<sub>2</sub>O<sub>3</sub> and Mo/H-[B]ZSM-5. Reaction conditions:  $T = 723$  K,  $P = 40$  bar, and  $WHSV = 188$  g<sub>C5</sub>g<sub>cat</sub><sup>-1</sup>h<sup>-1</sup>

Mo (w/w)%	$\gamma$ -Al <sub>2</sub> O <sub>3</sub>		[B]ZSM-5 (OH-1)	
	Rate	C <sub>5=</sub> Sel	Rate	C <sub>5=</sub> Sel
0	4.2	5.6	4.4	6.0
2	-	-	12.6	71.6
4	13.9	57.5	25.8	83.9
6	20.4	84.9	40.5	84.7
8	25.4	80.9	27.4	84.8
10	-	-	19.5	78.1
12	27.9	82.1	22.0	84.1
25	15.7	75.7	-	-

Figure 4.3 shows how boron concentration within the zeolite affects the consumption of pentane and production of pentenes. Reaction rates were highest when the hydroxide synthesis method was used to prepare the zeolite support (Si/B = 73 and 82). By incorporating more boron into the framework using the fluoride synthesis method (Si/B = 21 and 63), the overall reaction rate decreased, but selectivity remained high. The same result was observed when no boron was incorporated in the framework or the zeolite (OH-1) was deboronated by acid leaching. Reaction rates decreased by a factor of three, but selectivity to pentenes remained as high as the most active samples.

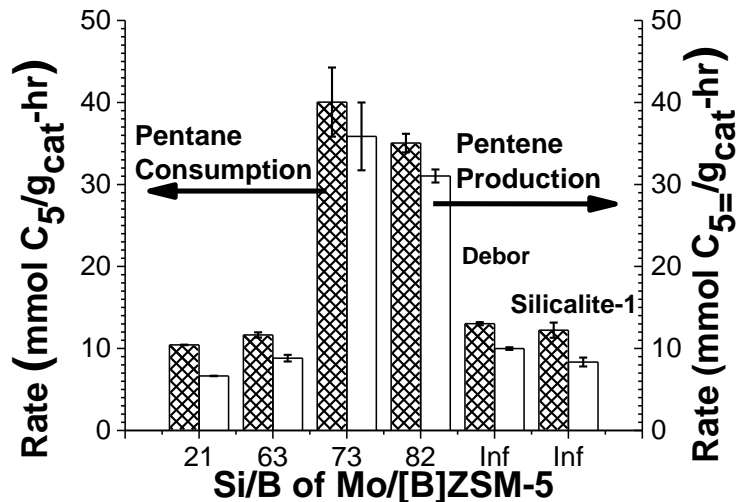


Figure 4.3: Consumption of *n*-pentane (*checkered*) and production of pentenes (*white*) on Mo/H-[B]ZSM-5 with different Si/B ratios. Reaction conditions:  $T = 673 - 798 \text{ K}$ ,  $P = 40 \text{ bar}$ , and  $\text{WHSV} = 188 \text{ g}_{\text{C}_5}\text{g}_{\text{cat}}^{-1}\text{h}^{-1}$

### 4.3.3 Catalytic Dehydrogenation of *n*-Pentane

The catalytic properties of  $\gamma\text{-Al}_2\text{O}_3$  and H-[B]ZSM-5 supports were compared to that of quartz wool and Mo/H-[B]ZSM-5 (Figure 4.4). Quartz wool,  $\gamma\text{-Al}_2\text{O}_3$ , and H-[B]ZSM-5 all exhibited similar reactivity with very low selectivity to pentenes, whereas Mo/H-[B]ZSM-5 produced higher rates of pentane consumption and pentene production. This difference in catalytic properties indicates that molybdenum is involved in the formation of the catalytic sites for pentane dehydrogenation. Note that maximum pentene production rates occurred at a temperature of 773 K, after which pentene production decreased even though pentane consumption rates continued to increase.

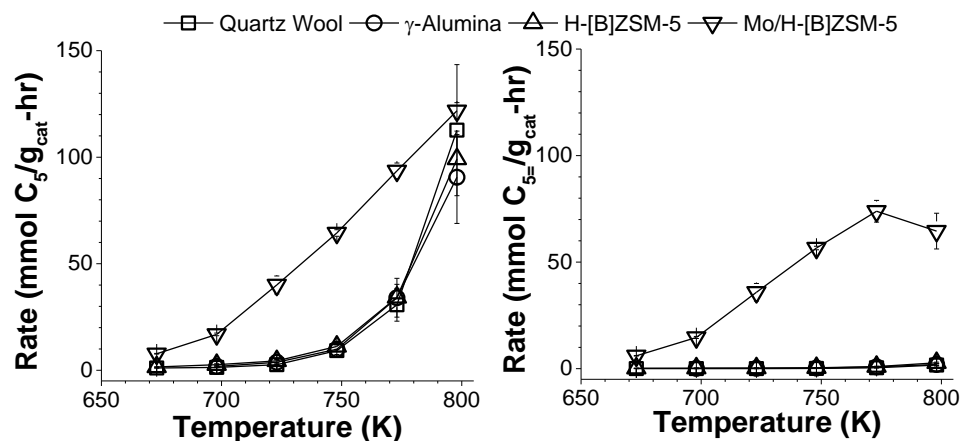


Figure 4.4: Consumption of *n*-pentane (*left*) and production of pentenes (*right*) on unloaded supports and Mo/H-[B]ZSM-5. Reaction conditions:  $T = 673 - 798$  K,  $P = 40$  bar, and  $WHSV = 188 \text{ g}_{C_5}g_{cat}^{-1}h^{-1}$

Figure 4.5 shows the rates of *n*-pentane consumption and pentene production as a function of pressure and weight hourly space velocity. Increasing pressure led to an increase in the rate of pentane consumption, while selectivity to pentenes remained unchanged. Increasing WHSV resulted in only small variations in the rate of pentane consumption, but led to a decrease in rate of pentene production. At higher WHSV, selectivity to pentenes decreased, while an increase in selectivity to all products lighter than pentane, not including the dehydrogenation product, was observed.

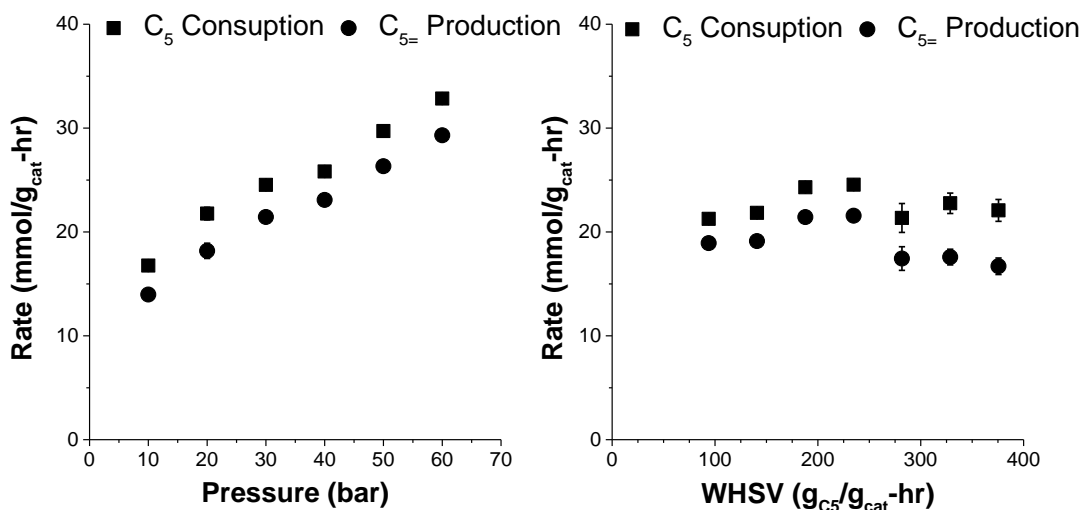


Figure 4.5: Consumption of *n*-pentane and production of pentenes on Mo/H-[B]ZSM-5 during varying pressures (*left*) and space velocities (*right*). Reaction conditions:  $T = 723$  K,  $P = 10 - 60$  bar,  $\text{WHSV} = 188 \text{ g}_{\text{C}_5}\text{g}_{\text{cat}}^{-1}\text{h}^{-1}$  and  $T = 723$  K,  $P = 40$  bar,  $\text{WHSV} = 94 - 376 \text{ g}_{\text{C}_5}\text{g}_{\text{cat}}^{-1}\text{h}^{-1}$ , respectively.

#### 4.3.4 Catalytic Dehydrogenation of *n*-Hexane and *n*-Heptane

Table 4.3 shows rates of *n*-pentane, *n*-hexane and *n*-heptane consumption carbon selectivity to the primary dehydrogenation products and to the sum of light olefins, including the primary dehydrogenation products, on Mo/ $\gamma$ -Al<sub>2</sub>O<sub>3</sub>, Mo/H-[B]Beta, and Mo/H-[B]ZSM-5. Selectivity to the dehydrogenation product for *n*-hexane conversion on Mo/H-[B]ZSM-5 was less than that of *n*-pentane conversion, but when the total olefinic product (all lighter olefins including hexene) was considered, the carbon selectivity was comparable to that of *n*-pentane. Similar trends were observed for *n*-heptane.  $\gamma$ -Al<sub>2</sub>O<sub>3</sub>, in contrast to H-[B]ZSM-5 as a support for molybdenum, was less active (80-95%) than H-[B]ZSM-5 and had a lower selectivity to the dehydrogenation (75-95%) and olefinic (75-90%) products. H-[B]Beta was the

least active (approximately 50% less than H-[B]ZSM-5) and selective (60-75% less than H-[B]ZSM-5) of the three supports. Like Mo/  $\gamma$ -Al<sub>2</sub>O<sub>3</sub>, Mo/H-[B]ZSM-5 was able to dehydrogenate *n*-alkanes, but lacked secondary sites found in  $\gamma$ -Al<sub>2</sub>O<sub>3</sub>, which consume olefins, preserving the primary dehydrogenation product.

Table 4.3: Consumption of *n*-pentane, *n*-hexane, and *n*-heptane and selectivity to primary dehydrogenation product and olefins lighter than the primary dehydrogenation products on Mo/H-[B]ZSM-5, Mo/ $\gamma$ -Al<sub>2</sub>O<sub>3</sub>, and Mo/[B]Beta. *T* = 723 K, *P* = 40 bar, WHSV = 188 g<sub>C5</sub>/g<sub>cat</sub>-hr, 196 g<sub>C6</sub>/g<sub>cat</sub>-hr and 205 g<sub>C7</sub>/g<sub>cat</sub>-hr

		[B]ZSM-5	$\gamma$ -Al <sub>2</sub> O <sub>3</sub>	[B]Beta
Rate (mmol/g <sub>cat</sub> -hr)	C <sub>5</sub>	40.0	20.4	12.5
	C <sub>6</sub>	12.8	10.1	7.0
	C <sub>7</sub>	12.3	12.1	6.3
Primary Dehydrogenation Product Selectivity (%)	C <sub>5</sub>	89.5	84.9	72.8
	C <sub>6</sub>	71.1	54.9	52.3
	C <sub>7</sub>	66.4	64.9	41.0
Olefinic Product Selectivity (%)	C <sub>5</sub>	91.2	94.6	90.8
	C <sub>6</sub>	85.4	77.1	75.3
	C <sub>7</sub>	89.4	84.9	71.6

#### 4.4 Discussion

Bulk and supported metal carbides have been shown to catalyze dehydrogenation of hydrocarbons [113,129]. Additionally, molybdenum carbide supported on H-[Al]ZSM-5 has been used to form aromatics from alkanes [130], where molybdenum carbide sites promote dehydrogenation and acid sites in the zeolite promote oligomerization and hydride transfer reactions. In this work, molybdenum

supported on low acidity H-[B]ZSM-5 was used as a means to isolate dehydrogenation and suppressed secondary reactions that lead to aromatics.

The active form of the catalyst is believed to be  $\text{MoC}_x$  species, as applying the conditions mentioned in section 4.2.1 to bulk molybdenum resulted in molybdenum carbide (see XRD in Appendix B). All supported molybdenum catalysts exhibited an induction period with peak conversion occurring approximately at 1-1.5 h time on stream (Figure 4.2). The induction period also occurred and the same peak conversion reached whether Mo/H-[B]ZSM-5 was carburized prior to the catalytic experiment (Section 4.2.1) or only calcined in air. This indicates that the active form of the catalyst, molybdenum carbide can be formed during the reaction using the feed alkanes as a carbon source. Several reports have shown that methane is not necessary to carburize molybdenum and that other hydrocarbons, such as ethane, acetylene, and toluene, can also carburize the Mo-oxide nanoparticles [131–133]. Molybdenum was necessary for catalytic dehydrogenation as the control experiments (blank supports) produced nearly no pentenes (Figure 4.4), which is in agreement with previous reports that showed chromia was needed to increase dehydrogenation rates [134,135]. At temperatures above 798 K, the rate of gas-phase reactions becomes a significant contribution to the overall observed reaction rates and selectivity. Therefore, the catalysts are not effective in controlling neither rates nor selectivity at temperature above 798 K.

The most active [B]ZSM-5 supports were those synthesized using the hydroxide synthesis route. Using directly synthesized siliceous ZSM-5 (silicalite-1) and deboronated [B]ZSM-5 (OH-1) as supports for molybdenum led to a decrease in reaction rates, therefore, the boron plays a role in the formation of the active catalyst

sites. Even though no change was observed in the XRD pattern or SEM of the deboronated [B]ZSM-5 (OH-1), there was a loss in micropore volume, which could be attributed to some collapse of the framework or extra-framework boron that was not completely removed from the pores. On the other hand, incorporating more boron into the zeolite framework via the fluoride synthesis also led to lower activity. This may be caused by an optimal framework concentration for boron, but may also be attributed to the lower micropore volume of those supports. In a report by Gao et al., density functional theory (DFT) calculations revealed that molybdenum anchored on two aluminum sites was the lowest energy configuration [136]. X-ray absorption, Raman, and infrared spectroscopy experiments have shown the anchoring of molybdenum species on acid sites within the pores of H-[Al]ZSM-5 [16,129]. Just as framework aluminum acts as an anchor for molybdenum clusters within the zeolite pores, framework boron may also act as an anchor for Mo clusters to form. Better dispersion of molybdenum within the zeolite pores could lead to the formation of smaller MoC<sub>x</sub> particles and consequently potentially forming more reaction sites.

Substitution of aluminum with boron in the zeolite framework led to a change in product selectivity. Conversion of *n*-pentane on Mo/H-[B]ZSM-5 produced pentenes as the major product (>90% selectivity). When molybdenum was supported on acidic H-[Al]ZSM-5, the product distribution closely resembled that of Mo-free H-[Al]ZSM-5, where propane and butane are the major products, followed by species heavier than pentane [98]. H-[B]ZSM-5 does not contain strong Brønsted acid sites, such as those found in H-[Al]ZSM-5, that consume olefins via secondary bimolecular reactions (hydride transfer and oligomerization). By replacing aluminum with boron in

ZSM-5, these secondary reactions were suppressed, preserving the primary dehydrogenation product.

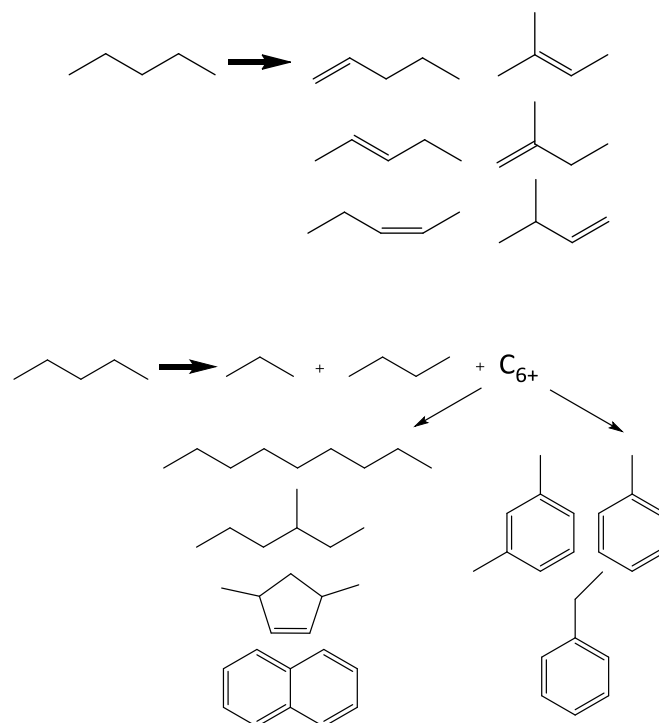


Figure 4.6: Example product distribution of *n*-pentane conversion on Mo/H-[B]ZSM-5 (*top*) and Mo/H-[Al]ZSM-5 (*bottom*). Reaction conditions:  $T = 723 \text{ K}$ ,  $P = 40 \text{ bar}$ , and  $\text{WHSV} = 188 \text{ g}_{\text{C}_5\text{g}_{\text{cat}}^{-1}\text{h}^{-1}}$

A decrease in consumption rate and selectivity to the primary dehydrogenation product (Table 4.3) was observed for *n*-hexane and *n*-heptane with respect to *n*-pentane. For all three species, selectivity to the primary dehydrogenation product exhibited a parabolic shape. Selectivity increased as reaction temperature increased, reaching a maximum around a temperature of 723 K and then decreased with further

increases in temperature (Fig 4.7). When all olefins lighter than the reactant are considered, all three *n*-alkanes yielded nearly the same selectivity to the total olefinic product. There was a much higher amount of olefins lighter than the feed compared to paraffins lighter than the feed. This product distribution suggests that olefins lighter than the feed are produced from cracking of the primary dehydrogenation product (or its isomers) in addition to direct monomolecular cracking of the feed, leading to a further increase in reaction endothermicity.

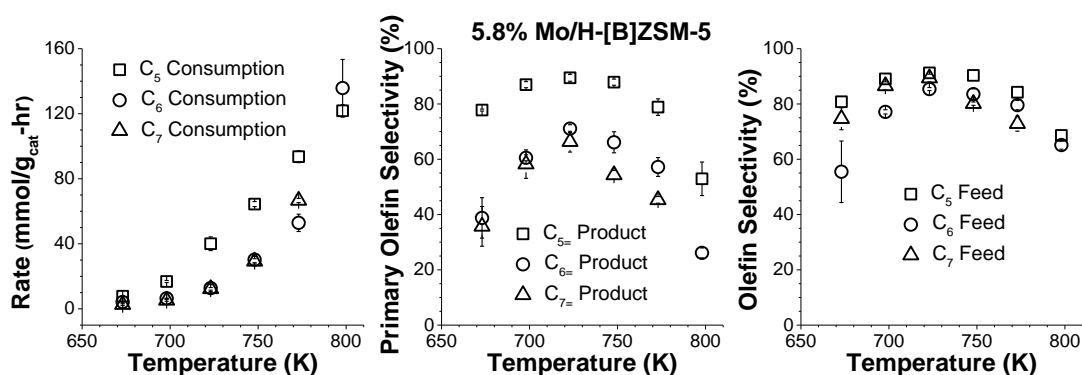


Figure 4.7: Consumption of *n*-pentane, *n*-hexane, and *n*-heptane and selectivity to primary dehydrogenation product and olefins lighter than the primary dehydrogenation products on Mo/H-[B]ZSM-5, Mo/ $\gamma$ -Al<sub>2</sub>O<sub>3</sub>, and Mo/[B]Beta.  $T = 673 - 798$  K,  $P = 40$  bar, WHSV = 188 gC<sub>5</sub>/g<sub>cat</sub>-hr, 196 gC<sub>6</sub>/g<sub>cat</sub>-hr and 205 gC<sub>7</sub>/g<sub>cat</sub>-hr

Although conversion of hexane and heptane on Mo/H-[B]ZSM-5 led to lower rates than pentane conversion, the observed activation energy for all three hydrocarbons are approximately equal at lower temperatures (673 – 723 K) (Figure 4.8). For conversion of pentane, the activation energy decreased with increasing temperature from 133 kJ/mol, between 673 K and 723 K, to 64 kJ/mol, between 748 K

and 798 K. The decrease in activation energy by half suggests pore diffusion limitations. Calculation of the Weisz-Prater criterion, using diffusions extrapolated from a report by Jobic et al. [137], resulted in a value on the order of  $10^{-5}$ . The low magnitude of this value (much less than one), shows that pore diffusion is not the limiting factor, and suggests that a different reaction mechanism may have become the dominant reaction pathway, leading to the decrease in activation energy. Finally, while there was an increase in reaction endothermicity from using Mo/H-[B]ZSM-5, reaction rates were an order of magnitude lower than observed with H-[Al]ZSM-5, resulting in an overall decrease in process endothermicity.

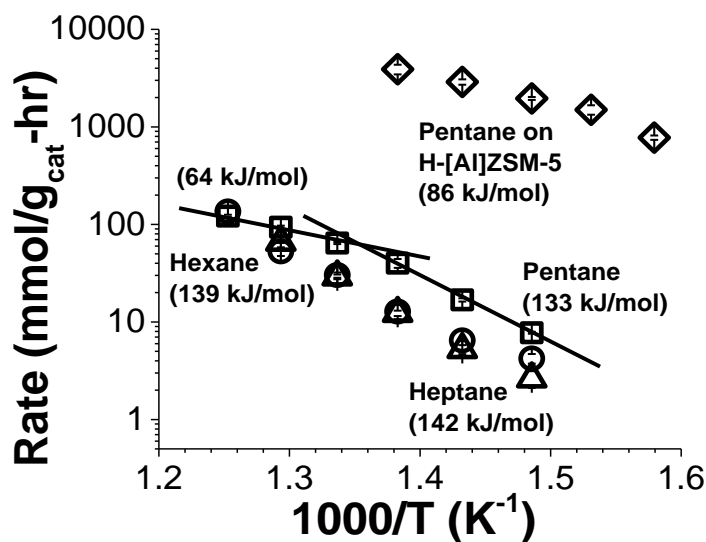


Figure 4.8: Rates of consumption of *n*-pentane (*square*), *n*-hexane (*circle*), and *n*-heptane (*triangle*) on Mo/H-[B]ZSM-5 and *n*-pentane on H-[Al]ZSM-5 (*diamond*) at various temperatures. Reaction conditions:  $T = 673 - 798$  K,  $P = 40$  bar, and  $WHSV = 188$   $g_{C5}/g_{cat}\text{-hr}$ ,  $196$   $g_{C6}/g_{cat}\text{-hr}$  and  $205$   $g_{C7}/g_{cat}\text{-hr}$  for Mo/H-[B]ZSM-5 and  $T = 633 - 723$  K,  $P = 40$  bar, and  $WHSV = 1120$   $g_{C5}/g_{cat}\text{-hr}$  for H-[Al]ZSM-5

Yeh et al. recently investigated *n*-hexane conversion on H-[Al]ZSM-5 and H(Zn)-[Al]ZSM-5 under high pressures [138]. At a temperature of 633 K and pressure of 137 bar, butanes and pentanes were the major products of hexane conversion on H-[Al]ZSM-5, with molar selectivity of 16% and 43%, respectively. When zinc was ion-exchanged on H-[Al]ZSM-5 at a loading of 1.3% (w/w), resulting in a Zn/Al less than 0.5, the consumption rate of hexane decreased from approximately 800 mmol/g<sub>cat</sub>-hr to 25 mmol/g<sub>cat</sub>-hr. Even though these experiments were performed at conditions different than those reported in this investigation, the reaction rates were of the same order. While pentanes remained the major product with selectivity of 31%, selectivity to butanes decreased to 5%, and a significant increase in selectivity to hydrogen (5% - 22%) and BTX (7% - 20%) was observed. This change in product selectivity led to an increase in the heat of reaction from 8 kJ/mol to 45 kJ/mol. Increasing zinc loading to 9.9% (w/w) led to a further decrease in hexane consumption rate to 8 mmol/g<sub>cat</sub>-hr, but product selectivity remained nearly constant. H(Zn)-[Al]ZSM-5 and Mo/H-[B]ZSM-5 alter the product selectivity to form higher energy species compared to those formed by using H-[Al]ZSM-5, but at the cost of an order of magnitude in consumption rates. Although reaction endothermicity is increased by the change in product selectivity, the loss in consumption rates leads to an overall decrease in process endothermicity.

#### 4.5 Conclusion

By utilizing weakly acidic H-[B]ZSM-5 material instead of H-[Al]ZSM-5 as a support for molybdenum species, it was found that secondary reactions that lead to molecular weight growth, were suppressed, preserving the primary dehydrogenation product and increasing reaction endothermicity. As the molecular weight of the feed increased, selectivity to the primary dehydrogenation product decreased, but total

olefinic product selectivity remained nearly constant. Cracking of the primary dehydrogenation product further increased the reaction endothermicity. While high-pressure dehydrogenation of alkanes on Mo/H-[B]ZSM-5 led to a higher reaction endothermicity ( $\sim 129 \text{ kJ/mol}_{\text{C}_5}$ ) compared to high-pressure conversion on H-[Al]ZSM-5 ( $\sim 43 \text{ kJ/mol}_{\text{C}_5}$ ), consumption rates were an order of magnitude less, resulting in an overall reduction in process endothermicity from  $168 \text{ kJ/g}_{\text{cat}}\text{-hr}$  on H-[Al]ZSM-5 to  $16 \text{ kJ/g}_{\text{cat}}\text{-hr}$  on Mo/H-[B]ZSM-5. Further improvement in reaction rates while maintaining a high selectivity to olefins is required to make Mo/[B]ZSM-5 a viable catalyst for endothermic cooling applications.

## Chapter 5

### METHANOL CONVERSION TO HYDROCARBONS ON FERRISILICATE [Fe]BETA

This chapter reports an investigation on the conversion of dimethyl ether (DME), which is the condensation product of methanol, on microporous ferrisilicate, [Fe]Beta. In the standard methanol-to-olefin (MTO) reaction with H-SAPO-34 or H-[Al]ZSM-5, ethylene and propylene or propylene and butenes are the major olefins produced, respectively. The intent was to develop a catalyst to produce olefins larger than those formed with MTO using ZSM-5 or SAPO-34 and then, in a subsequent step, couple those olefins to produce species larger than C<sub>12</sub>. To preserve the large olefins, it was hypothesized that the acid strength of the zeolite would have to be reduced to suppress hydride transfer reactions that lead to aromatic formation, but still be strong enough to catalyze methylation of double bonds. This was accomplished by using ferrisilicate instead of aluminosilicate zeolites. Nickel was subsequently added to promote oligomerization of the olefins formed from conversion of DME.

#### 5.1 Introduction

The gap generated by fluctuations in petroleum supply and derivative demand offers an opportunity for utilizing alternative carbon sources for fuels and chemicals. Gasification of coal, methane, and biomass can provide an alternative supply of these fuels and chemicals. Methanol, an intermediate formed from synthesis gas produced via gasification of multiple feedstocks, can be transformed into hydrocarbons using homogeneous or heterogeneous catalysts [139–142].

There are three classes of methanol conversions to hydrocarbons: methanol-to-olefins (MTO), methanol-to-aromatics (MTA), and methanol-to-gasoline (MTG). Into which class methanol conversion falls under is influenced by catalyst used and process condition [26]. Both MTG and MTO have been commercialized [25,143,144]. Industrially, methanol is first dehydrated to dimethyl ether (DME) and after the water is removed, DME is then fed to the desired reactor/catalyst system [27]. H-[Al]ZSM-5, a medium-pore zeolite, is used to catalyze the MTG process, with propylene and butene being produced as major byproducts. H-SAPO-34, a silicon aluminophosphate with chabazite structure and small-pores, is used to catalyze the MTO process [145,146].

Conversion of methanol occurs via a hydrocarbon pool mechanism with two different hydrocarbon pools having been identified: an alkene and an arene carbon pool (Figure 5.1) [27,147,148]. In the alkene cycle, olefins are successively alkylated (Figure 5.2), adding one addition methyl group in each step of the cycle. The alkene starts a chain and when that chain is large enough, it can crack producing two lighter alkenes, one that is the product and another that reenters the cycle. Alternatively, the larger alkenes can cyclize and aromatize entering the aromatic cycle. In the aromatic cycle, an arene is successively alkylated. Methyl groups on the arene combine and are eventually released as an olefin product.

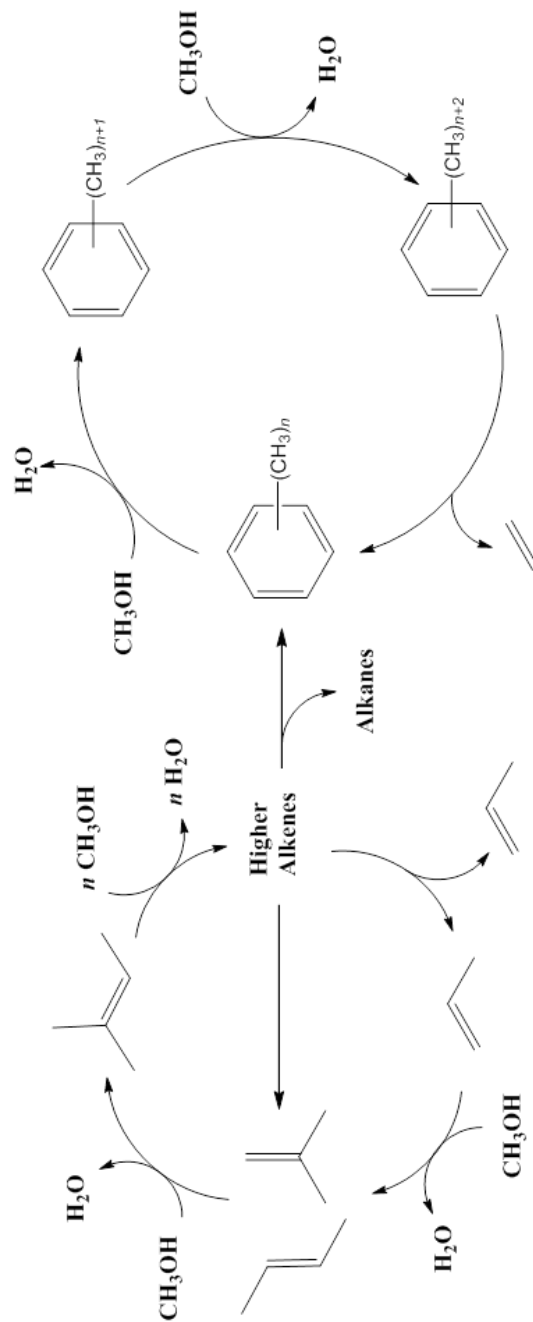


Figure 5.1: Hydrocarbon pool mechanism for methanol conversion to hydrocarbons showing an alkene cycle (*left*) and arene cycle (*right*). Recreated from review by Olsbye et al. [27]

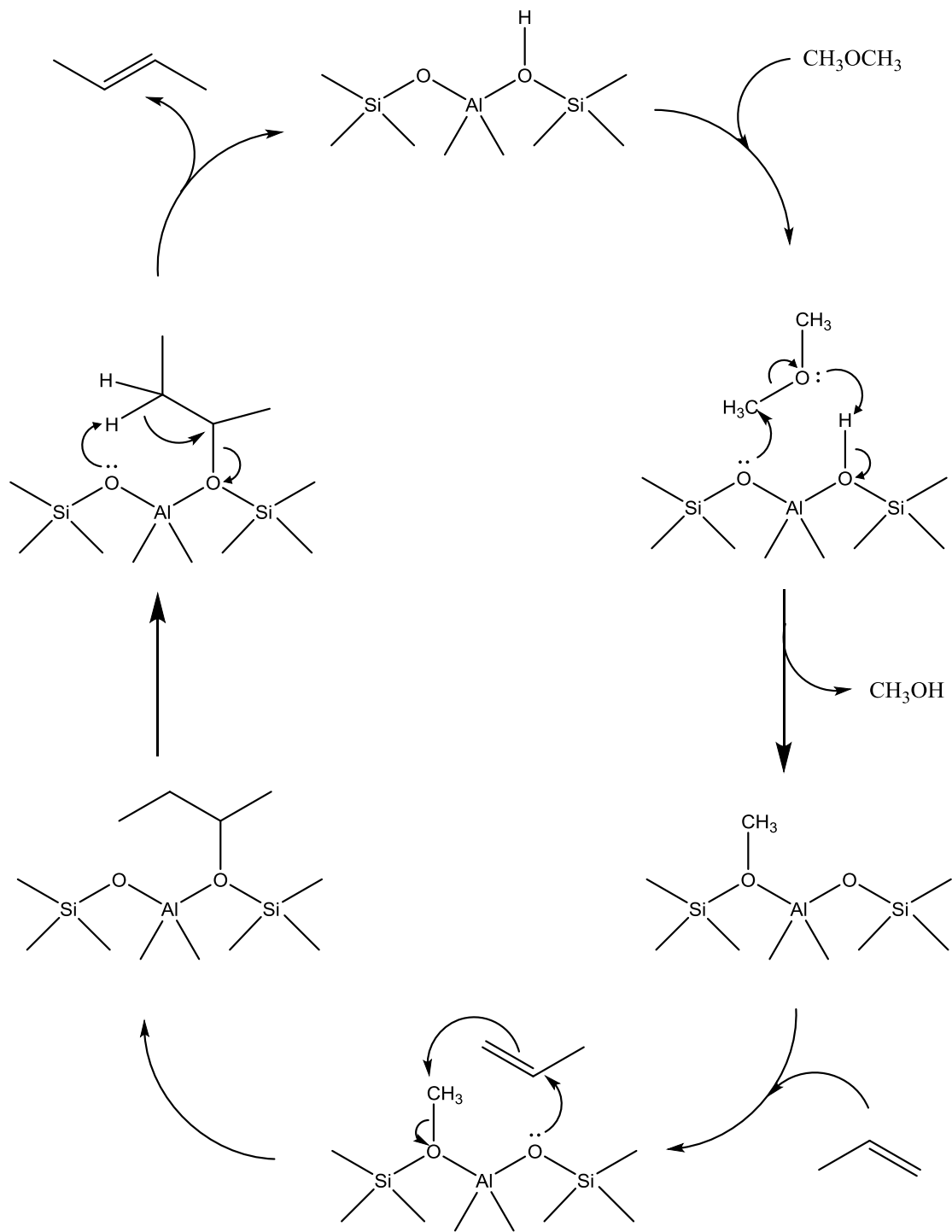


Figure 5.2: Example catalytic cycle of propylene methylation by dimethyl ether on a zeolite acid site

The size and shape of the zeolite pore structure influences which hydrocarbon pool forms and therefore the distribution of products that is produced [149–151]. An example is comparing the MTG catalyst, ZSM-5, with ZSM-22, which has a similar pore size, but different structure. Both zeolites have 10 member ring (MR) straight channels, but only ZSM-5 has 10 MR sinusoidal channels that run perpendicular and intersect the straight channels. Unidirectional 10 MR ZSM-22 does not have the space to form the bulky aromatics in the arene cycle and only the alkene cycle contributes to the product distribution [152]. In ZSM-5, the channel intersections are large enough to allow the formation of aromatic species and therefore, both cycles contribute to the product distribution.

A third example is methanol conversion on H-[Al]Beta. Ahn et al. have shown that methanol conversion on H-[Al]Beta produces isobutane and triptane as the major products [153]. Hazari et al. showed that methanol conversion on Beta occurs via a modified alkene cycle (Figure 5.3) [154]. Alkenes are successively methylated until reaching triptene. Triptene then either undergoes hydride transfer to form triptane or is methylated again. The formed C<sub>8</sub> alkene isomerizes and cracks to form two isobutenes, which also undergo hydride transfer to form isobutane. Hexamethylbenzene forms in parallel to complete the hydrogen/carbon balance, but diffuses quickly out of the pores of Beta, which suppresses the aromatic cycle.

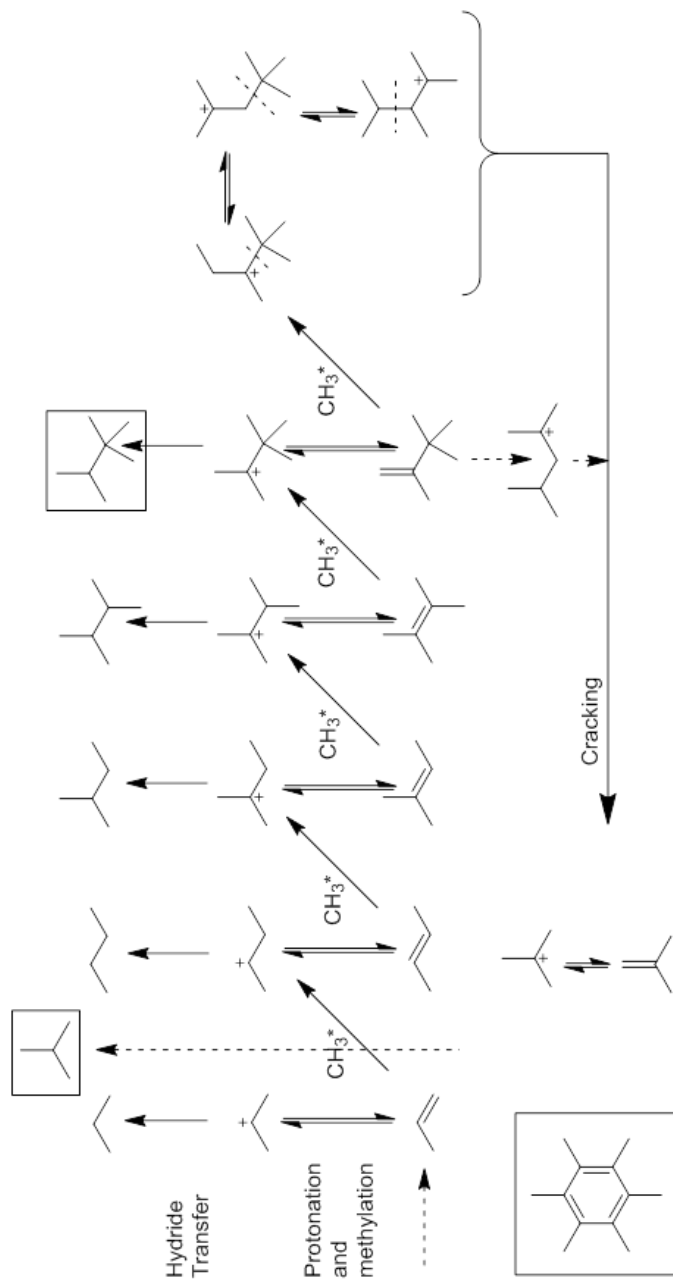


Figure 5.3: Reaction network for methanol conversion on H-[Al]Beta. Recreated from publication by Hazari et al. [154]

Aside from zeolite structure altering product selectivity of methanol conversion, acid strength also contributes to controlling which products are formed. Jin et al. investigated the influence of heteroatom substitution in ZSM-5 on methanol conversion, where iron and gallium substituted ZSM-5 were compared to H-[Al]ZSM-5 [155]. H-[Al]ZSM-5 was most the reactive and selective to aromatic production, whereas H-[Fe]ZSM-5 was the least reactive and selective to aromatic production, but the most selective to alkene production. Similarly, Taniguchi et al. showed that nanocrystalline H-[Fe]ZSM-5 converted methanol to olefins with greater than 90% selectivity [156]. These reports show that the acidity of H-[Fe]ZSM-5 is strong enough to catalyze carbon-carbon coupling reactions in methanol conversion, but not strong enough to catalyze hydride transfer reactions that lead to the formation of aromatic species.

Oligomerization (defined as the formation of oligomers with a geometric weight distribution) of light olefins to form long-chain  $\alpha$ -olefins (LAO) is important to surfactants, polymers, and lubricants production [al-jallah] [157,158]. Industrially, ethylene oligomerization is performed homogeneously with transition metal based catalyst [158]. Ziegler-type catalysts, which are triethyl aluminum or derivatives of, is utilized most often, but nickel, titanium, or zirconium have also been utilized or patented [159–163]. A key disadvantage of using a homogeneous catalyst is the required addition of a separation unit to remove the catalyst and solvent from the product. Preferably, a heterogeneous catalyst would be used to simplify separation. Many supported nickel catalysts have been shown to be active for ethylene dimerization or oligomerization, such as NiO/ZrO<sub>2</sub>, Ni/ $\gamma$ -Al<sub>2</sub>O<sub>3</sub>, and nickel-exchange zeolites and mesoporous silicas [164–167].

In this chapter we investigated the conversion of dimethyl ether on H-[Fe]Beta as an alternative methanol-to-olefins catalysts. It was found that conversion of DME on H-[Fe]Beta produced olefins with high selectivity (>90%) and isobutene was the major species produced. While conversion of DME on H-[Al]Beta produced paraffins and H-[Fe]Beta produced olefins with high selectivity, the product distributions based on carbon number and compound skeletal structure were similar and it appears that DME conversion occurs via a similar reaction network for both catalysts. Finally, a partial nickel ion exchange was performed to promote oligomerization of the olefins produced from MTO. However, the opposite effect was observed: nickel addition led to a decrease in heavier olefin selectivity and a large increase in methane formation from DME.

## 5.2 Experimental Section

### 5.2.1 Materials

Dimethyl ether (Praxair, 99.5% purity) was used as received. For calcination and gas chromatograph operation, the following gases were used: Air (Keen, Grade 0.1), Helium (Keen, Grade 5.0), Hydrogen (Keen, Grade 5.0), and Nitrogen (Keen, Grade 5.0).

The ammonium form of [Al]ZSM-5 (CBV8014) was purchased from Zeolyst International and used as received.

[Fe]Beta was synthesized using a modified method report by Raj et al. [168]. A synthesis gel was made by incorporating materials at a molar ratio of  $2.0\text{Fe(III)}_2(\text{SO}_4)_3$ :  $85.3\text{SiO}_2$ :  $3.3\text{NaOH}$ :  $1.8\text{KOH}$ :  $42.9\text{TEAOH}$ :  $1000\text{H}_2\text{O}$ . In a 45 mL gel synthesis, sodium hydroxide (0.25 g, Fisher) and potassium hydroxide (0.18 g,

Fisher) were dissolved in a 35% w/w solution of tetraethylammonium hydroxide and water (33.8 g, Alfa Aesar). While constantly stirring, silicon dioxide (9.6 g, Cab-o-sil M5) was slowly added to this first solution. A second solution was made by dissolving ferric sulfate (1.5 g, Sigma Aldrich) in deionized water (11.8 g). Upon complete incorporation of the silicon dioxide, the gel was stirred for 15 min. After 15 min of stirring, the second solution containing ferric sulfate was added, along with [Fe]Beta seed crystals (0.15 g), to the gel and stirred for an additional 5 min. The resulting gel was then placed into the Teflon liner of an autoclave (Parr 4744) and heated statically at a temperature of 413 K for 15 days. The zeolite particles were filtered and washed with deionized water until the filtrate reached neutral pH. After drying overnight at a temperature of 353 K, the zeolite was calcined in air using the following temperature program: a ramp from room temperature to 423 K in 1 h, a hold at 423 K for 2 h, a ramp from 423 K to 753 K in 3 h, and a final hold at 753 K for 5 h. Following calcination, an ion exchange was carried out overnight at a temperature of 298 K in 0.05 M  $\text{NH}_4\text{NO}_3$  (Sigma Aldrich). The amount of ammonium nitrate used was five times that of the ferric sulfate added to the gel on a molar basis (approximately 1 g  $\text{NH}_4\text{NO}_3$  per 1 g  $\text{Fe(III)}_2(\text{SO}_4)_3$  in the gel). The zeolite was then filtered and rinsed three times in deionized water and dried overnight at a temperature of 353 K.

For nickel exchanged samples, ammonium form [Fe]Beta was ion exchanged overnight at a temperature of 298 K in 0.05 M  $\text{Ni}(\text{NO}_3)_2$  (Sigma Aldrich). The amount of nickel nitrate used was 20% that of the ferric sulfate added to the gel on a molar basis (approximately 0.15 g  $\text{Ni}(\text{NO}_3)_2$  per 1 g  $\text{Fe(III)}_2(\text{SO}_4)_3$  in the gel).

### 5.2.2 Characterization

Sample chemical compositions were determined using a Rigaku Supermini 200 wavelength dispersive X-ray fluorescence spectrometer with a Pd-anode X-ray tube (50 kV, 200 W). Surface area and microporous volumes (calculated using the t-plot method) were determined from N<sub>2</sub> adsorption isotherms measured using a Micromeritics ASAP 2020 instrument. The samples were pretreated at a temperature of 423 K and a pressure of 0.5 torr overnight to remove any adsorbed species. X-ray powder diffraction patterns (PXRD) were measured using a Bruker D8 X-ray diffractometer with a CuK $\alpha$  source ( $\lambda = 1.542\text{\AA}$ ). Diffraction patterns were obtained using a step size of  $0.02^\circ 2\theta$  with 1 s counting time at each step and were measured between  $5^\circ$  and  $50^\circ 2\theta$ . SEM images were taken with a JSM-7400F scanning electron microscope with an accelerating voltage of 3.00 kV. UV/Vis spectra were measured using a Jasco V-550 UV/Vis spectrometer. UV/Vis spectra were measured between wavelengths of 220 nm and 850 nm with a scan rate of 400 nm/min.

### 5.2.3 Catalytic Testing

The reactor system used for catalyst performance testing was the same as described in a previous report [98], except that a syringe pump (Teledyne Isco 260D) was used instead of a HPLC pump to feed the reactant (DME) into the system. An online gas chromatograph (GC) (Agilent 7890B) equipped with a flame ionization detector (FID) was used to analyze reactor effluent. Separation of chemical species within the reactor effluent was performed in the GC with a HP-Plot Q column (Agilent, 30 m x 320  $\mu\text{m}$  ID, 0.20 mm film thickness). Helium was used as the carrier gas and nitrogen was used as the makeup gas. The following temperature program was used for product detection: a 5 minute hold at 333 K, a ramp to 423 K at a rate of 20

K/min, a 3 min hold at 423 K, a ramp to 473 K at a rate of 20 K/min, a 5 min hold at 473 K, a ramp to 523 K, and a final hold at 523 K for 2.5 min.

The catalyst powder was pressed (5000 psi, 13 mm dye), gently crushed and sieved to particle sizes between 250 and 425  $\mu\text{m}$  (40 – 60 mesh). Each experiment was performed using 100-200 mg of the sieved catalyst. Prior to each experiment, the catalyst was calcined *in situ* in air (100 mL/min). For [Al]ZSM-5, the following temperature program was used: a ramp from room temperature to 823 K at a rate of 2 K/min, followed by a hold at 823 K for 5 hrs. For [Fe]Beta, the following temperature program was used: a ramp from room temperature to 673 K at a rate of 2 K/min, followed by a hold at 673 K for 8 hrs.

A variety of reaction conditions were investigated: partial pressure of DME was investigated from 0.14 atm to 0.40 atm and reaction temperature was studied in the range of 573 – 623 K. Partial pressure of DME was controlled by adjusting the flow rate of the nitrogen carrier gas from 60 mL/min down to 15 mL/min. Weight hourly space velocity (WHSV, defined as grams of pentane fed per gram of catalyst per hour) was 11.3  $\text{g}_{\text{DME}}\text{g}_{\text{cat}}^{-1}\text{h}^{-1}$  for [Al]ZSM-5 and 5.7  $\text{g}_{\text{DME}}\text{g}_{\text{cat}}^{-1}\text{h}^{-1}$  for [Fe]Beta. Conversion of reactant was defined as 100% minus the percentage of unreacted feed (DME plus methanol) in the product stream. Product carbon selectivity was defined as the fraction of carbon in each product as compared to the total amount of carbon in the effluent that was not reactant. Comparison of consumption rates and product selectivities were made when the consumption rate was highest (peak DME conversion) for each experiment.

## 5.3 Results

### 5.3.1 Catalyst Characterization

Powder XRD shows that the ferrisilicate synthesis forms a crystalline zeolite product with the BEA\* topology. The materials did not show evidence of any amorphous material or other crystalline phases (Figure 5.4). The micropore volume, as calculated by the t-plot method, was determined to be  $0.25 \text{ cm}^3/\text{g}$ , which is consistent with a highly crystalline zeolite Beta sample. Using XRF spectroscopy, the Si/Fe ratio was determined to be 16 and when nickel was ion-exchanged onto the zeolite, the Ni/Fe ratio was 0.13. UV/Vis spectroscopy of the as made, uncalcined zeolite show three peaks at wavelengths of 374, 415, and 440 nm (Figure 5.5). These peaks are consistent with d-d transitions of tetrahedrally bound iron in a zeolite framework [87]. Upon calcination, these well-defined peaks are lost and only shoulders are present. This is a result of the less-than tetrahedral coordination of iron in the framework caused by the loss of the large charge sphere formed by the presence of the structural directing agent, which helps to diffuse the effects of the positive charge and generates a more symmetric coordination of iron in the framework. SEM images show crystal sizes in the range of 200 – 400 nm with a non-uniform crystal structure (Figure 5.6). EDS imaging techniques were used to show uniform dispersion of iron in the particles.

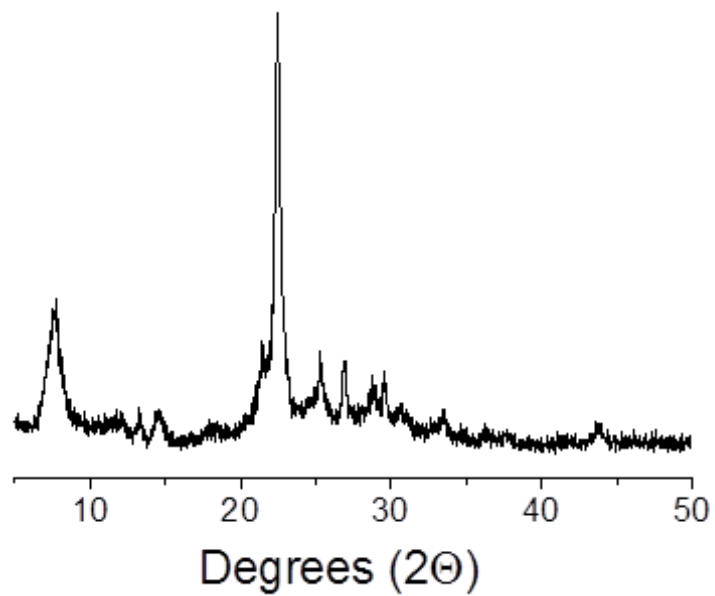


Figure 5.4: X-ray diffraction pattern of NH<sub>4</sub>-[Fe]Beta

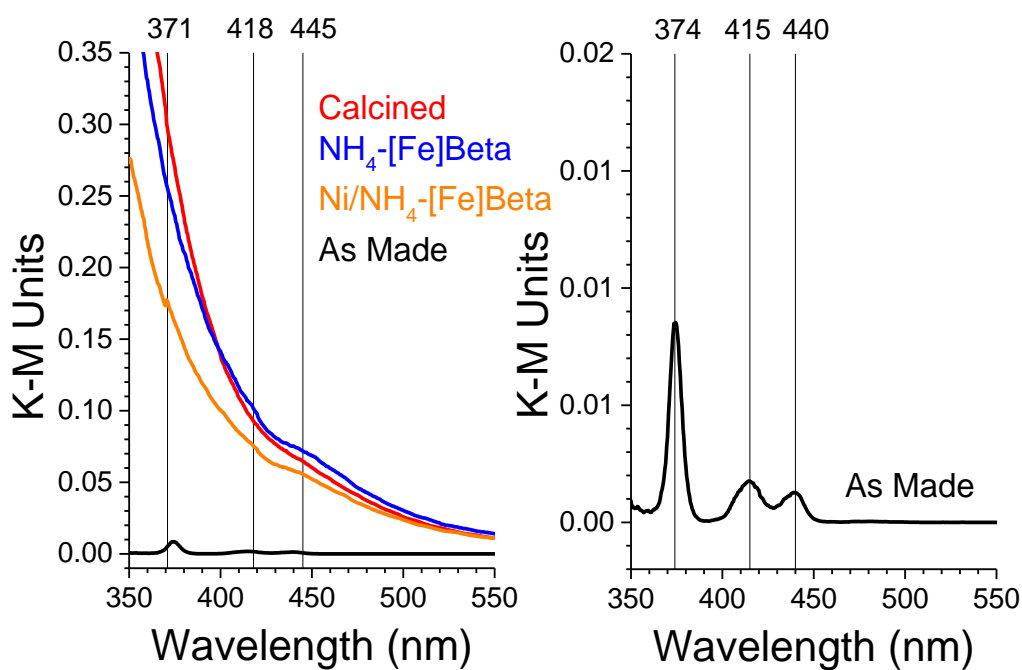


Figure 5.5: UV/Vis spectra of [Fe]Beta throughout the synthesis process (*left*) and UV/Vis of as made [Fe]Beta magnified (*right*)

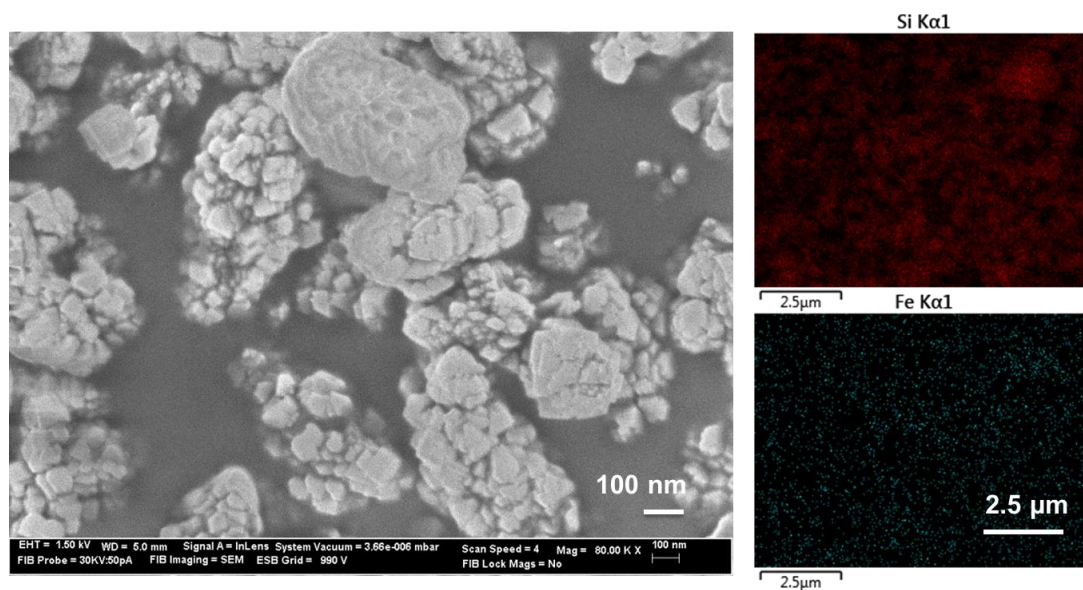


Figure 5.6: SEM of [Fe]Beta (*left*) with silicon EDS (*top right*) and iron EDS (*bottom right*)

### 5.3.2 Catalytic Testing

Conversion of dimethyl ether on acidic H-[Al]ZSM-5 resulted in a peak consumption rate of  $66.8 \text{ mmol}_{\text{DME}}/\text{g}_{\text{cat}}\text{-hr}$  ( $T = 573 \text{ K}$ ,  $P = 1 \text{ atm}$ ,  $P_{\text{DME}} = 0.14 \text{ atm}$ ,  $F_{\text{N}_2} = 60 \text{ mL/min}$ , and  $\text{WHSV} = 11.3 \text{ g}_{\text{DME}}\text{g}_{\text{cat}}^{-1}\text{h}^{-1}$ ). As seen in Figure 5.7, the carbon selectivity of  $\text{C}_2$  to  $\text{C}_6$  and aromatic species was between 10% and 20%, exhibiting a relatively even distribution of molecular weights. Conversion of dimethyl ether on H-[Fe]Beta resulted in a peak consumption rate of  $11.9 \text{ mmol}_{\text{DME}}/\text{g}_{\text{cat}}\text{-hr}$  ( $T = 573 \text{ K}$ ,  $P = 1 \text{ atm}$ ,  $P_{\text{DME}} = 0.14 \text{ atm}$ ,  $F_{\text{N}_2} = 60 \text{ mL/min}$ , and  $\text{WHSV} = 5.7 \text{ g}_{\text{DME}}\text{g}_{\text{cat}}^{-1}\text{h}^{-1}$ ).  $\text{C}_4$  compounds, which were all olefins, were the major products of DME conversion on H-[Fe]Beta, followed by  $\text{C}_5$  compounds, which were mostly pentenes. Unlike H-[Al]ZSM-5, H-[Fe]Beta produced a lower quantity of light olefins, ethylene and propylene. Note that under these reaction conditions, no aromatic products are produced on [Fe]Beta.

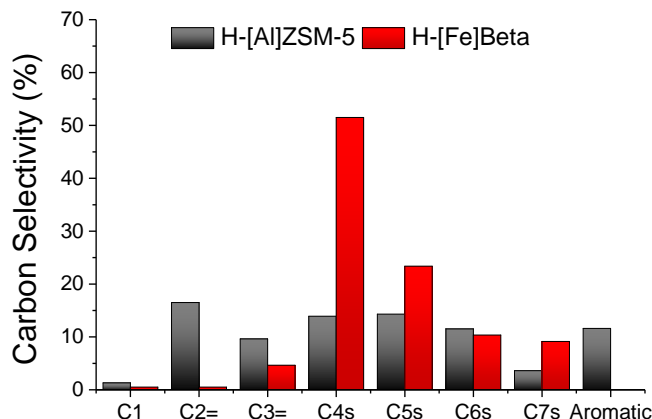


Figure 5.7: Comparison of carbon selectivity of dimethyl ether conversion on H-[Al]ZSM-5 and H-[Fe]Beta. Reaction conditions:  $T = 573$  K,  $P = 1$  atm,  $P_{\text{DME}} = 0.14$  atm,  $F_{\text{N}_2} = 60$  mL/min, and  $\text{WHSV} = 11.3 \text{ g}_{\text{DME}}\text{g}_{\text{cat}}^{-1}\text{h}^{-1}$  (ZSM-5) and  $5.7 \text{ g}_{\text{DME}}\text{g}_{\text{cat}}^{-1}\text{h}^{-1}$  (Beta)

Conversion of dimethyl ether on H-[Fe]Beta ( $T = 573$  K,  $P = 1$  atm,  $P_{\text{DME}} = 0.14$  atm,  $F_{\text{N}_2} = 60$  mL/min, and  $\text{WHSV} = 5.7 \text{ g}_{\text{DME}}\text{g}_{\text{cat}}^{-1}\text{h}^{-1}$ ) exhibited deactivation with increasing time on stream, but reached a steady state at approximately 3 hrs time on stream (Figure 5.8). Although deactivation was observed, product selectivity remained nearly constant with time on stream regardless of DME consumption rates.  $\text{C}_4$  and  $\text{C}_7$  compounds displayed the largest change in carbon selectivity with time on stream. With increasing time on stream, or decreasing DME consumption rates,  $\text{C}_4$  carbon selectivity decreased from approximately 55% to 45%, while  $\text{C}_7$  carbon selectivity increased from approximately 10% to 20%.

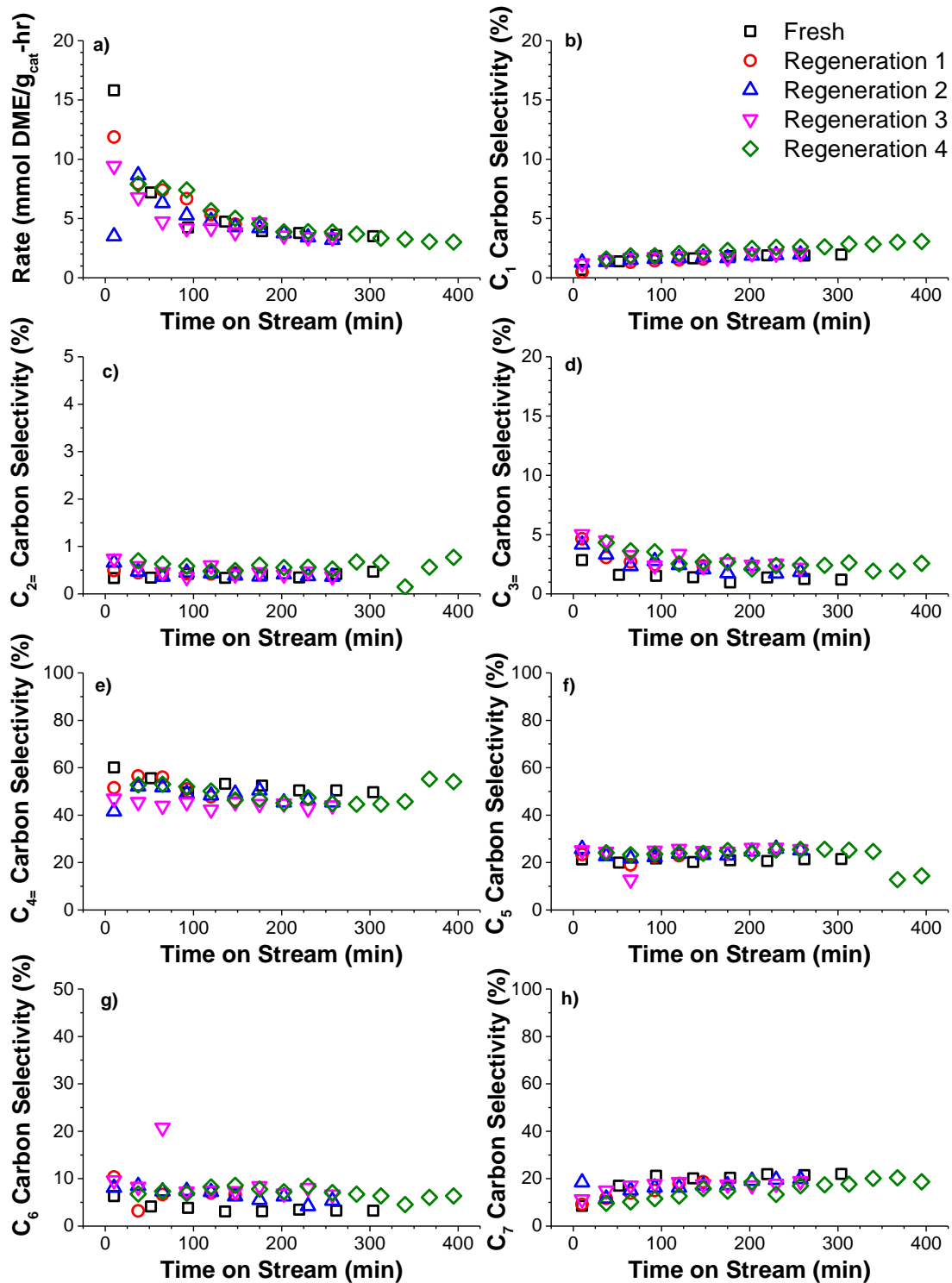


Figure 5.8: Comparison of fresh and regenerated H-[Fe]Beta with regard to dimethyl ether consumption rates (a) and carbon selectivity to methane (b), ethylene (c), propylene (d), C<sub>4</sub> compounds (e), C<sub>5</sub> compounds (f), C<sub>6</sub> compounds (g), and C<sub>7</sub> compounds (h) as a function of time on stream. Reaction conditions:  $T = 573$  K,  $P = 1$  atm,  $P_{\text{DME}} = 0.14$  atm,  $F_{\text{N}_2} = 60$  mL/min, and  $\text{WHSV} = 5.7 \text{ g}_{\text{DME}}\text{g}_{\text{cat}}^{-1}\text{h}^{-1}$

Increasing reaction temperature resulted in an increase in DME consumption rates. Peak DME consumption rates were as follows:  $11.9 \text{ mmol}_{\text{DME}}/\text{g}_{\text{cat}}\text{-hr}$  at  $T = 573$  K,  $17.7 \text{ mmol}_{\text{DME}}/\text{g}_{\text{cat}}\text{-hr}$  at  $T = 588$  K, and  $27.3 \text{ mmol}_{\text{DME}}/\text{g}_{\text{cat}}\text{-hr}$  at  $T = 603$  K ( $P = 1$  atm,  $P_{\text{DME}} = 0.14$  atm,  $F_{\text{N}_2} = 60$  mL/min, and  $\text{WHSV} = 5.7 \text{ g}_{\text{DME}}\text{g}_{\text{cat}}^{-1}\text{h}^{-1}$ ). As seen in Figure 5.9, product selectivity was nearly constant with increasing reaction temperature and only minor changes were observed. Selectivity to C<sub>4</sub> compounds slightly increased with increasing temperature, while C<sub>5</sub> and C<sub>7</sub> compounds slightly decreased. Aromatic species were observed at temperatures above 573 K.

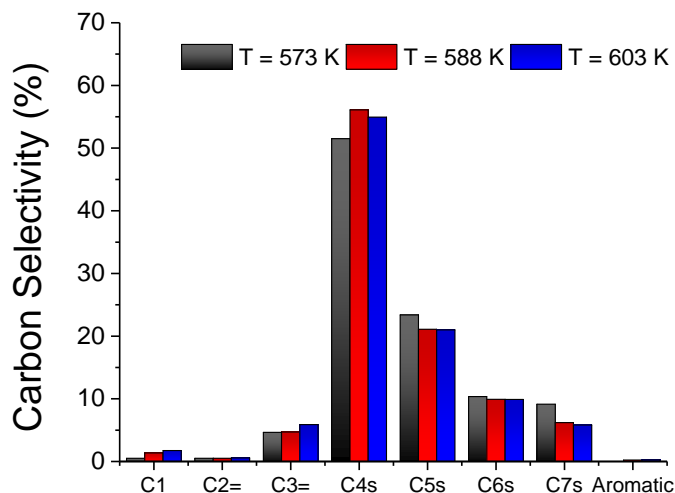


Figure 5.9: Comparison of carbon selectivity of dimethyl ether conversion on H-[Fe]Beta at different reaction temperatures. Reaction conditions:  $T = 573$  -  $603$  K,  $P = 1$  atm,  $P_{\text{DME}} = 0.14$  atm,  $F_{\text{N}_2} = 60$  mL/min, and  $\text{WHSV} = 5.7 \text{ g}_{\text{DME}}\text{g}_{\text{cat}}^{-1}\text{h}^{-1}$

Changes in partial pressure of DME were investigated by adjusting the flow rate of the nitrogen carrier gas. This resulted in changes in residence time within the catalyst bed, but no change in weight hourly space velocity. Peak DME consumption rates were as follows:  $11.9 \text{ mmol}_{\text{DME}}/\text{g}_{\text{cat}}\text{-hr}$  at  $P_{\text{DME}} = 0.14$  atm,  $12.0 \text{ mmol}_{\text{DME}}/\text{g}_{\text{cat}}\text{-hr}$  at  $P_{\text{DME}} = 0.25$  atm, and  $12.9 \text{ mmol}_{\text{DME}}/\text{g}_{\text{cat}}\text{-hr}$  at  $P_{\text{DME}} = 0.40$  atm ( $T = 573$  K,  $P = 1$  atm,  $F_{\text{N}_2} = 60$  mL/min, and  $\text{WHSV} = 5.7 \text{ g}_{\text{DME}}\text{g}_{\text{cat}}^{-1}\text{h}^{-1}$ ). Similarly to changes in reaction temperature, product selectivity was nearly constant with changing DME partial pressure (Figure 5.10). Aromatic formation was observed at a DME partial pressure of 0.40 atm.

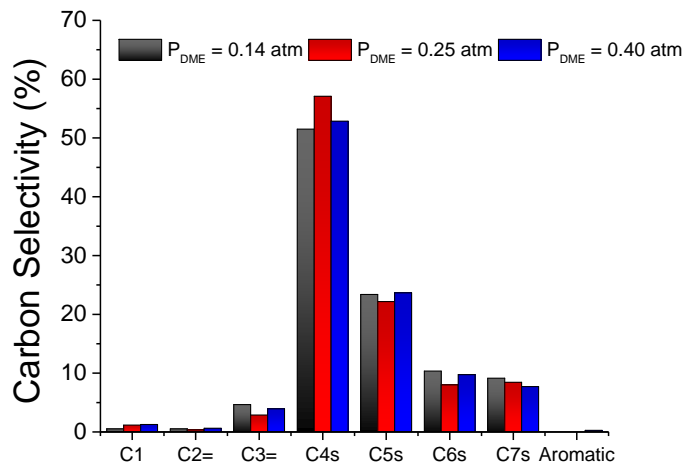


Figure 5.10: Comparison of carbon selectivity of dimethyl ether conversion on H-[Fe]Beta at different DME partial pressures. Reaction conditions:  $T = 573$  K,  $P = 1$  atm,  $P_{DME} = 0.14 - 0.40$  atm,  $F_{N_2} = 60$  mL/min, and WHSV = and  $5.7 \text{ g}_{DME} \text{ g}_{cat}^{-1} \text{ h}^{-1}$

Ion exchange of nickel onto H-[Fe]Beta resulted in a decrease in DME peak consumption rate from  $11.9 \text{ mmol}_{DME} / \text{g}_{cat} \cdot \text{hr}$  to  $1.8 \text{ mmol}_{DME} / \text{g}_{cat} \cdot \text{hr}$  ( $T = 573$  K,  $P = 1$  atm,  $P_{DME} = 0.14$  atm,  $F_{N_2} = 60$  mL/min, and WHSV =  $5.7 \text{ g}_{DME} \text{ g}_{cat}^{-1} \text{ h}^{-1}$ ). Significant changes in product selectivity were also observed (Figure 5.11). Addition of nickel resulted in a six-fold increase in methane selectivity as well as increases in selectivity to ethylene and propylene. Selectivity to  $C_4$  compounds decreased from approximately 55% to 25% and  $C_5$  compounds were the major species produced.

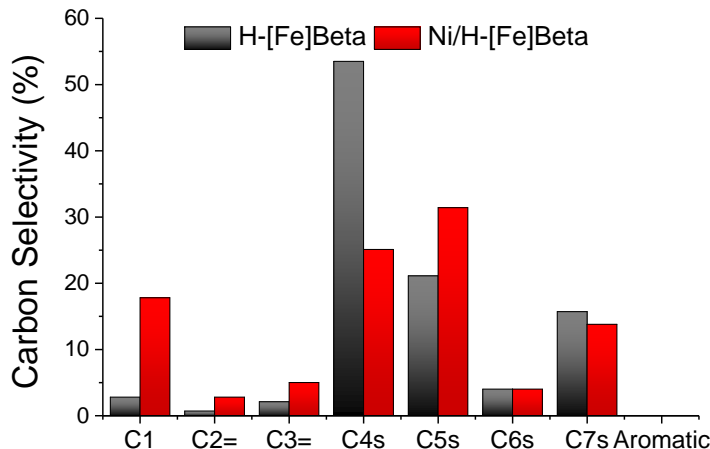


Figure 5.11: Comparison of carbon selectivity of dimethyl ether conversion on H-[Fe]Beta and Ni/H-[Fe]Beta. Reaction conditions:  $T = 573$  K,  $P = 1$  atm,  $P_{\text{DME}} = 0.14$  atm,  $F_{\text{N}_2} = 60$  mL/min, and  $\text{WHSV} = 5.7 \text{ g}_{\text{DME}}\text{g}_{\text{cat}}^{-1}\text{h}^{-1}$

Unlike DME conversion on H-[Fe]Beta, increasing DME partial pressure for DME conversion of Ni/H-[Fe]Beta caused an increase in peak DME consumption rate from  $1.8 \text{ mmol}_{\text{DME}}/\text{g}_{\text{cat}}\text{-hr}$  at  $P_{\text{DME}} = 0.14$  atm to  $6.1 \text{ mmol}_{\text{DME}}/\text{g}_{\text{cat}}\text{-hr}$  at  $P_{\text{DME}} = 0.25$  atm ( $T = 573$  K,  $P = 1$  atm,  $F_{\text{N}_2} = 60$  mL/min, and  $\text{WHSV} = 5.7 \text{ g}_{\text{DME}}\text{g}_{\text{cat}}^{-1}\text{h}^{-1}$ ). There was also a shift in product selectivity (Figure 5.12). While selectivity to methane and  $\text{C}_5$  compounds increased the most when H-[Fe]Beta was partially exchanged with nickel, increased DME partial pressure caused the largest decrease in selectivity to these species and  $\text{C}_4$  compounds were the major product.

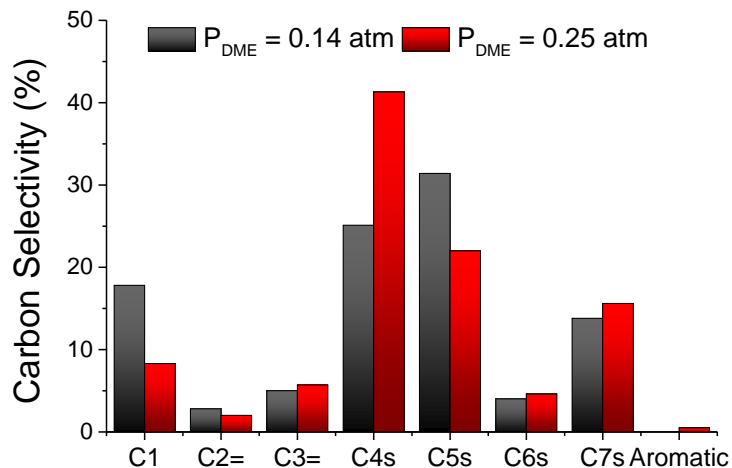


Figure 5.12: Comparison of carbon selectivity of dimethyl ether conversion on Ni/H-[Fe]Beta at different DME partial pressures. Reaction conditions:  $T = 573$  K,  $P = 1$  atm,  $P_{DME} = 0.14 - 0.25$  atm,  $F_{N_2} = 60$  mL/min, and  $WHSV =$  and  $5.7 \text{ g}_{DME} \text{ g}_{cat}^{-1} \text{ h}^{-1}$

#### 5.4 Discussion

H-[Al]ZSM-5 exhibited dimethyl ether consumption rates five times higher than H-[Fe]Beta even though the ZSM-5 sample had a lower acid site density (Si/Al = 40 vs Si/Fe = 16). The higher consumption rates on H-[Al]ZSM-5 compared to H-[Fe]Beta are consistent with the influence of acid strength on catalytic activity of methanol conversion to hydrocarbons [169,170]. Similarly to conversion of methanol on H-[Fe]ZSM-5, H-[Fe]Beta exhibited a high carbon selectivity to olefins (>90%), while producing low amounts of aromatics, relative to aluminum containing zeolites [155,156]. Gas chromatography / mass spectrometry (GC/MS) was performed to elucidate the structure of the olefinic species produced.

Reactor effluent from conversion of DME on H-[Fe]Beta at a temperature of 593 K and DME partial pressure of 0.14 atm was collected and analyzed via GC/MS

with the same HP-Plot Q column used in GC analysis. MS fragmentation patterns were compared to reference patterns from the NIST database (Appendix C). The closest matches from GC/MS are summarized below in Table 5.1.

Table 5.1 Carbon selectivity and research octane number (RON) of species identified via GC/MS from DME conversion on H-[Fe]Beta. Reaction conditions:  $T = 593$  K,  $P = 1$  atm,  $P_{\text{DME}} = 0.14$  atm,  $F_{\text{N}_2} = 60$  mL/min, and WHSV = and  $5.7 \text{ g}_{\text{DME}}\text{g}_{\text{cat}}^{-1}\text{h}^{-1}$

Compound	Carbon Selectivity (%)	RON
Methane	1.7	120.0
Ethene	0.6	97.3
Propene	4.5	101.8
<i>i</i> -butane	---	102.1
<b><i>i</i>-butene</b>	<b>49.3</b>	<b>106.3</b>
2-butene	3.0	101.6
2-methyl-1-butene	0.3	98.3
2-methylbutane	3.0	93.0
2-pentene	3.6	87.8
2-pentene	2.1	87.8
<b>2-methyl-2-butene</b>	<b>13.3</b>	<b>97.3</b>
2,3-dimethyl-1-butene	1.4	101.3
2,3-dimethylbutane	0.2	104.3
2-methyl-1-pentene	0.6	94.2
2-methyl-2-pentene	2.3	97.8
3-hexene	1.5	94.0
3-methyl-2-pentene	1.3	97.2
2,3-dimethyl-2-butene	2.5	97.4
<b>triptene</b>	<b>4.9</b>	<b>105.3</b>
Other C <sub>7=</sub>	3.6	90-105
<i>o,p</i> -Xylene	0.3	146.0

One limitation of the GC technique was inefficient separation of compounds with the GC column. These inefficient separations were most notable in the following:

methanol and C<sub>4</sub> compounds, C<sub>4</sub> isomer separation, and separation of C<sub>7+</sub> compounds. MS analysis revealed isobutane was present within the methanol peak and 2-butene was present in butane (butane was a contaminant in the DME feed and was subtracted out during analysis as it was determined in control experiments to be an unreactive spectator). While isobutane could not be separated from methanol and therefore could not be quantified, its presence still must be considered in the development of the reaction network of this system. Also, while we were able to separate and quantify one isomer of 2-butene, the other isomer was subtracted out with the butane contaminant, leading to an underestimation in 2-butene production. A similar inefficient separation of C<sub>7</sub> compounds was also observed. MS analysis of the peak attributed to triptene revealed the presence of other C<sub>7</sub> olefins. There were also numerous small convoluted peaks that were revealed to be C<sub>7</sub> olefins, but because of the irregular shape, could not be quantified (Figure C.1). This led to an underestimation in the production of C<sub>7</sub> compounds.

The presence of four saturated compounds (methane, isobutane, isopentane, and 2,3-dimethylbutane) is evidence of hydride transfer reactions occurring in this reaction system. The formation of species with H/C ratios greater than two must be accompanied by the formation of species with H/C ratios less than two in order to conserve mass. While aromatic species are observed at reaction temperatures greater than 573 K or DME partial pressures greater than 0.25 atm, the amount produced is not sufficient to complete the H/C balance. Two possibilities exist to complete the H/C balance: formation of carbonaceous deposits that lead to catalyst deactivation could be forming with H/C ratios less than two or other aromatic species are forming at

concentrations too low to be observed through GC analysis or are inadequately separated from other compounds and therefore not observed.

As reported by Ahn et al., selectivity to species with 1 to 3 carbons was low, selectivity to species with 4 and 7 carbons was high, and selectivity to species with 5 carbons was greater than those with 6 carbons (Table 5.2) [153]. While product carbon selectivity does not match exactly, similar trends were observed with DME conversion on H-[Fe]Beta. The most notable differences are in the C<sub>7</sub> and C<sub>8+</sub> fractions. Low C<sub>7</sub> selectivity can be attributed to inefficient GC column separation and inability to be quantified, while low C<sub>8+</sub> selectivity can be attributed to low aromatic formation rates. Another possible explanation for the lower C<sub>7</sub> selectivity could be attributed to the lower rates of hydride transfer reactions on H-[Fe]Beta. Based on the reaction mechanism proposed by Hazari et al. (Figure 5.3), triptene is consumed via two competing pathways: hydride transfer or methylation. With lower rates of hydride transfer reactions on H-[Fe]Beta, triptene would be consumed mostly via methylation, leading to the formation of a C<sub>8</sub> compound. The C<sub>8</sub> compound undergoes isomerization followed by cracking to produce isobutene. This would also explain the higher selectivity to C<sub>4</sub> compounds, specifically *iso*-C<sub>4</sub>, for H-[Fe]Beta compared to H-[Al]Beta.

Table 5.2: Comparison of carbon selectivity of dimethyl ether conversion on H-[Fe]Beta and H-[Al]Beta. Reaction conditions: <sup>a</sup> $T = 573 \text{ K}$ ,  $P = 1 \text{ atm}$ ,  $P_{\text{DME}} = 0.14 \text{ atm}$ ,  $F_{\text{N}_2} = 60 \text{ mL/min}$ , and  $\text{WHSV} = 11.3 \text{ g}_{\text{DME}}\text{g}_{\text{cat}}^{-1}\text{h}^{-1}$  and <sup>b</sup> $T = 473 \text{ K}$ ,  $P = 10 \text{ atm}$ ,  $P_{\text{DME}} = 1.2 \text{ atm}$ ,  $F_{\text{N}_2} = 16.7 \text{ mL/min}$ , and  $\text{WHSV} = 0.7 \text{ g}_{\text{DME}}\text{g}_{\text{cat}}^{-1}\text{h}^{-1}$

Carbon Number	Carbon Selectivity (%)	
	H-[Fe]Beta <sup>a</sup>	H-[Al]Beta <sup>b</sup>
1	1.7	2
2	0.6	1
3	4.5	5
4	52.4	29
5	22.3	8
6	9.8	6
7	8.4	31
8+	0.3	18

Similar trends were also observed with changes in reaction temperature and pressure. For both H-[Al]Beta and H-[Fe]Beta, increasing reaction temperature caused a decrease in selectivity to C<sub>7</sub> species (Figure 5.9). Also, changes in DME partial pressure resulted in only small variations in product selectivity for DME conversion on both H-[Al]Beta and H-[Fe]Beta (Figure 5.10). When comparing dimethyl ether conversion on H-[Al]Beta and H-[Fe]Beta, both catalysts exhibit a high selectivity to C<sub>4</sub> compounds (specifically branched C<sub>4</sub> species), a high selectivity to triptyl species within the C<sub>7</sub> fraction, similar ratios in product selectivity, and similar changes in product selectivity with changes in reaction temperature and DME partial pressure.

Conversion of dimethyl ether on H-[Fe]Beta resulted in the formation of only three hydrogenated olefins: isobutane, 2-methylbutane, and 2,3-dimethylbutane. The olefins from which these three paraffins are formed from are the most energetically favored species produced during the subsequent methylation of propylene (Figure 5.13). The energetic favorability of the olefins formed is based on the stability of the carbocation intermediate (tertiary > secondary > primary) and the stability of the final olefin product (tetraalkyl > trialkyl > dialkyl > monoalkyl). The formation of these species is consistent with the reaction network proposed by Hazari et al.

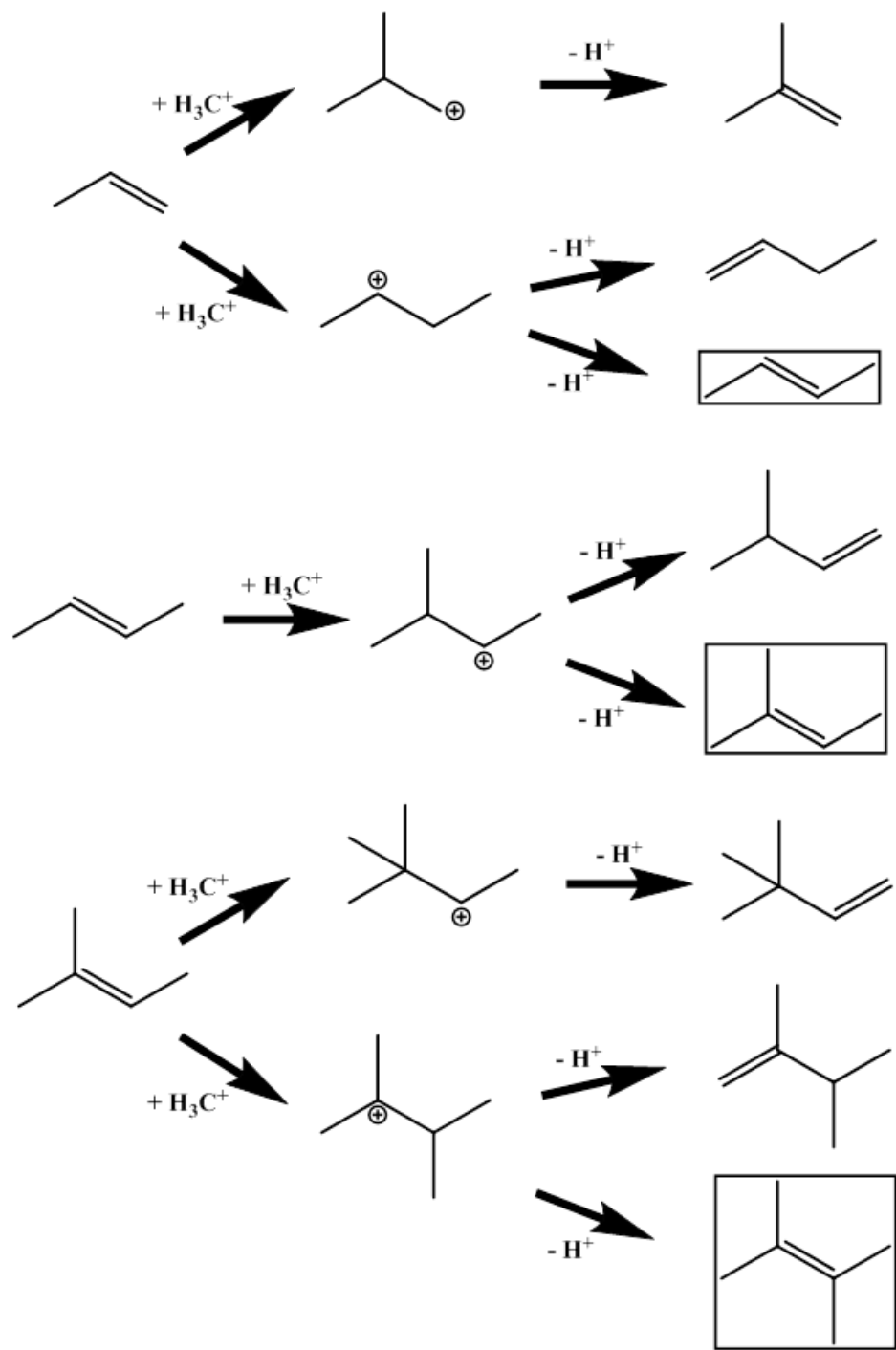


Figure 5.13: Most energetically favorable species, based on the stability of the carbocation intermediate and subsequent olefin formed from deprotonation, produced by successive methylation of propylene

When comparing conversion of dimethyl ether on H-[Al]Beta and H-[Fe]Beta, both catalysts exhibited high selectivity to branched C<sub>4</sub> compounds and triptyl compounds within the C<sub>7</sub> fraction, similar trends in product selectivity with changes in temperature and DME partial pressure, and similar trends with product selectivity based on carbon number. Considering all of these factors, it appears that conversion of DME on H-[Fe]Beta occurs via a similar reaction network as H-[Al]Beta. The major difference between the two catalysts is that H-[Fe]Beta produces olefins with high selectivity (specifically isobutene, 2-methyl-2-butene, and triptene), whereas H-[Al]Beta produces paraffins and aromatics with high selectivity (specifically isobutane, triptane, and hexamethylbenzene) (Figure 5.14).

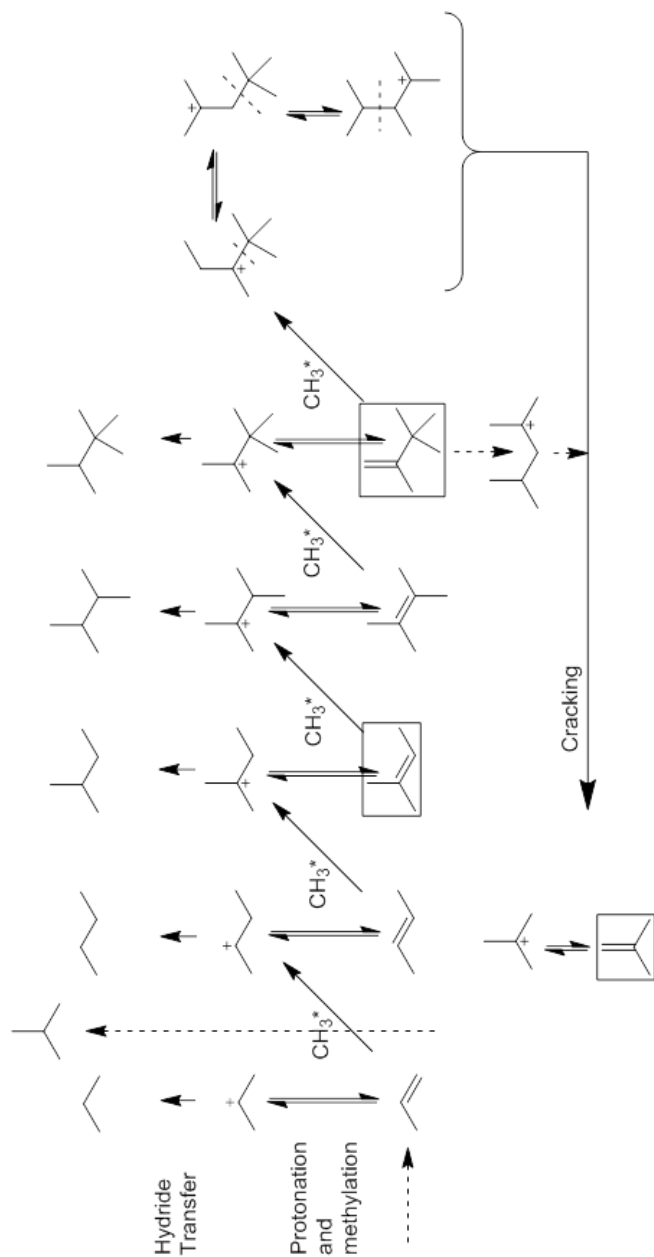


Figure 5.14: Reaction network for methanol conversion on H-[Al]Beta modified to reflect the high selectivity to olefins (particularly isobutene, 2-methyl-2-pentene, and triptene) and low selectivity to paraffins on H-[Fe]Beta. Recreated from publication by Hazari et al. [154]

Having established that conversion of dimethyl ether with H-[Fe]Beta produced olefins at high selectivities (>90%), a partial nickel ion exchange was performed to promote olefin oligomerization. Addition of nickel resulted in a decrease in DME consumption rates, which is expected as it is the acid sites that catalyze methylation reactions and a fraction of the acid sites were lost from nickel ion-exchange. Also, addition of nickel led to a decrease in selectivity to C<sub>4+</sub> compounds. The ratio of C<sub>4</sub>-C<sub>7</sub> to C<sub>1</sub>-C<sub>3</sub> carbon selectivity decreased from 17 to 3 when nickel was added, with a large increase in methane selectivity from 3% to 18%. Supported nickel is a known methanation catalyst and even though ion exchanged nickel is a cation (2+ charge) instead of metallic, it could potentially be enhancing a methanation reaction [171]. Unlike H-[Fe]Beta, increasing DME partial pressure caused a significant change in product selectivity. The ratio of C<sub>4</sub>-C<sub>7</sub> to C<sub>1</sub>-C<sub>3</sub> carbon selectivity increased from 3 to 5 with increasing DME partial pressure, which suggests that nickel could be promoting oligomerization reactions as no major changes were observed with H-[Fe]Beta.

## 5.5 Conclusion

Conversion of dimethyl ether on H-[Fe]Beta produced olefins with high selectivity (>90%). Isobutene was the major product (>50% selectivity) and 95% or more of the olefins produced were heavier than propylene. Within the C<sub>7</sub> fraction, triptene was the major compound formed. When compared to dimethyl ether conversion on H-[Al]Beta, H-[Fe]Beta exhibited similar trends in product selectivity based on carbon number and changes in reaction conditions. Both catalysts also showed high selectivity to branched C<sub>4</sub> species and triptyl species within the C<sub>4</sub> and C<sub>7</sub> fractions, respectively. This evidence suggests that conversion of dimethyl ether on H-

[Al]Beta and H-[Fe]Beta occurs via a similar reaction network, where product distribution is controlled by an olefinic cycle. The olefins produced are rapidly converted to paraffins via hydride transfer reaction catalyzed by the strong acidity of H-[Al]Beta, but the moderate acidity of H-[Fe]Beta does not enhance these hydride transfer reaction as strongly and preserves the olefinic product. Partial nickel ion exchange had the opposite effect than intended. Instead of promoting molecular weight growth, the selectivity to compounds heavier than propylene decreased from 94% to 74%. A large increase in methane formation was also observe, but this side methanation reaction most likely occurs via a mechanism separate from the main reaction network.

H-[Fe]Beta was able to selectively produce olefins heavier than ethylene and propylene, which are the olefins mainly produced in industrial MTO processes. Although nickel did not promote molecular weight growth as intended, the compounds produced have a high research octane number (RON) of 90 to 105. This would allow direct blending into gasoline as an octane booster. Alternatively, isobutene was the major compound produced and could be used as a precursor for polybutyl rubbers or other chemicals such as methyl *tert*-butyl ether (MTBE).

## Chapter 6

### RECOMMENDATIONS AND CONCLUSIONS

In this chapter, I will discuss some future directions to consider with regard to aircraft endothermic cooling, alternative uses of Mo/H-[B]ZSM-5, and alternative catalysts for methanol to hydrocarbons. Future considerations include altering of target reactions and catalyst design considerations. Finally, I discuss the main conclusions of this thesis and the end impact for the average person.

A major challenge of hydrocarbon conversion processes is having high reaction rates that convert the feed molecules into the desired product molecules while having low reaction rates for reactions that may consume the feed or desired product molecules and produce undesirable byproducts. Catalysts can be used to enhance the desired reactions, while not enhancing or suppressing undesired reactions. In this thesis, zeolites were used to catalyze reactions and altering the heteroatom substituted into the framework, metal cation addition, and framework type was used to control product selectivity.

In Chapter 3, H-[Al]ZSM-5, which has a strong acidity, was used to catalyze high-pressure *n*-pentane cracking for aircraft endothermic cooling. Conversion of pentane on H-[Al]ZSM-5 occurred with high reaction rates, but poor selectivity to the desired light olefinic product (C<sub>2=</sub> - C<sub>4=</sub>). These light olefins are the primary product of pentane cracking, but they were rapidly consumed via secondary bimolecular reactions, such as oligomerization and hydride transfer. While the overall process was

endothermic, the endothermicity of was reduced by these secondary bimolecular reactions.

In Chapter 4, Mo/H-[B]ZSM-5, which is a low-acidity zeolite, was used to catalyze high-pressure dehydrogenation of C<sub>5</sub>-C<sub>7</sub> normal alkanes. Dehydrogenation was investigated as it is more endothermic than cracking and dehydrogenation catalysts do not promote oligomerization reactions. It was shown that by using H-[B]ZSM-5 as a support for molybdenum instead of a porous metal oxide, such as  $\gamma$ -Al<sub>2</sub>O<sub>3</sub>, reactant consumption rates were increased while maintaining high selectivity to olefins. Also, by using H-[B]ZSM-5 instead of H-[Al]ZSM-5 as a molybdenum support, the secondary bimolecular reactions that led to molecular weight growth and reduced endothermicity, were suppressed.

In Chapter 5, H-[Fe]Beta, which has a moderate acidity, was used to catalyze dimethyl ether conversion to produce olefins. Conversion of dimethyl ether on H-[Fe]Beta produced olefins with a high selectivity (>90%). In addition, selectivity to olefins heavier than ethylene and propylene, which are produced industrially in methanol-to-olefin processes, was over 90%. Nickel was partially ion exchanged to promote oligomerization of the olefins formed, but had the opposite effect and increased selectivity to methane, ethylene, and propylene.

## **6.1 Suggestions for Future Work**

### **6.1.1 Enhancing Aircraft Endothermic Cooling**

While the actual operating conditions of aircraft endothermic cooling are classified, a test can be performed to measure heats of reactions and catalyst deactivation. Our collaborators at United Technologies Research Center have access to

an “endothermic test rig” (Figure 6.1). To measure heats of reactions, a slurry is made by suspending the catalyst particle in a feed compound. The furnace is set to a given temperature and held at that temperature for 20 min to ensure a steady state temperature has been achieved. With a stable temperature in the furnace, a volume of the slurry is sent through a reactor tube within the furnace. A temperature drop is detected and the energy required to reheat the furnace is recorded as the heat of reaction. This slurry injection process was repeated at increasing temperatures until the pressure drop across the reactor reached 13 bar.

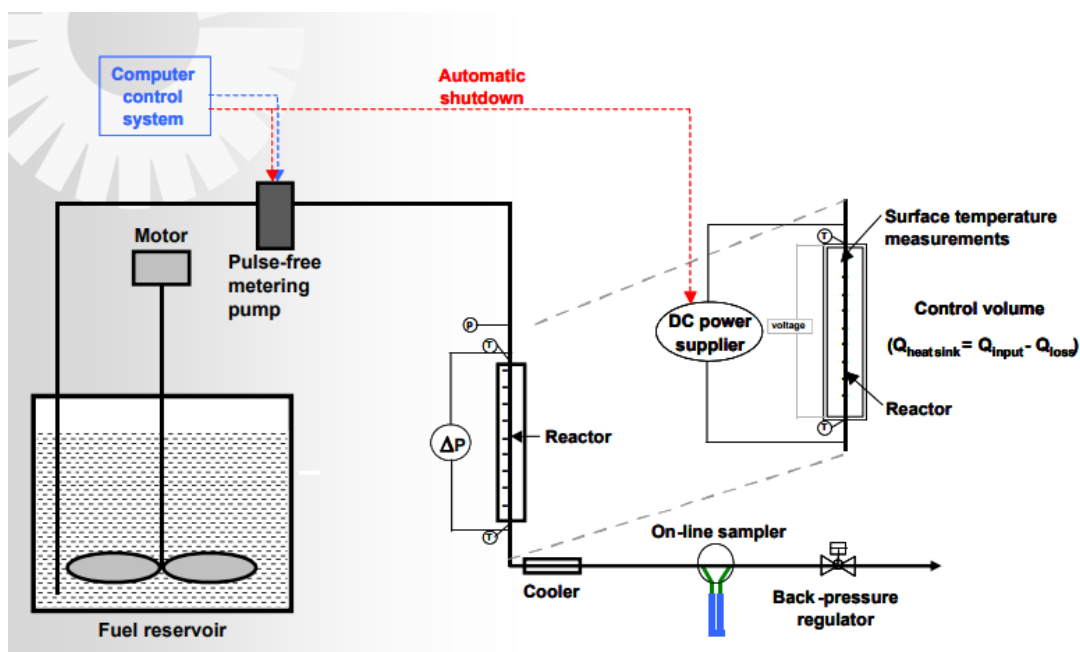


Figure 6.1: Process flow diagram of endothermic test rig used to measure endothermicity of a reactant and catalyst. Adapted from Huang et al. [172].

As seen in Figure 6.2, a slurry of 1.1% (w/w) Mo/H-[B]ZSM-5 / *n*-dodecane was compared to *n*-dodecane thermal decomposition and the physical heat capacity of *n*-dodecane. By adding Mo/H-[B]ZSM-5, *n*-dodecane conversion exhibited an onset temperature approximately 100 K lower than thermal decomposition. In addition, at the highest temperature, 942 K, Mo/H-[B]ZSM-5 increased the reaction endothermicity by approximately 230 kJ/kg. While there was a decrease in onset temperature and an increase reaction endothermicity, the majority of reaction endothermicity (>80 %) is attributed to thermal decomposition of *n*-dodecane.

Instead of controlling the products of the initial reaction, I would like to suggest that it may be more beneficial to target secondary conversion of products formed by thermal decomposition. For example, it may be better to target hexane or hexene conversion instead of dodecane conversion. Alternatively, providing a parallel reaction that aids in limiting catalyst deactivation, such as *in situ* hydrogen generation to target hydrogenation of aromatic coke precursors, may increase catalyst lifetime. For example, Habib et al. investigated hydrocracking of a model vacuum residual compound, 1,3,6,8-tetrahexylpyrene, in the presence of sulfided-iron, a hydrogenation catalyst, and tetralin, a solvent hydrogen donor [173]. They found that sulfide-iron and tetralin did not affect the hydrocracking reaction, but reduced the amount of coke formed during the reaction.

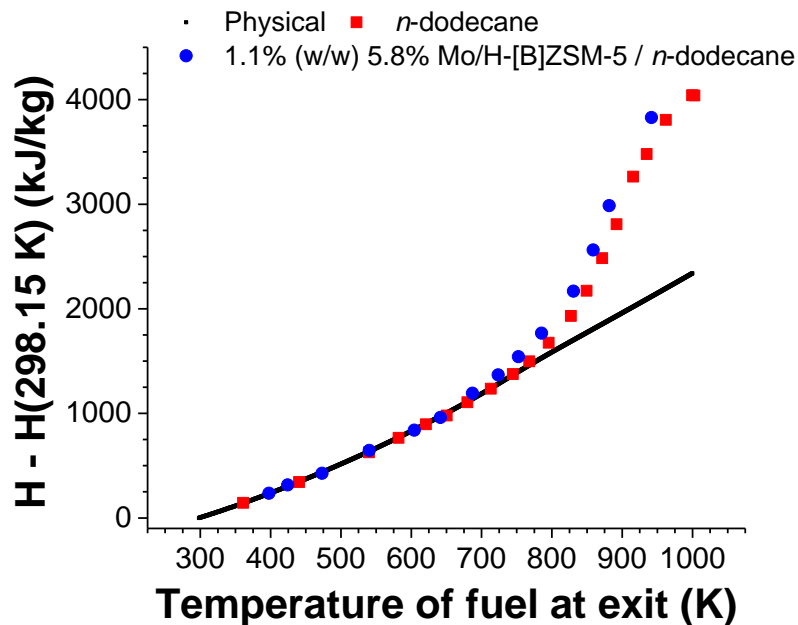


Figure 6.2: Comparison of heat absorbed by thermal decomposition of *n*-dodecane and conversion of *n*-dodecane with Mo/H-[B]ZSM-5 as a function of temperature

### 6.1.1.1 Selective Heteroatom Site Incorporation

Being able to control the precise framework site for heteroatom incorporation could greatly enhance the tunability of zeolite catalytic activity. One example is mordenite. Mordenite consists of straight 12 member ring (MR) channels that offer increased diffusion rates of large molecules, but the increased pore size allows for bimolecular reactions to occur, as there is space for the bulky transition states to form. Connecting the 12 member ring straight channels are side pockets that are only accessible through 8 member ring windows (Figure 6.3).

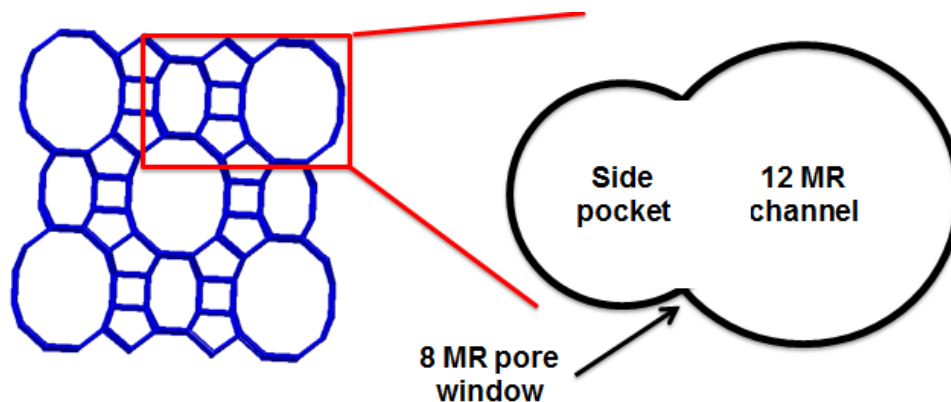


Figure 6.3: Depiction of mordenite structure with 12 member ring straight channels connected via 8 member ring side pockets

In work by Gounder and Iglesia, it is shown there is a measurable difference in monomolecular alkane cracking, which is more favorable in the 12 MR channels, and dehydrogenation, which is more favorable in the 8 MR side pockets, by varying the extent of sodium ion exchange, which preferentially occurs in the 12 member ring channels [174]. By isolating the acid sites in the side pockets of an 8x12 MR zeolite, such as mordenite, the 8 MR windows would restrict access of larger molecules to the side pocket, while the spatial constraint of the side pocket could decrease rates of bimolecular reactions. Using the secondary conversion of dodecane as an example, the dodecane could travel through the 12 MR pores and crack homogeneously. The smaller products of the primary homogeneous cracking of dodecane, such as hexane and hexene, could then access the side pockets and react heterogeneously with the acid sites.

While the structure of mordenite offers the opportunity to utilize smaller side pockets to restrict bimolecular reactions, there still remains difficulty in selectively incorporating aluminum into these pockets instead of in the 12 member ring channels.

The difficulty arises with the number of T-sites (T=tetrahedral) in this framework. Mordenite has 4 T-sites and to selectively incorporate aluminum into the framework at a specific T-site could be accomplished by designing a structural directing agent where the quaternary ammonium sits inside the 8 member ring channel, aiding in directing heteroatom incorporation there. Iorio et al. has shown that by synthesizing chabazite, which has 1 T-sites, with only N,N,N-trimethyl-1-adamantylammonium hydroxide (TMAdaOH) and no added mineralizing agent (i.e. KOH), one aluminum is incorporated per cage [175]. This arises from each cage only being able to accommodate one template molecule. With only one positive charge present per cage, only one aluminum can be incorporated per cage. While mordenite is synthesized without the use of a template, this principle could potentially be applied to the synthesis of ZSM-10, which also has 12 member ring straight channels connected by 8 member ring side pockets, or other zeolites that have similar 12x8 structures.

## **6.1.2 Further Improvements on Mo/H-[B]ZSM-5**

### **6.1.2.1 Active Site Structure Elucidation**

From a combination of X-ray absorption, operando infrared and Raman spectroscopy, and density functional theory calculations, three proposed structures of molybdenum supported on H-[Al]ZSM-5 have been proposed (Figure 6.4) [16,136]. According to theoretical calculations, the most stable form is molybdenum oxide species bridging two aluminum sites, followed by anchoring on one aluminum site, and finally anchoring on silanol groups. These species have all been observed spectroscopically during the calcination step following incipient wetness impregnation.

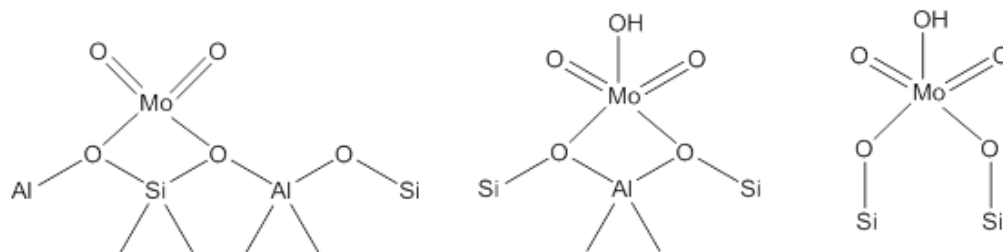


Figure 6.4: Representation of three possible molybdenum oxide anchored sites: bridged (*left*), single aluminum (*middle*), and silanol (*right*)

During carburization, molybdenum atoms migrate and form clusters of 4 molybdenum atoms and two carbon atoms anchored to an aluminum site. X-ray absorption spectroscopy of Mo/H-[Al]ZSM-5 and Mo/H-[B]ZSM-5 show similar changes during carburization, suggesting that similar species may be forming (Figure 6.5). It has already been shown that boron is necessary to enhance catalytic activity (Chapter 4) and our samples have been sent to Lehigh University for testing in the same operando IR and Raman spectroscopy as reported by Gao et al.

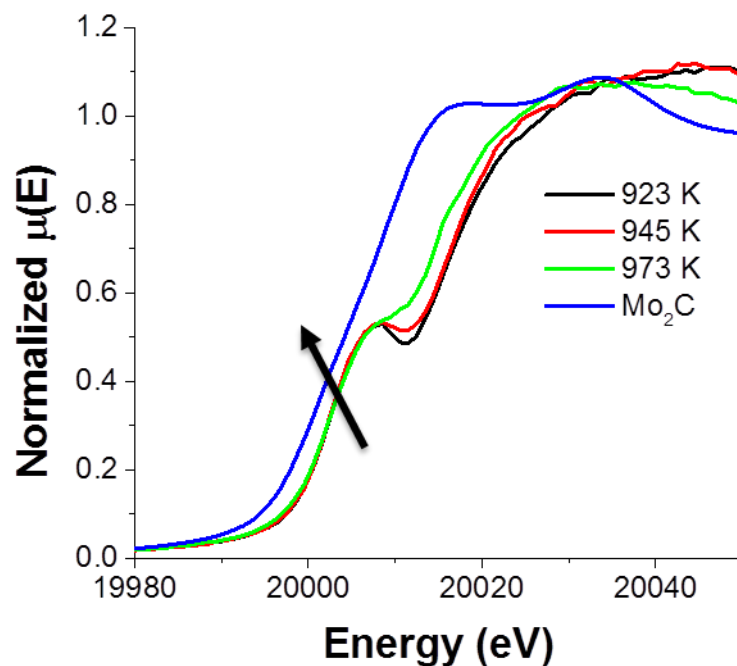


Figure 6.5: In situ XANES of 1% Mo/H-[B]ZSM-5 showing the transition from isolated molybdenum oxide to molybdenum carbide species

Catalyst deactivation is also important to understand. While Mo/H-[B]ZSM-5 remains active through successive regenerations ( $T = 823 \text{ K}$ ,  $F = 100 \text{ mL/min air}$ ,  $t = 5 \text{ hrs}$ ), after 4 or 5 regeneration cycles, the activity of the catalyst falls to that of Mo/Silicalite-1. Combining successive carburization and regeneration cycles in the operando IR and Raman cell could show the formation and loss of the active species by tracking the increase and decrease in the spectral bands corresponding to the bonds between molybdenum, oxygen, and boron. If the boron is leaching out of the framework during regeneration, there will eventually be no evidence of the active species following carburization. Since deactivation of the catalyst is observed during individual runs, a constant regeneration may need to be performed industrially, and by understanding the rate at which boron is extracted from the framework during

regeneration will allow for the proper continuous addition of fresh catalyst and removal of spent catalyst. Additionally, if boron is leaching out of the framework, use of an operando IR/Raman cell could allow for tuning of the regeneration process by altering temperature, flow rates, and gas composition to reduce the amount of boron removed.

#### **6.1.2.2 Alternative Applications**

While Mo/H-[B]ZSM-5 was originally tested for catalytic dehydrogenation, metal carbides can also catalyze other reactions. For example, carbides have been shown to promote hydrodeoxygenation reactions [119,176,177]. With increased dispersion of metal ions on boron sites in the framework, increased reaction rates may be achieved compared to bulk carbides.

Hydrodesulfurization may also be of interest. Currently, sulfided MoCo/Al<sub>2</sub>O<sub>3</sub> or MoNi/Al<sub>2</sub>O<sub>3</sub> are used industrially for removal of sulfur in the petrochemical industry [178,179]. Just as a molybdenum carbide species form during carburization of Mo/H-[B]ZSM-5, a molybdenum sulfide may also potentially form and could catalyze hydrodesulfurization [180].

#### **6.1.3 Increasing Yield of Heavier Hydrocarbons in MTO**

In order to form heavier hydrocarbons from the methanol-to-olefins process, diffusion limitations will need to be considered. Oligomerization in zeolite Beta becomes diffusion limited when C<sub>12+</sub> species are formed [181]. One strategy that has been applied to a number of catalytic systems to reduce diffusion limitations is to use hierarchical zeolites [182]. One type of hierarchical zeolite contains mesoporous networks in the crystal structure (Figure 6.6).

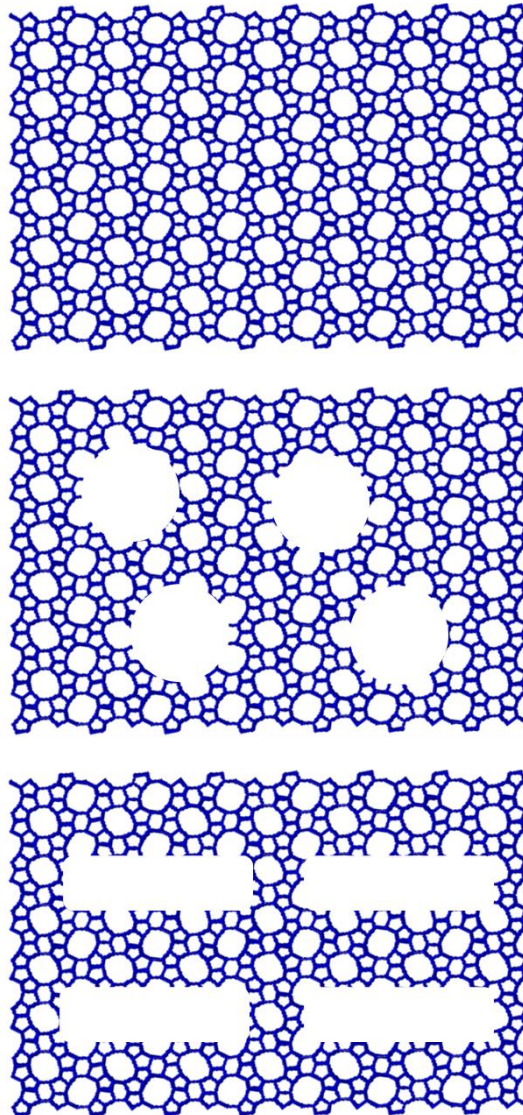


Figure 6.6: Example of the crystal structure of a standard zeolite (*top*), a hierarchical zeolite with mesoporous channels (*middle*), and a hierarchical pillared zeolite (*bottom*)

Another class of hierarchical zeolites is pillared zeolites. These mesoporous materials consist of sheets of zeolite crystal only a few unit cells in depth connected together via “pillars”. They can be made in one step by utilizing multifunctional

structural directing agents or the nano sheets can be synthesized and pillared afterwards [183,184]. These pillared zeolites have been used in a variety of reactions to increase yield or decrease deactivation [185,186]. In one study by Mei et al., MTO was investigated on post-synthetically modified mesoporous H-ZSM-5 [187]. They found that introducing mesopores caused an increase in the propylene to ethylene ratio of the effluent, as well as an increase in butylene selectivity. They also found that the mesopores themselves did not contribute to the catalytic activity beyond decreasing diffusion limitations.

Finally, studies on mesoporous silicas could be a bridge to modified mesoporous zeolites. Just like zeolites, these materials can be made siliceously or heteroatoms, such as aluminum or iron, can be incorporated [188–190]. In addition to heteroatom substitution, metal organic complexes can be anchored within the nanometer-sized pores [191–193]. If a metal organic complex that promotes oligomerization is anchored within the mesopores of a mesoporous zeolite, larger species maybe formed in comparison to nickel-exchanged zeolites. Additionally, the larger species would diffuse more rapidly out of the zeolite crystal and not be held up in the micropores.

#### **6.1.4 Identifying Species Produced during Dimethyl Ether Conversion**

In order to further understand dimethyl ether conversion on iron zeolites, it will be necessary to improve product species identification. This can be accomplished by modifying the existing GC used for reactor effluent analysis. The first and easiest alteration would be to add a capillary column between the HP-Plot-Q column and FID. In the GC/MS that the HP-Plot-Q column was installed, a short amount of capillary column connected the split for the MS to the FID. When analysis was performed, a

slight increase in product separation was observed from the GC/MS, which could be attributed to the capillary column.

The second alteration would be to install a valve that switches columns the effluent runs through. Polar columns are best for separating olefins and paraffins, but cannot be used in the presence of polar species, as these species remain adsorbed on the column and alter elution times of other nonpolar species. To work around this, the HP-Plot-Q column would provide the initial separation of species until methanol elutes out of the column at approximately 9.7 minutes. Once methanol has eluted, a valve would switch and send the effluent of the HP-Plot-Q column to a GS-Alumina column like that used for species separation in Chapters 3 and 4. This would then allow better separation and identification of olefins and paraffins that could not be sufficiently separated with the HP-Plot-Q column.

## **6.2 Concluding Remarks**

In this thesis, it has been shown that altering zeolite catalysts by changing heteroatom substitution in the framework (Chapters 3-5), metal cation addition (Chapters 4 and 5), and framework structure (Chapter 5) can influence selectivity of hydrocarbon conversion processes. While aircraft endothermic cooling was investigated for military applications, it could potentially be applied to civilian aircraft in the future. The efficiency of a jet engine is enhanced by increasing the temperature achieved during combustion of the fuel. Currently this is limited to the thermal stability of engine components. Endothermic fuels could be utilized in civilian aircraft to cool engine components, allowing for increased combustion temperatures and leading to increased fuel efficiency. Supported metal carbides have been shown to catalyze reactions currently performed with expensive noble metals, such as platinum

or palladium. Switching to inexpensive metal carbides could result in a reduction in processing costs, which could in turn result in decreased product costs for the end consumer.

Finally, methanol conversion to hydrocarbons represents an alternative method to produce fuels and chemicals. Rather than refining petroleum oil, natural gas, coal, or renewable biomass can be upgraded through methanol to produce fuels and chemicals. Methanol conversion to hydrocarbons represents a process to achieve energy independency and renewable fuels and chemicals production through biomass.

## REFERENCES

- [1] J.H. Gary, G.E. Handwerk, M.J. Kaiser, *Petroleum Refining: Technology and Economics*, 5th ed., CRC Press, Boca Taton, Florida, 2007.
- [2] J. Chen, Y. Gao, S. Xiong, M. Delferro, T.L. Lohr, T.J. Marks, *ACS Catal.* 7 (2017) 5214–5219.
- [3] Y. V. Kissin, V.P. Marin, P.J. Nelson, *J. Polym. Sci. Part A Polym. Chem.* 55 (2017) 3832–3841.
- [4] P. Raffa, D.A.Z. Wever, F. Picchioni, A.A. Broekhuis, *Chem. Rev.* 115 (2015) 8504–8563.
- [5] S. Echaroj, M. Santikunaporn, S. Chavadej, *React. Kinet. Mech. Catal.* 121 (2017) 629–644.
- [6] C. Wang, Y. Li, Y. Han, J. Zhang, R. Wu, G. He, *Polym. Chem.* 8 (2017) 5561–5569.
- [7] G. Jaouen, A. Vessières, S. Top, *Chem. Soc. Rev.* 44 (2015) 8802–8817.
- [8] T. Kawada, B.D. Mookherjee, S.S. Chang, *J. Am. Oil Chem. Soc.* 43 (1965) 237–241.
- [9] D.K.T. Moreira, J.N.R. Ract, A.P.B. Ribeiro, G.A. Macedo, *Food Res. Int.* 99 (2017) 713–719.
- [10] J. Scherzer, *Octane-Enhancing Zeolitic FCC Catalysts: Scientific and Technical Aspects*, Marcel Dekker, Inc., New York, New York, 1990.
- [11] I. Nifant'ev, P. Ivchenko, A. Tavtorkin, A. Vinogradov, A. Vinogradov, *Pure Appl. Chem.* 89 (2017) 1017–1032.
- [12] I. Shimada, R. Imai, Y. Hayasaki, H. Fukunaga, N. Takahashi, T. Takatsuka, *Catalysts* 5 (2015) 703–717.

- [13] P. Hu, Y. Wang, X. Meng, R. Zhang, H. Liu, C. Xu, Z. Liu, *Fuel* 189 (2017) 203–209.
- [14] J.D. Naber, D.L. Siebers, S.S. Di Julio, C.K. Westbrook, *Combust. and Flame* 99 (1994) 192–200.
- [15] D. Seddon, *Petrochemical Economics: Technology Selection in a Carbon Constrained World*, Imperial College Press, London, 2010.
- [16] J. Gao, Y. Zheng, J. Jehng, Y. Tang, I.E. Wachs, S.G. Podkolzin, *Science* (80-.). 348 (2015) 686–690.
- [17] O. V. Sedel'nikova, A.A. Stepanov, V.I. Zaikovskii, L.L. Korobitsyna, A. V. Vosmerikov, *Kinet. Catal.* 58 (2017) 51–57.
- [18] Y. Lai, G. Vesper, *Environ. Prog. Sustain.* 35 (2016) 334–344.
- [19] L. Su, J. Zhuang, H. Wang, Y. Li, W. Shen, Y. Xu, X. Bao, *Catal. Letters* 91 (2003) 155–167.
- [20] H.F. Liu, R.S. Liu, K.Y. Liew, R.E. Johnson, J.H. Lunsford, *J. Am. Chem. Soc.* 106 (1984) 4117–4121.
- [21] B. Ipek, R.F. Lobo, *Chem. Commun.* 52 (2016) 13401–13404.
- [22] P. Tomkins, M. Ranocchiari, J.A. Van Bokhoven, *Acc. Chem. Res.* 50 (2017) 418–425.
- [23] M.J. Wulfers, S. Teketel, B. Ipek, R.F. Lobo, *Chem. Commun.* 51 (2015) 4447–4450.
- [24] M.J. Brown, N.D. Parkyns, *Catal. Today* 8 (1991) 305–335.
- [25] F.J. Keil, *Microporous Mesoporous Mater.* 29 (1999) 49–66.
- [26] M. Stöcker, *Microporous Mesoporous Mater.* 29 (1999) 3–48.
- [27] U. Olsbye, S. Svelle, M. Bjrgen, P. Beato, T.V.W. Janssens, F. Joensen, S. Bordiga, K.P. Lillerud, *Angew. Chemie Int. Ed.* 51 (2012) 5810–5831.
- [28] N. Mosier, C. Wyman, B. Dale, R. Elander, Y.Y. Lee, M. Holtzapple, M. Ladisch, *Bioresour. Technol.* 96 (2005) 673–686.
- [29] M.E. Davis, *Top. Catal.* (2015) 405–409.

- [30] R.E. Patet, M. Koehle, R.F. Lobo, S. Caratzoulas, D.G. Vlachos, *J. Phys. Chem. C* 121 (2017) 13666–13679.
- [31] S. Sun, R. Yang, P. Sun, C. Ma, J. Chen, *Energy* 135 (2017) 577–584.
- [32] B. Lu, J. Li, G. Lv, Y. Qi, Y. Wang, X. Hou, Y. Yang, *J. Clean. Prod.* 162 (2017) 330–335.
- [33] T. Ogoshi, Y. Miyawaki, *J. Am. Oil Chem. Soc.* 62 (1985) 331–335.
- [34] M. Fangrui, M. Hanna, *Bioresour. Technol.* 70 (1999) 1–15.
- [35] J. Kopyscinski, T.J. Schildhauer, S.M.A. Biollaz, *Fuel* 89 (2010) 1763–1783.
- [36] K. Göransson, U. Söderlind, J. He, W. Zhang, *Renew. Sustain. Energy Rev.* 15 (2011) 482–492.
- [37] M.E. Dry, *J. Chem. Technol. Biotechnol.* 77 (2002) 43–50.
- [38] M. Hook, K. Aleklett, *Int. J. Energy Res.* 34 (2010) 848–864.
- [39] D.A. Wood, C. Nwaoha, B.F. Towler, *J. Nat. Gas Sci. Eng.* 9 (2012) 196–208.
- [40] N.R. Deprez, M.S. Sanford, *J. Am. Chem. Soc.* 131 (2009) 11234–11241.
- [41] J.A. Loiland, M.J. Wulfers, N.S. Marinkovic, R.F. Lobo, *Catal. Sci. Technol.* 6 (2016) 5267–5279.
- [42] C. Baerlocher, L.B. McCusker, D.H. Olson, *Atlas of Zeolite Framework Types*, 6th ed., Elsevier, Amsterdam, 2007.
- [43] S. Kulprathipanja, ed., *Zeolites in Industrial Separation and Catalysis*, Wiley-WCH Verlag GmbH & Co. KGaA, Weinheim, 2010.
- [44] J. Perez-Pariente, J.A. Martens, P.A. Jacobs, *Zeolites* 8 (1988) 46–53.
- [45] C. Liu, W. Gu, D. Kong, H. Guo, *Microporous Mesoporous Mater.* 183 (2014) 30–36.
- [46] G.T. Kerr, *J. Phys. Chem.* 70 (1966) 1047–1050.
- [47] U. Barth-Wirsching, H. Holler, *Eur. J. Mineral.* 1 (1989) 489–506.
- [48] L.B. Young, S.A. Butter, W.W. Kaeding, *J. Catal.* 76 (1982) 418–432.

- [49] A.J. Jones, R.T. Carr, S.I. Zones, E. Iglesia, *J. Catal.* 312 (2014) 58–68.
- [50] L. Ma, Y. Cheng, G. Cavataio, R.W. McCabe, L. Fu, J. Li, *Chem. Eng. J.* 225 (2013) 323–330.
- [51] A. Finiels, F. Fajula, V. Hulea, *Catal. Sci. Technol.* 4 (2014) 2412–2426.
- [52] B.M. Murphy, M.P. Letterio, B. Xu, *J. Catal.* 339 (2016) 21–30.
- [53] J. Wei, Q. Ge, R. Yao, Z. Wen, C. Fang, L. Guo, H. Xu, J. Sun, *Nat. Commun.* 8 (2017) 15174.
- [54] G.A. Olah, A. Goepfert, G.K.S. Prakash, 74 (2009) 487–498.
- [55] W. Luc, J. Rosen, F. Jiao, *Catal. Today* 288 (2017) 79–84.
- [56] C. Costentin, M. Robert, J. Savéant, *Chem. Soc. Rev.* 42 (2013) 2423–2436.
- [57] V. Smil, *Enriching the Earth: Fritz Haber, Carl Bosch, and the Transformation of World Food Production*, MIT Press, Cambridge, Massachusetts, 2000.
- [58] R. Lan, J.T.S. Irvine, S. Tao, *Sci. Rep.* 3 (2013) 1–7.
- [59] R. Jenkins, R. Snyder, *Introduction to X-Ray Powder Diffractometry*, John Wiley and Sons, New York, New York, 2012.
- [60] J. Jiao, W. Wang, B. Sulikowski, J. Weitkamp, M. Hunger, *Microporous Mesoporous Mater.* 90 (2006) 246–250.
- [61] K.S.W. Sing, D.H. Everett, R.A.W. Haul, L. Moscou, R.A. Pierotti, J. Rouquerol, T. Siemieniowska, *Pure Appl. Chem.* 57 (1985) 603–619.
- [62] M. Thommes, K. Kaneko, A. V. Neimark, J.P. Olivier, F. Rodriguez-Reinoso, J. Rouquerol, K.S.W. Sing, *Pure Appl. Chem.* 87 (2015) 1051–1069.
- [63] H. Lander, A.C. Nixon, *J. Aircr.* 8 (1971) 200–207.
- [64] D.G. Norton, R.J. Perry, J. Osaheni, P. Pastecki, P. Glaser, A.B. Mhadeshwar, *Systems and Methods for Using an Endothermic Fuel with a High Heat Sink Capacity for Aircraft Waste Heat Rejection*, US 2012/0305712 A1, 2012.
- [65] J.A. Widegren, T.J. Bruno, *Energy and Fuels* 23 (2009) 5523–5528.
- [66] H.S. Chung, C.S.H. Chen, R.A. Kremer, J.R. Boulton, G.W. Burdette, *Energy and Fuels* 13 (1999) 641–649.

- [67] N. Gascoin, G. Abraham, P. Gillard, *J. Anal. Appl. Pyrolysis* 89 (2010) 294–306.
- [68] J. Kim, D.H. Hyeon, S.H. Park, B. Chun, B.H. Jeong, J.S. Han, S.H. Kim, *Catal. Today* 232 (2014) 63–68.
- [69] M. Stöcker, *Microporous Mesoporous Mater.* 82 (2005) 257–292.
- [70] A. Corma, *Chem. Rev.* 95 (1995) 559–614.
- [71] Z. Dardas, M.G. Suer, Y.H. Ma, W.R. Moser, *J. Catal.* 159 (1996) 204–211.
- [72] X. Xian, G. Liu, X. Zhang, L. Wang, Z. Mi, *Chem. Eng. Sci.* 65 (2010) 5588–5604.
- [73] J. Luo, R.J. Gorte, *Catal. Letters* 143 (2013) 313–316.
- [74] J. Luo, B. V. Bhaskar, Y.H. Yeh, R.J. Gorte, *Appl. Catal. A Gen.* 478 (2014) 228–233.
- [75] W. Ning, P. Yu, Z. Jin, *Proc. Inst. Mech. Eng. Part G J. Aerosp. Eng.* 227 (2012) 1780–1794.
- [76] W.O. Haag, R.M. Dessau, *Duality of Mechanism for Acid-Catalyzed Paraffin Cracking*, Princeton, NJ, 1985.
- [77] R. Gounder, E. Iglesia, *J. Am. Chem. Soc.* 131 (2009) 1958–1971.
- [78] S.M. Babitz, B. a. Williams, J.T. Miller, R.Q. Snurr, W.O. Haag, H.H. Kung, *Appl. Catal. A Gen.* 179 (1999) 71–86.
- [79] T.F. Narbeshuber, H. Vinek, J.A. Lercher, *J. Catal.* 157 (1995) 388–395.
- [80] A. Janda, A.T. Bell, *J. Am. Chem. Soc.* 135 (2013) 19193–19207.
- [81] A. Bhan, R. Gounder, J. Macht, E. Iglesia, *J. Catal.* 253 (2008) 221–224.
- [82] B. Xu, C. Sievers, S.B. Hong, R. Prins, J.A. van Bokhoven, *J. Catal.* 244 (2006) 163–168.
- [83] M. Derewinski, F. Fajula, *Appl. Catal. A Gen.* 108 (1994) 53–61.
- [84] V.B. Kazansky, *Catal. Today* 51 (1999) 419–434.
- [85] A. Corma, P.J. Miguel, A. V. Orchilles, *J. Catal.* 145 (1994) 171–180.

- [86] T.F. Narbeshuber, A. Brait, K. Seshan, J.A. Lercher, *J. Catal.* 172 (1997) 127–136.
- [87] J.H. Yun, R.F. Lobo, *J. Catal.* 312 (2014) 263–270.
- [88] J.H. Yun, R.F. Lobo, *Catal. Sci. Technol.* 5 (2015) 264–273.
- [89] J. Kim, S.H. Park, B.H. Chun, B.H. Jeong, J.S. Han, S.H. Kim, *Catal. Today* 185 (2012) 47–53.
- [90] Y. Wang, X. Xian, X. Hou, X. Zhang, L. Wang, G. Liu, *J. Anal. Appl. Pyrolysis* 113 (2015) 133–136.
- [91] A. Farshi, H.R. Abri, *Pet. Sci. Technol.* 30 (2012) 1285–1295.
- [92] E. V. Anslyn, D.A. Dougherty, *Modern Physical Organic Chemistry*, University Science Books, 2006.
- [93] D.J. Rosenthal, A.S. Teja, *AIChE J.* 35 (1989) 1829–1834.
- [94] J.C. Groen, J.A. Moulijn, J. Pérez-Ramírez, *Ind. Eng. Chem. Res.* 46 (2007) 4193–4201.
- [95] R.J. Quann, L.A. Green, S.A. Tabak, F.J. Krambeck, *Ind. Eng. Chem. Res.* 27 (1988) 565–570.
- [96] B. Chiche, E. Sauvage, F. Di Renzo, I.I. Ivanova, F. Fajula, *J. Mol. Catal. A Chem.* 134 (1998) 145–157.
- [97] C. Bertrand-Drira, X. Cheng, T. Cacciaguerra, P. Trens, G. Melinte, O. Ersen, D. Minoux, A. Finiels, F. Fajula, C. Gerardin, *Microporous Mesoporous Mater.* 213 (2015) 142–149.
- [98] E.P. Schreiner, S. Teketel, R.F. Lobo, *New J. Chem.* 40 (2016) 4245–4251.
- [99] D.E. Resasco, *Encycl. Catal.* (2002).
- [100] J.J.H.B. Sattler, J. Ruiz-Martinez, E. Santillan-Jimenez, B.M. Weckhuysen, *Chem. Rev.* 114 (2014) 10613–10653.
- [101] H. Lieske, A. Sarkany, J. Volter, *Appl. Catal.* 30 (1987) 69–80.
- [102] J.M. Hill, R.D. Cortright, J.A. Dumesic, *Appl. Catal. A Gen.* 168 (1998) 9–21.
- [103] R.D. Cortright, J.M. Hill, J.A. Dumesic, *Catal. Today* 55 (2000) 213–223.

- [104] B.M. Nagaraja, C.H. Shin, K.D. Jung, *Appl. Catal. A Gen.* 467 (2013) 211–223.
- [105] J. Wu, Z. Peng, A.T. Bell, *J. Catal.* 311 (2014) 161–168.
- [106] F.E. Frey, W.F. Huppke, *Ind. Eng. Chem. Res.* 25 (1933) 54–59.
- [107] Z. Liu, X. He, R. Cheng, M.S. Eisen, M. Terano, S.L. Scott, B. Liu, *Adv. Chem. Eng.* 44 (2014) 127–191.
- [108] M. Volpe, G. Tonetto, H. de Lasa, *Appl. Catal. A Gen.* 272 (2004) 69–78.
- [109] M. Saito, S. Watanabe, I. Takahara, M. Inaba, K. Murata, *Catal. Letters* 89 (2003) 213–217.
- [110] M.E. Harlin, L.B. Backman, A.O.I. Krause, O.J.T. Jylha, O. Jylhä, *J. Catal.* 183 (1999) 300–313.
- [111] J. Ogonowski, E. Skrzyńska, *Catal. Letters* 111 (2006) 79–85.
- [112] K. Nakagawa, M. Okamura, N. Ikenaga, T. Suzuki, T. Kobayashi, *Chem. Commun.* 3 (1998) 1025–1026.
- [113] R. B. Levy and M. Boudart, *Science* (80-. ). 181 (1973) 547–549.
- [114] A.L. Stottlemeyer, P. Liu, J.G. Chen, *J. Chem. Phys.* 133 (2010) 104702.
- [115] B. Frank, T.P. Cotter, M.E. Schuster, R. Schlögl, A. Trunschke, *Chem. - A Eur. J.* 19 (2013) 16938–16945.
- [116] A. Mehdad, R.E. Jentoft, F.C. Jentoft, *J. Catal.* 347 (2017) 89–101.
- [117] F. Solymosi, J. Cserényi, A. Szöke, T. Bánsági, A. Oszkó, *J. Catal.* 165 (1997) 150–161.
- [118] A. Széchenyi, F. Solymosi, *Appl. Catal. A Gen.* 306 (2006) 149–158.
- [119] H. Ren, W. Yu, M. Saliccioli, Y. Chen, Y. Huang, K. Xiong, D.G. Vlachos, J.G. Chen, *ChemSusChem* 6 (2013) 798–801.
- [120] Z.R. Ismagilov, E. V. Matus, L.T. Tsikoza, *Energy Environ. Sci.* 1 (2008) 526–541.
- [121] N. Kosinov, F.J.A.G. Coumans, E.A. Uslamin, A.S.G. Wijkema, B. Mezari, E.J.M. Hensen, *ACS Catal.* 7 (2017) 520–529.

- [122] C. Karakaya, H. Zhu, R.J. Kee, *Chem. Eng. Sci.* 123 (2015) 474–486.
- [123] K.S. Wong, J.W. Thybaut, E. Tangstad, M.W. Stocker, G.B. Marin, *Microporous Mesoporous Mater.* 164 (2012) 302–312.
- [124] E. Unneberg, S. Kolboe, *Appl. Catal. A, Gen.* 124 (1995) 345–354.
- [125] M.G. Howden, *Zeolites* 5 (1985) 334–338.
- [126] M.B. Sayed, A. Auroux, J.C. Vedrine, *J. Catal.* 116 (1989) 1–10.
- [127] F. Testa, R. Chiappetta, F. Crea, R. Aiello, A. Fonseca, J.C. Bertrand, G. Demortier, J.L. Guth, L. Delmotte, J.B. Nagy, *J. Porous Mater.* 14 (2007) 191–204.
- [128] C.D. Chang, C. Chu, J.L. Schlenker, *Geol. Soc. Spec. Publ.* 7 (2002) 75–82.
- [129] W. Ding, S. Li, G.D. Meitzner, E. Iglesia, *J. Phys. Chem. B* 105 (2001) 506–513.
- [130] F. Solymosi, R. Barthos, *Catal. Letters* 101 (2005) 235–239.
- [131] H.J. Guzmán, W. Xu, D. Stacchiola, G. Vitale, C.E. Scott, J.A. Rodríguez, P. Pereira-Almao, *Can. J. Chem.* 91 (2013) 573–582.
- [132] T. Xiao, A.P.E. York, K.S. Coleman, J.B. Claridge, J. Sloan, J. Charnock, M.L.H. Green, *J. Mater. Chem.* 11 (2001) 3094–3098.
- [133] T. Xiao, H. Wang, J. Da, K. Coleman, M.L.H. Green, *J. Catal.* 211 (2002) 183–191.
- [134] A.W. Ritchie, R.D. Hawthorn, A.C. Nixon, *Ind. Eng. Chem. Prod. Res. Dev.* 4 (1965) 129–136.
- [135] O.F. Gorriz, V.C. Corberin, J.L.G. Fierro, *Ind. Eng. Chem. Res.* 31 (1992) 2670–2674.
- [136] J. Gao, Y. Zheng, G.B. Fitzgerald, J. de Joannis, Y. Tang, I.E. Wachs, S.G. Podkolzin, *J. Phys. Chem. C* 118 (2014) 4670–4679.
- [137] H. Jobic, W. Schmidt, C.B. Krause, J. Kärger, *Microporous Mesoporous Mater.* 90 (2006) 299–306.
- [138] Y.H. Yeh, S. Zhu, P. Staiber, R.F. Lobo, R.J. Gorte, *Ind. Eng. Chem. Res.* 55 (2016) 3930–3938.

- [139] S. Walspurger, G.K.S. Prakash, G.A. Olah, *Appl. Catal. A Gen.* 336 (2008) 48–53.
- [140] J. Bercaw, P. Diaconescu, R. Grubbs, R. Kay, S. Kitching, J. Labinger, Z. Li, P. Mehrkhodavandi, G. Morris, G. Sunley, P. Vagner, *J. Org. Chem.* 71 (2006) 8907–8917.
- [141] G.J. Hutchings, R. Hunter, *Catal. Today* 6 (1990) 279–306.
- [142] D. Chen, K. Moljord, A. Holmen, *Microporous Mesoporous Mater.* 164 (2012) 239–250.
- [143] C.D. Chang, *Catal. Today* 13 (1992) 103–111.
- [144] P. Tian, Y. Wei, M. Ye, Z. Liu, *ACS Catal.* 5 (2015) 1922–1938.
- [145] C.D. Chang, J.C.W. Kuo, W.H. Lang, S.M. Jacob, J.J. Wise, A.J. Silvestri, *Ind. Eng. Chem. Process Des. Dev.* 17 (1978) 255–260.
- [146] M.J. van Niekerk, J.C.Q. Fletcher, C.T. O'Connor, *Appl. Catal. A Gen.* 138 (1996) 135–145.
- [147] S. Ilias, A. Bhan, *ACS Catal.* 3 (2013) 18–31.
- [148] J.F. Haw, W. Song, D.M. Marcus, J.B. Nicholas, *Acc. Chem. Res.* 36 (2003) 317–326.
- [149] K. Nishi, T. Shimizu, H. Yoshida, A. Satsuma, T. Hattori, *Appl. Catal. A Gen.* 166 (1998) 335–341.
- [150] S. Svelle, U. Olsbye, F. Joensen, M. Bjørgen, *J. Phys. Chem. C* 111 (2007) 17981–17984.
- [151] Q. Wang, Z.M. Cui, C.Y. Cao, W.G. Song, *J. Phys. Chem. C* 115 (2011) 24987–24992.
- [152] S. Teketel, S. Svelle, K. Lillerud, U. Olsbye, *ChemCatChem* 1 (2009) 78–81.
- [153] J.H. Ahn, B. Temel, E. Iglesia, *Angew. Chemie Int. Ed.* 48 (2009) 3814–3816.
- [154] N. Hazari, E. Iglesia, J.A. Labinger, D.A. Simonetti, *Acc. Chem. Res.* 45 (2012) 653–662.
- [155] Y. Jin, S. Asaoka, S. Zhang, P. Li, S. Zhao, *Fuel Process. Technol.* 115 (2013) 34–41.

- [156] T. Taniguchi, K. Yoneta, S. Nakaoka, Y. Nakasaka, T. Yokoi, T. Tago, T. Masuda, *Catal. Letters* 146 (2016) 442–451.
- [157] S. Tobisch, T. Ziegler, *Organometallics* 22 (2003) 5392–5405.
- [158] A.M. Al-Jarallah, J.A. Anabtawi, M.A.B. Siddiqui, A.M. Aitani, *Catal. Today* 14 (1992) 1–124.
- [159] K. Ziegler, *Angew. Chemie* 64 (1952) 323–329.
- [160] A. Forestière, H. Olivier-Bourbigou, L. Saussine, *Oil Gas Sci. Technol. - Rev. IFP* 64 (2009) 649–667.
- [161] W. Keim, *Angew. Chemie Int. Ed.* 52 (2013) 12492–12496.
- [162] O. Novaro, S. Chow, P. Magnouat, *J. Catal.* 41 (1976) 91–100.
- [163] H. Makio, T. Fujita, *Acc. Chem. Res.* 42 (2009) 1532–1544.
- [164] J.R. Sohn, H.W. Kim, M.Y. Park, E.H. Park, J.T. Kim, S.E. Park, *Appl. Catal. A, Gen.* 128 (1995) 127–141.
- [165] Q. Zhang, M. Kantcheva, I.G. Dalla Lana, *Ind. Eng. Chem. Res.* 36 (1997) 3433–3438.
- [166] M. Lallemand, A. Finiels, F. Fajula, V. Hulea, *J. Phys. Chem. C* 113 (2009) 20360–20364.
- [167] J. Heveling, A. van der Beek, M. de Pender, *Appl. Catal.* 42 (1988) 325–336.
- [168] A. Raj, S. Sivasanker, K. Lazar, *J. Catal.* 147 (1994) 207–213.
- [169] M.W. Erichsen, S. Svelle, U. Olsbye, *Catal. Today* 215 (2013) 216–223.
- [170] A.T. Aguayo, A.G. Gayubo, R. Vivanco, M. Olazar, J. Bilbao, *Appl. Catal. A Gen.* 283 (2005) 197–207.
- [171] H. Muroyama, Y. Tsuda, T. Asakoshi, H. Masitah, T. Okanishi, T. Matsui, K. Eguchi, *J. Catal.* 343 (2016) 178–184.
- [172] H. Huang, X. Tang, M. Haas, *J. Eng. Gas Turbines Power* 134 (2012) 101502.
- [173] F.K. Habib, C. Diner, M. Stryker, N. Semagina, M.R. Gray, (2013).
- [174] R. Gounder, E. Iglesia, *Angew. Chemie Int. Ed.* 49 (2010) 808–811.

- [175] J.R. Di Iorio, R. Gounder, *Chem. Mater.* 28 (2016) 2236–2247.
- [176] S. Boullosa-Eiras, R. Lodeng, H. Bergem, M. Stocker, L. Hannevold, E.A. Blekkan, *Catal. Today* 223 (2014) 44–53.
- [177] W.S. Lee, Z. Wang, W. Zheng, D.G. Vlachos, A. Bhan, *Catal. Sci. Technol.* 4 (2014) 2340–2352.
- [178] J.S. Lee, M. Boudart, *Appl. Catal.* 19 (1985) 207–210.
- [179] A. Alsalmeh, N. Alzaqri, A. Alsaleh, M.R.H. Siddiqui, A. Alotaibi, E.F. Kozhevnikova, I. V. Kozhevnikov, *Appl. Catal. B Environ.* 182 (2016) 102–108.
- [180] B. Baubet, E. Devers, A. Hugon, E. Leclerc, P. Afanasiev, *Appl. Catal. A Gen.* 487 (2014) 72–81.
- [181] M.J. Wulfers, R.F. Lobo, *Appl. Catal. A Gen.* 505 (2015) 394–401.
- [182] J. Pérez-Ramírez, C.H. Christensen, K. Egeblad, C.H. Christensen, J.C. Groen, *Chem. Soc. Rev.* 37 (2008) 2530–2542.
- [183] K. Na, C. Jo, J. Kim, K. Cho, J. Jung, Y. Seo, R.J. Messinger, B.F. Chmelka, R. Ryoo, *Science* (80-. ). 333 (2011) 328–332.
- [184] J. Wang, J.C. Groen, W. Yue, W. Zhou, M.-O. Coppens, *J. Mater. Chem.* 18 (2008) 468.
- [185] L. Ren, Q. Guo, P. Kumar, M. Orazov, D. Xu, S.M. Alhassan, K.A. Mkhoyan, M.E. Davis, M. Tsapatsis, *Angew. Chemie Int. Ed.* 54 (2015) 10848–10851.
- [186] Y. Wu, L. Emdadi, Z. Wang, W. Fan, D. Liu, *Appl. Catal. A Gen.* 470 (2014) 344–354.
- [187] C. Mei, P. Wen, Z. Liu, H. Liu, Y. Wang, W. Yang, Z. Xie, W. Hua, Z. Gao, *J. Catal.* 258 (2008) 243–249.
- [188] M. Kruk, M. Jaroniec, C.H. Ko, R. Ryoo, *Chem. Mater.* 12 (2000) 1961–1968.
- [189] Á. Reyes-Carmona, M.D. Soriano, J.M. López Nieto, D.J. Jones, J. Jiménez-Jiménez, A. Jiménez-López, E. Rodríguez-Castellón, *Catal. Today* 210 (2013) 117–123.
- [190] I. Jiménez-Morales, J. Santamaría-González, P. Maireles-Torres, A. Jiménez-López, *Appl. Catal. B Environ.* 105 (2011) 199–205.

- [191] E. Rossetto, B.P. Nicola, R.F. de Souza, S.B.C. Pergher, K. Bernardo-Gusmao, *Appl. Catal. A Gen.* 502 (2015) 221–229.
- [192] L. Laskowski, M. Laskowska, M. Balanda, M. Fitta, J. Kwiatkowska, K. Dzilinski, A. Karczmarzka, *Microporous Mesoporous Mater.* 200 (2014) 253–259.
- [193] F. Schweyer-Tihay, P. Braunstein, C. Estournès, J.L. Guille, B. Lebeau, J.L. Paillaud, M. Richard-Plouet, J. Rosé, *Chem. Mater.* 15 (2003) 57–62.

## Appendix A

### DETAILED PRODUCT SELECTIVITY FOR *n*-PENTANE CONVERSION ON H-[Al]ZSM-5

Table A.1: Product carbon selectivity at 15 min time on stream from high pressure conversion of *n*-pentane on H-[Al]ZSM-5. Reaction conditions: T = 633 – 723 K, P = 40 bar, and WHSV = 1120 g<sub>C5</sub>g<sub>cat</sub><sup>-1</sup>h<sup>-1</sup>.

Pressure	40 bar		
	Temperature	633 K	673 K
Conversion	4.29	12.20	29.57
methane	0.05	0.05	0.13
ethane	0.28	0.36	0.86
ethene	0.21	0.30	0.45
propane	23.47	29.18	35.67
propene	1.21	1.38	1.71
<i>iso</i> -butane	15.87	15.55	14.25
<i>n</i> -butane	26.04	27.90	26.25
<i>trans</i> -2-butene	0.65	0.69	0.71
1-butene	0.33	0.38	0.45
<i>iso</i> -butene	1.72	1.57	1.46
<i>cis</i> -2-butene	1.38	0.93	0.77
pentenes	5.22	3.97	3.19
hexanes	5.97	10.93	7.10
hexenes	11.70	1.97	1.72
heptanes	2.24	1.67	1.17
heptenes	3.71	2.75	2.06
Other	0.00	0.39	2.05
P/O Ratio	2.83	6.14	6.83



**Appendix B**  
**X-RAY DIFFRACTION PATTERNS AND SEM IMAGES OF**  
**BOROSILICATES**

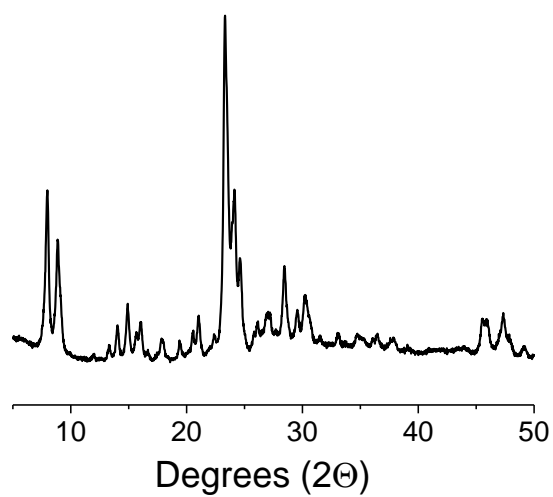


Figure B.1: X-ray diffraction pattern of [B]ZSM-5 (F-1) with silicon metal added

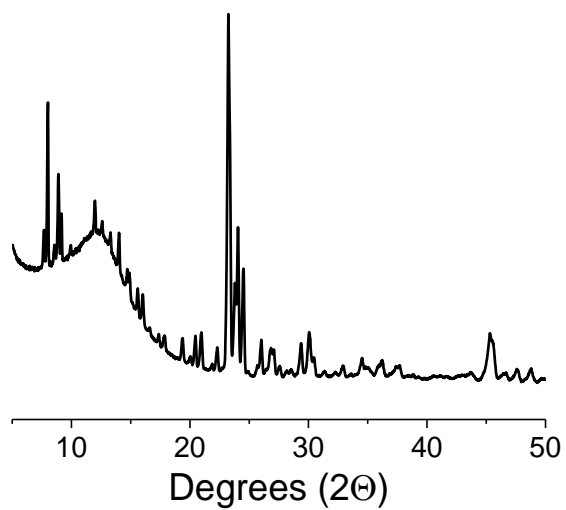


Figure B.2: X-ray diffraction pattern of [B]ZSM-5 (F-2)

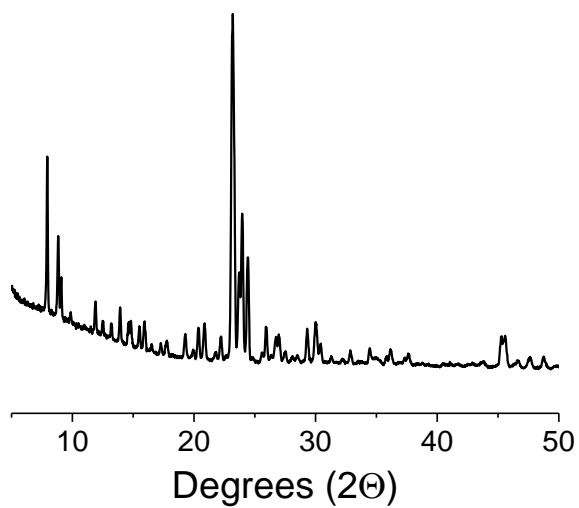


Figure B.3: X-ray diffraction pattern of [B]ZSM-5 (OH-1)

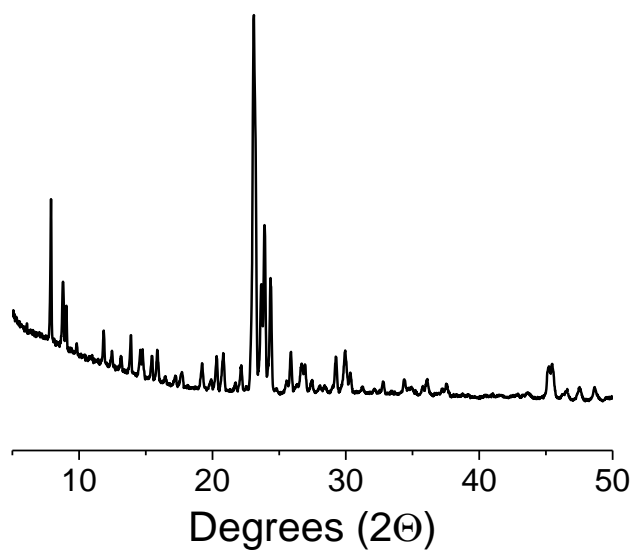


Figure B.4: X-ray diffraction pattern of [B]ZSM-5 (OH-2)

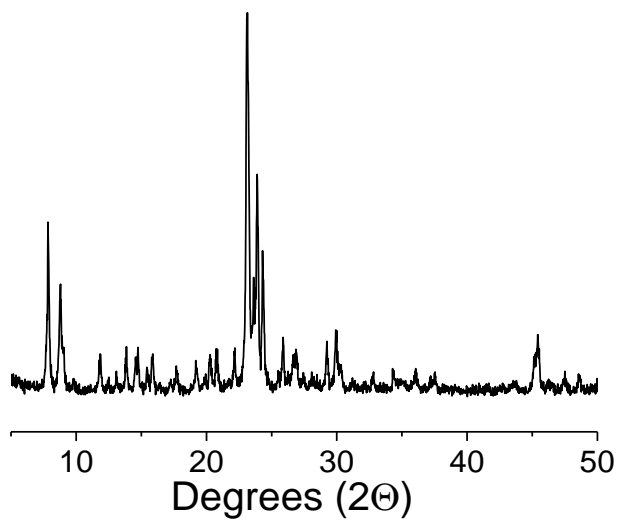


Figure B.5: X-ray diffraction pattern of Silicalite-1 (MFI Topology)

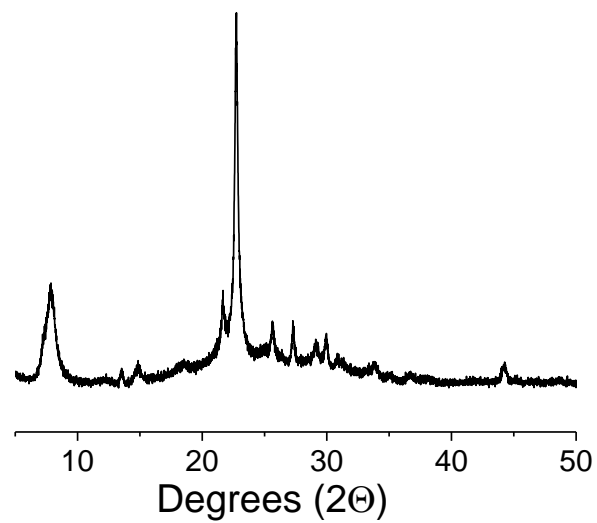


Figure B.6: X-ray diffraction pattern of [B]Beta



Figure B.7: SEM image of [B]ZSM-5 (F-1)

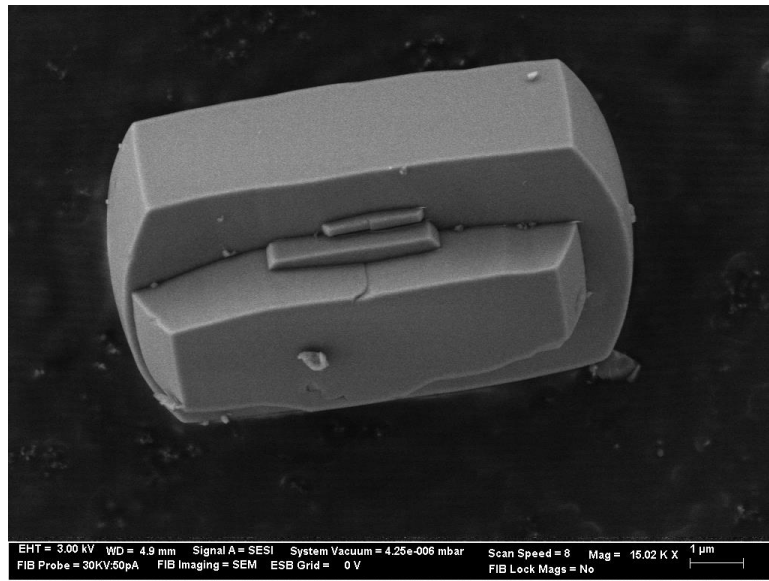


Figure B.8: SEM image of [B]ZSM-5 (F-2)

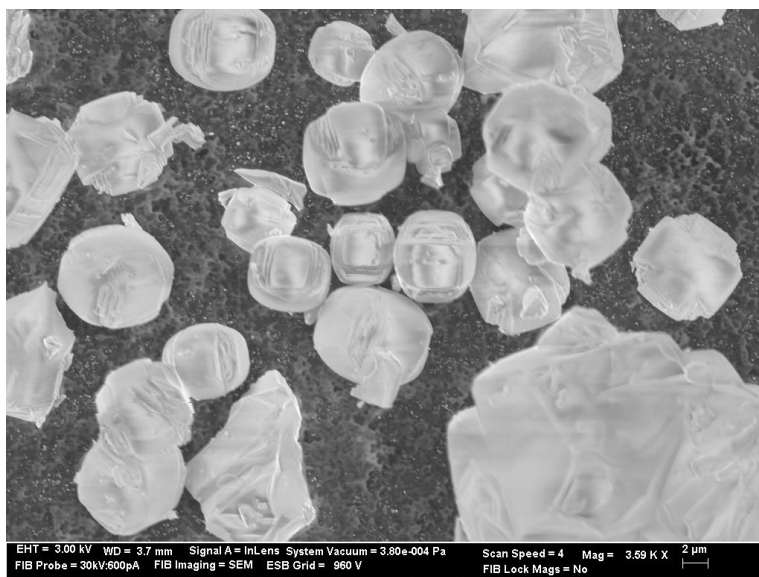


Figure B.9: SEM image of [B]ZSM-5 (OH-1)

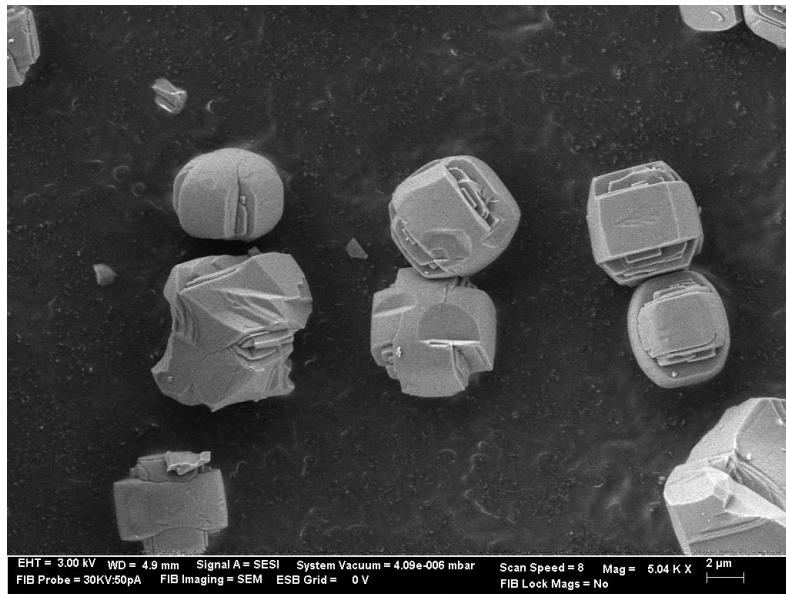


Figure B.10: SEM image of [B]ZSM-5 (OH-2)

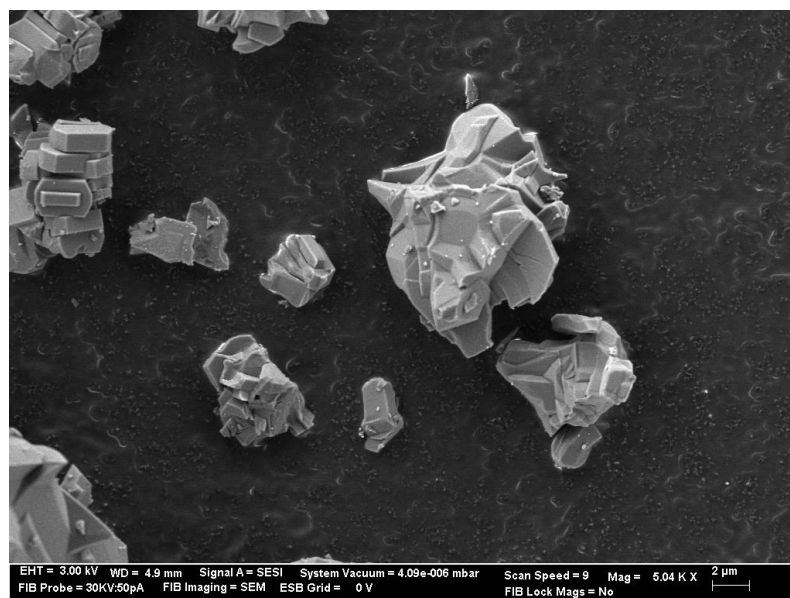


Figure B.11: SEM image of Silicalite-1

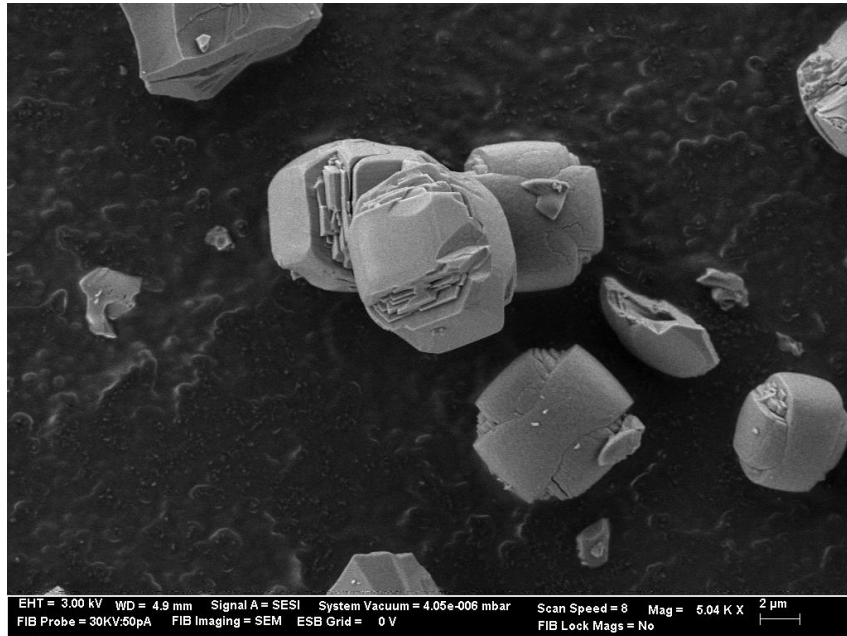


Figure B.12: SEM image of deboronated [B]ZSM-5 (OH-1)

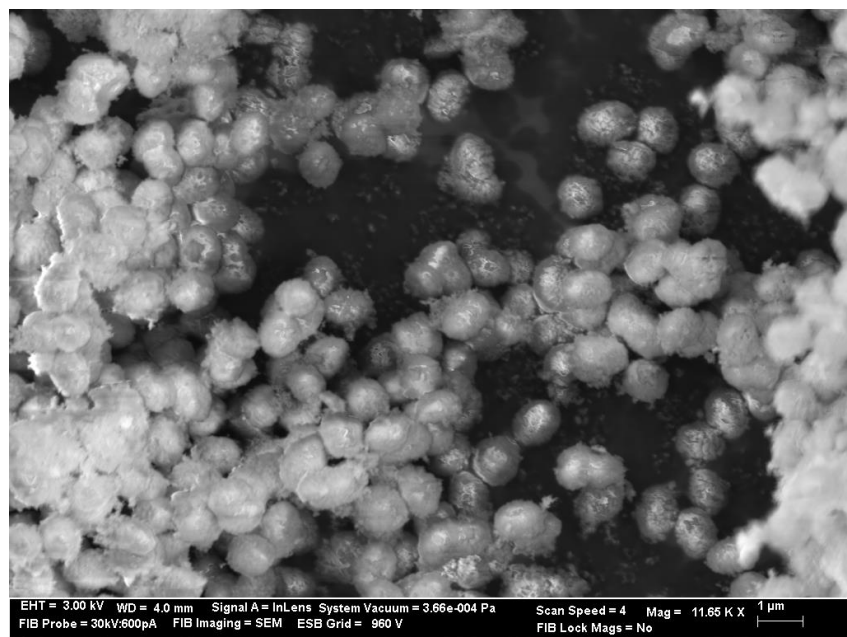


Figure B.13: SEM image of [B]Beta

## Appendix C

### GAS CHROMATOGRAPHY / MASS SPECTROMETRY OF DME CONVERSION ON H-[FE]BETA

Table C.1: Carbon selectivity of species identified via GC/MS from DME conversion on H-[Fe]Beta. Reaction conditions: T = 593 K, P = 1 atm,  $P_{\text{DME}} = 0.14$  atm,  $F_{\text{N}_2} = 60$  mL/min, and  $\text{WHSV} =$  and  $5.7 \text{ g}_{\text{DME}}\text{g}_{\text{cat}}^{-1}\text{h}^{-1}$

	Compound	Carbon Selectivity (%)
a	Methane	1.7
b	Ethene	0.6
c	Propene	4.5
d	Dimethyl ether	---
e	Methanol	---
f	<i>i</i> -butane	---
g	<i>i</i> -butene	49.3
h	<i>n</i> -butane	---
i	2-butene	3.0
j	2-methyl-1-butene	0.3
k	2-methylbutane	3.0
l	2-pentene	3.6
m	2-pentene	2.1
n	2-methyl-2-butene	13.3
o	2,3-dimethyl-1-butene	1.4
p	2,3-dimethylbutane	0.2
q	2-methyl-1-pentene	0.6
r	2-methyl-2-pentene	2.3
s	3-hexene	1.5
t	3-methyl-2-pentene	1.3
u	2,3-dimethyl-2-butene	2.5
v	triptene	4.9

q	Other C <sub>7=</sub>	3.6
x	<i>o,p</i> -Xylene	0.3

---

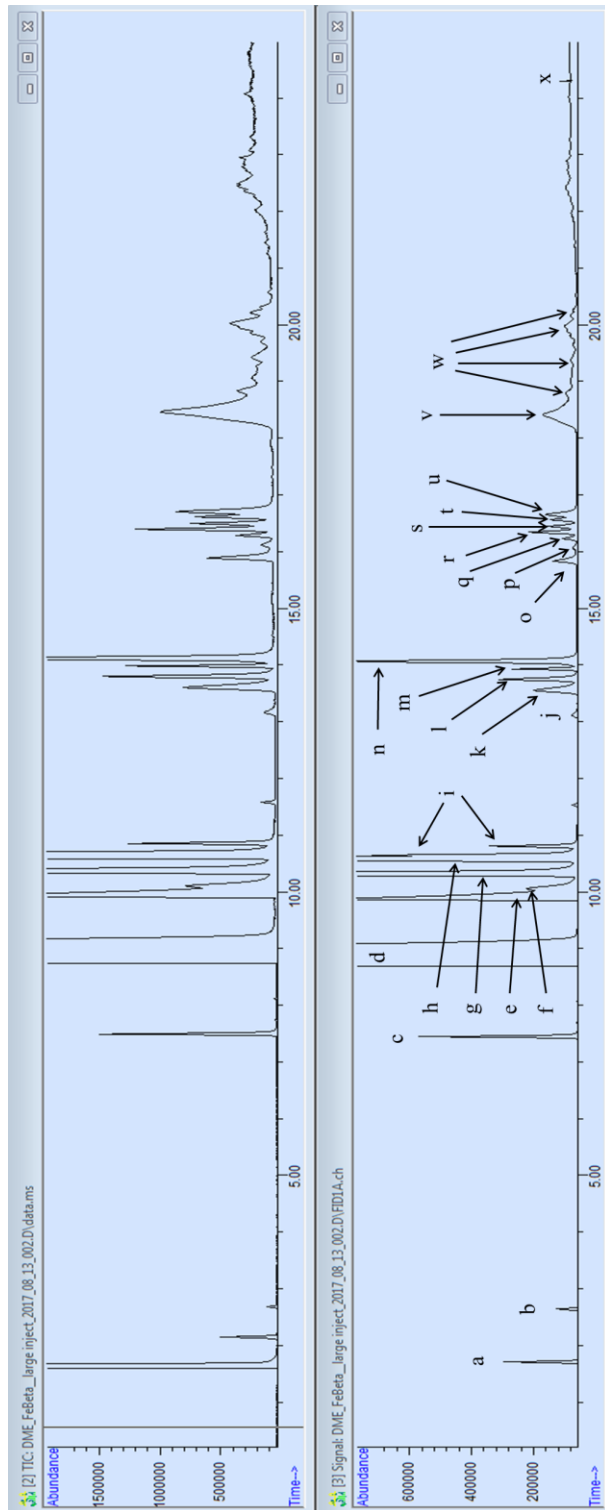


Figure C.1: GC/MS data with peak labeled matching Table C.1

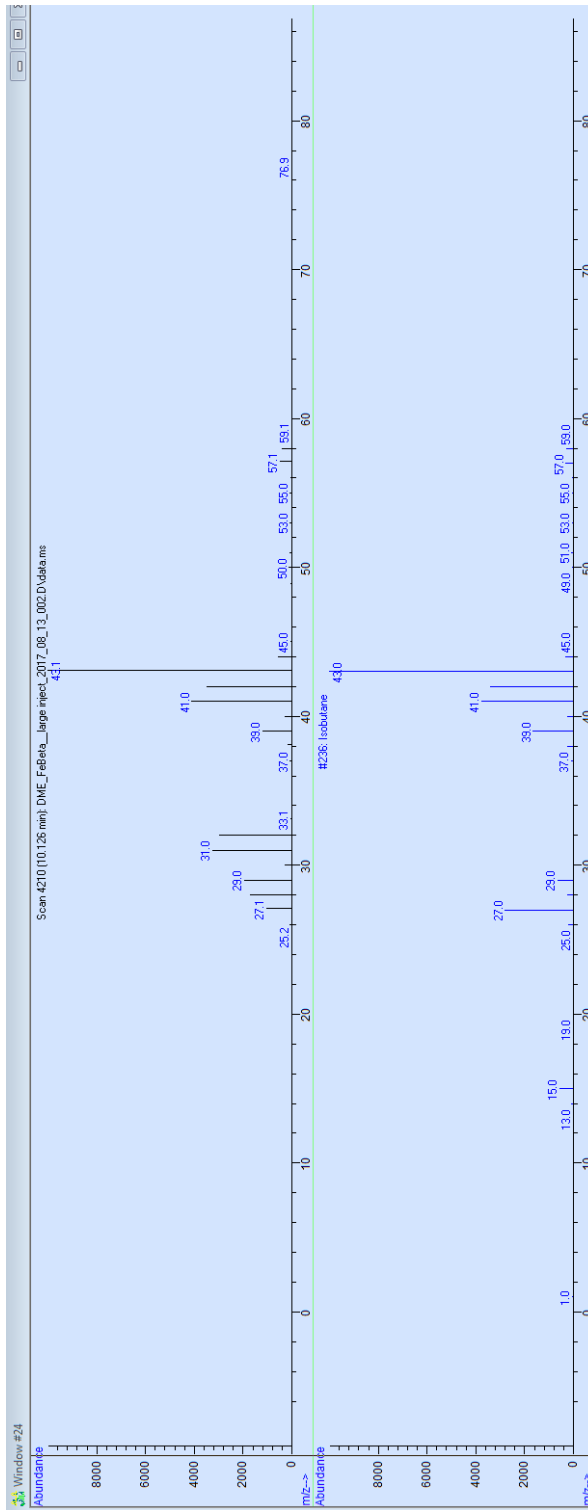


Figure C.2: Mass spectrometer fragmentation pattern for isobutane peak

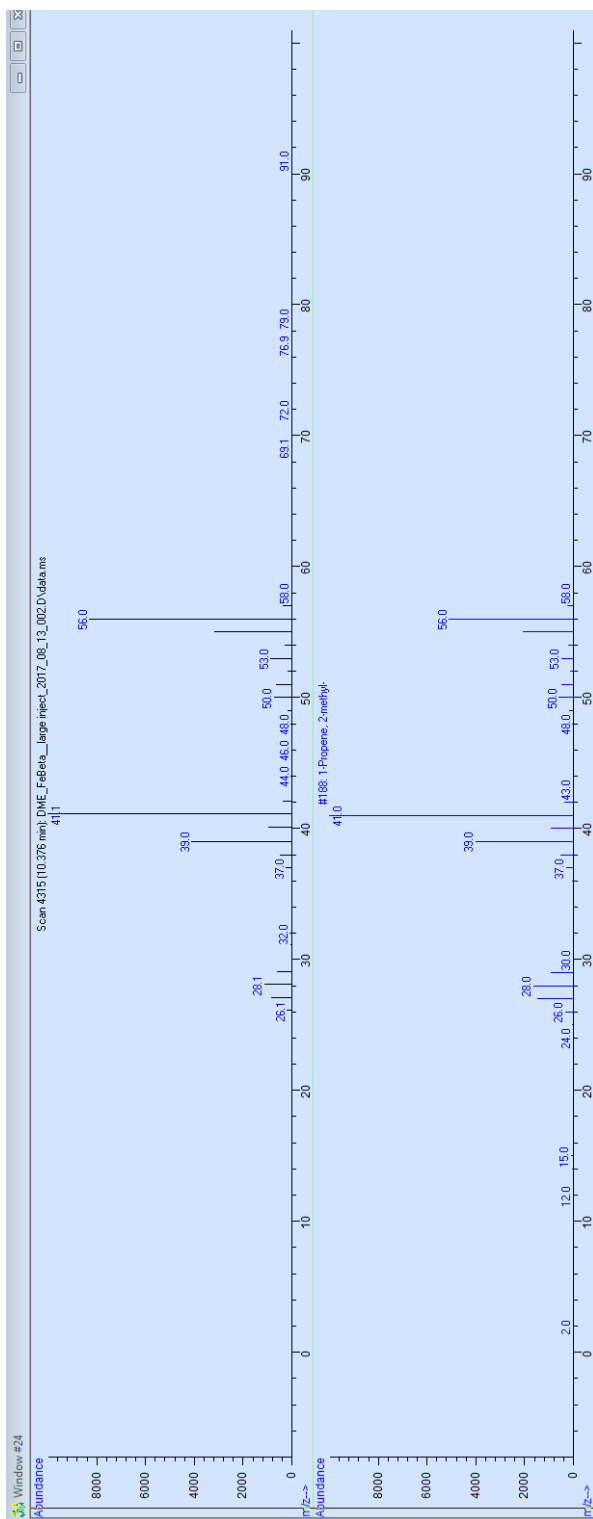


Figure C.3: Mass spectrometer fragmentation pattern for isobutene peak

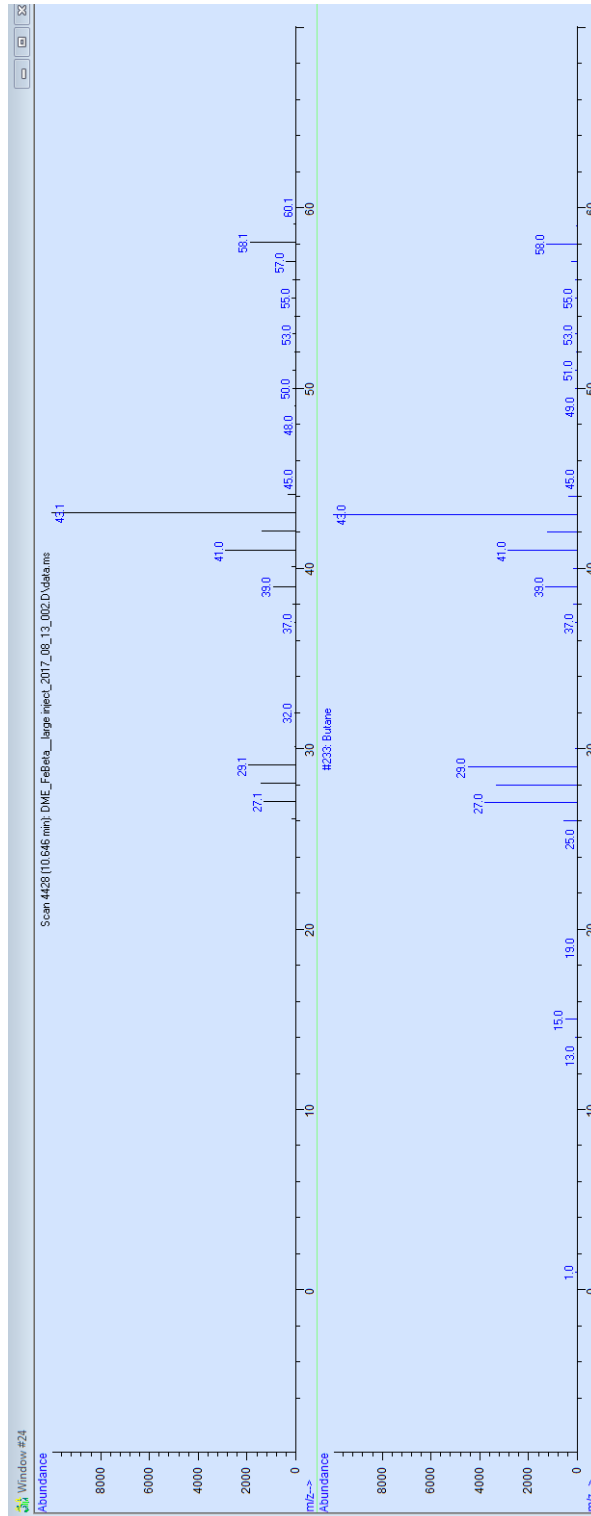


Figure C.4: Mass spectrometer fragmentation pattern for *n*-butane peak

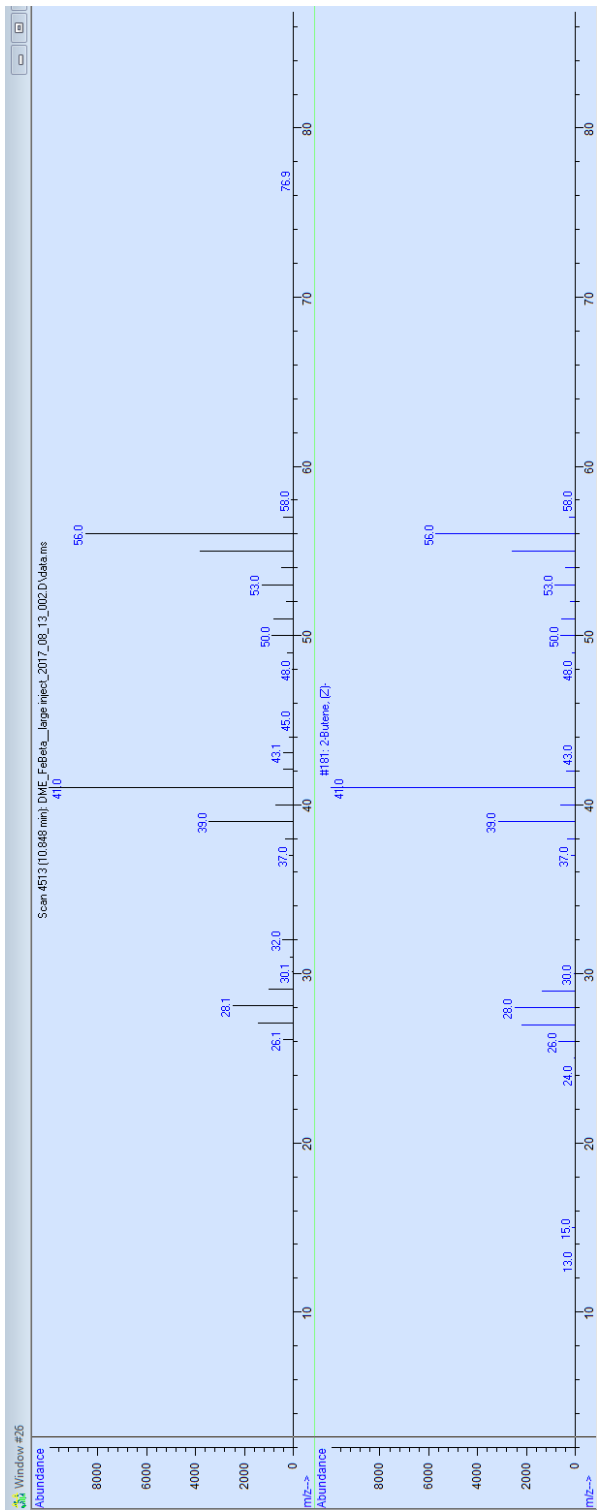


Figure C.5: Mass spectrometer fragmentation pattern for 2-butene peak

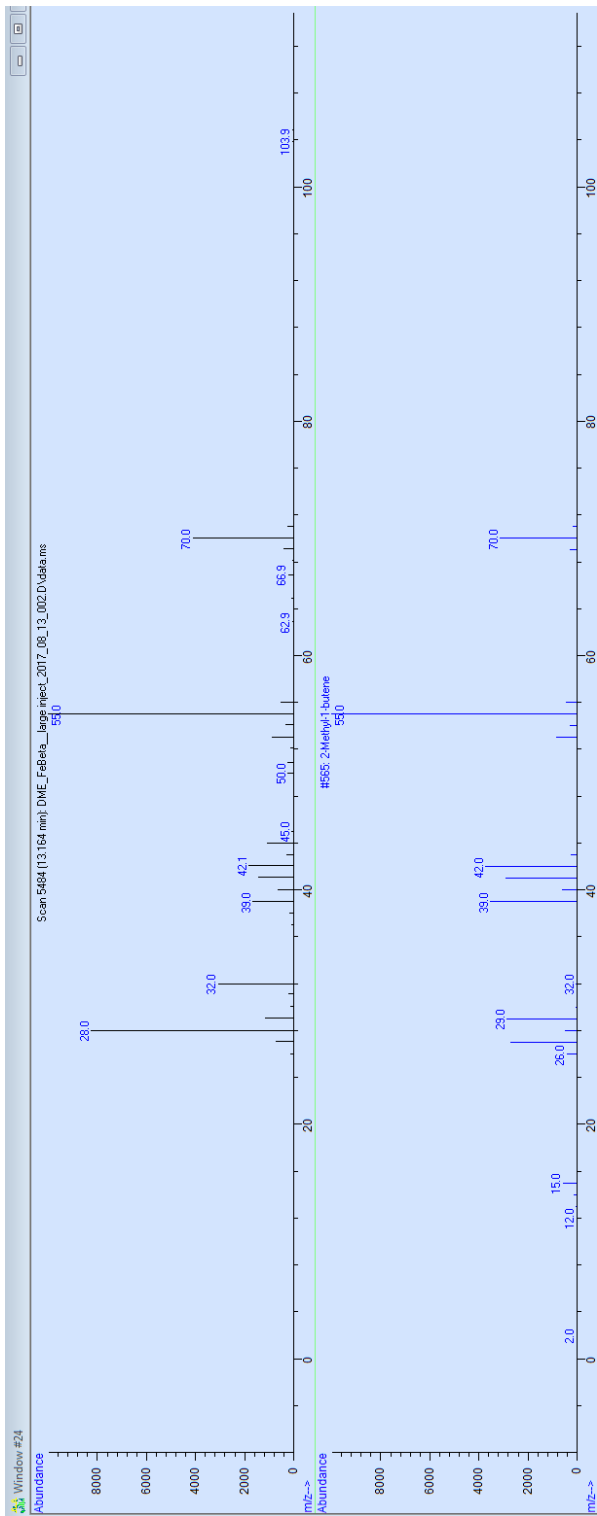


Figure C.6: Mass spectrometer fragmentation pattern for 2-methyl-1-butene peak

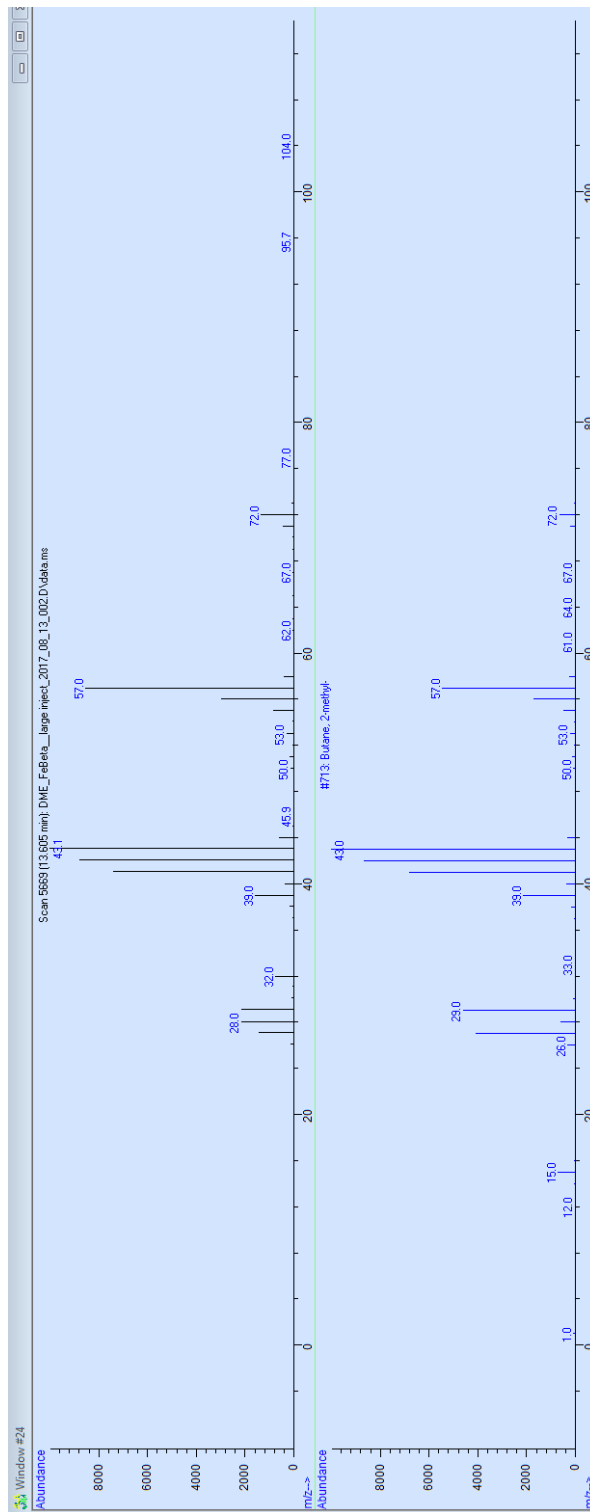


Figure C.7: Mass spectrometer fragmentation pattern for 2-methylbutane peak

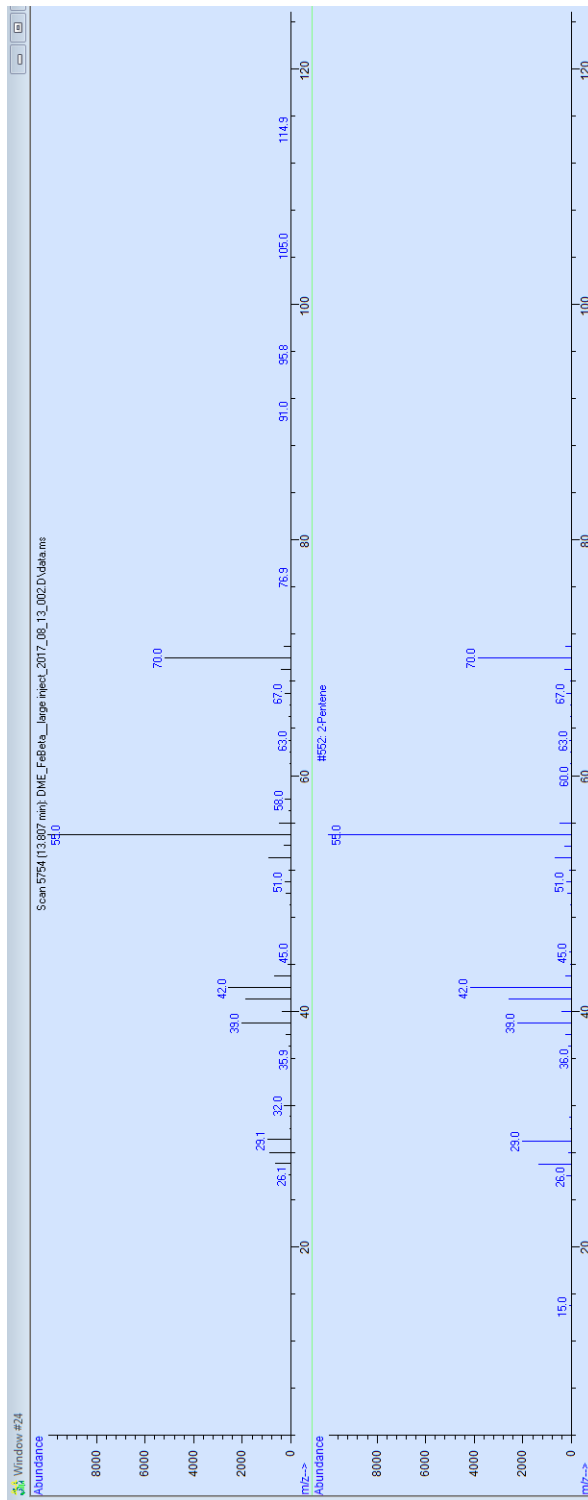


Figure C.8: Mass spectrometer fragmentation pattern for 2-pentene peak

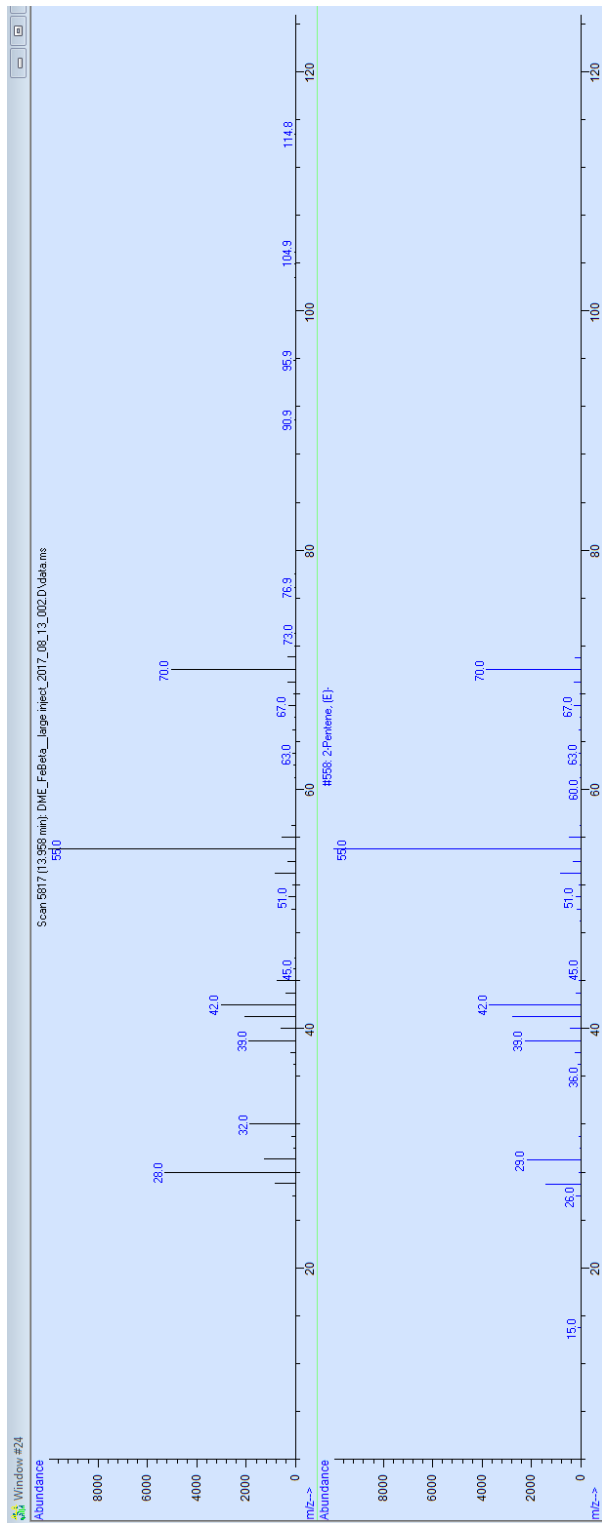


Figure C.9: Mass spectrometer fragmentation pattern for 2-pentene peak

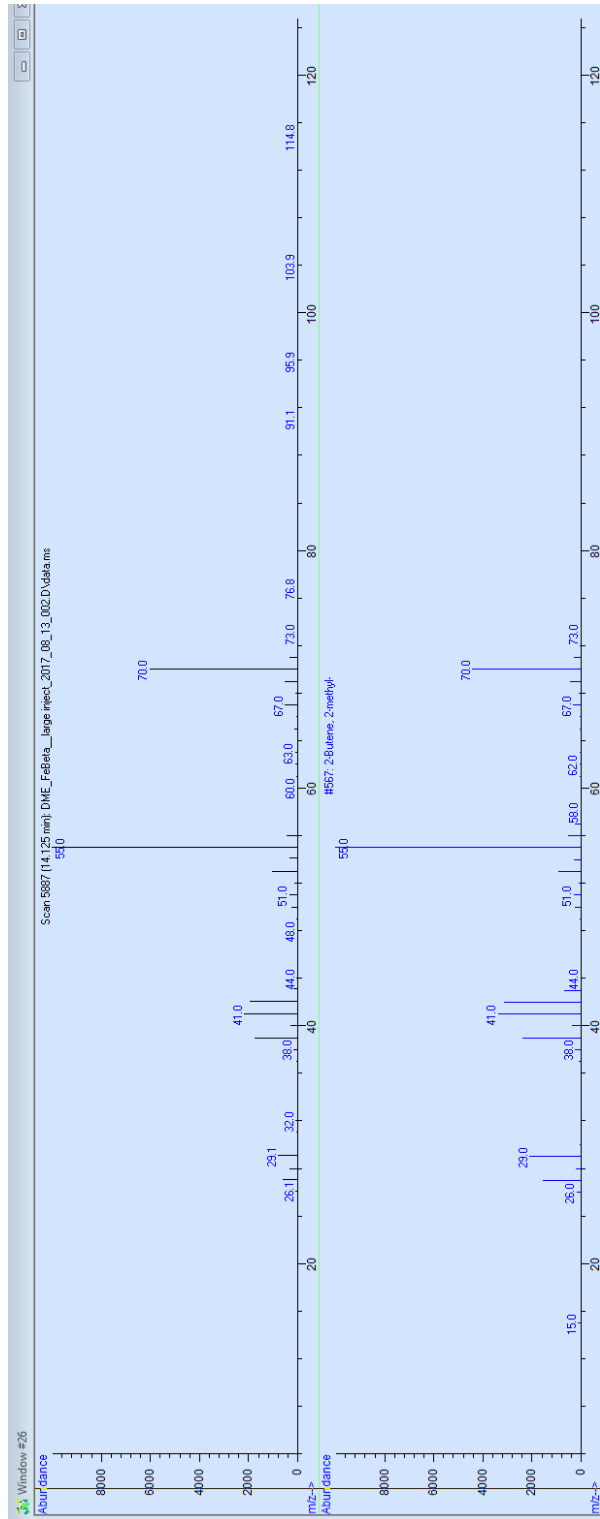


Figure C.10: Mass spectrometer fragmentation pattern for 2-methyl-2-butene peak

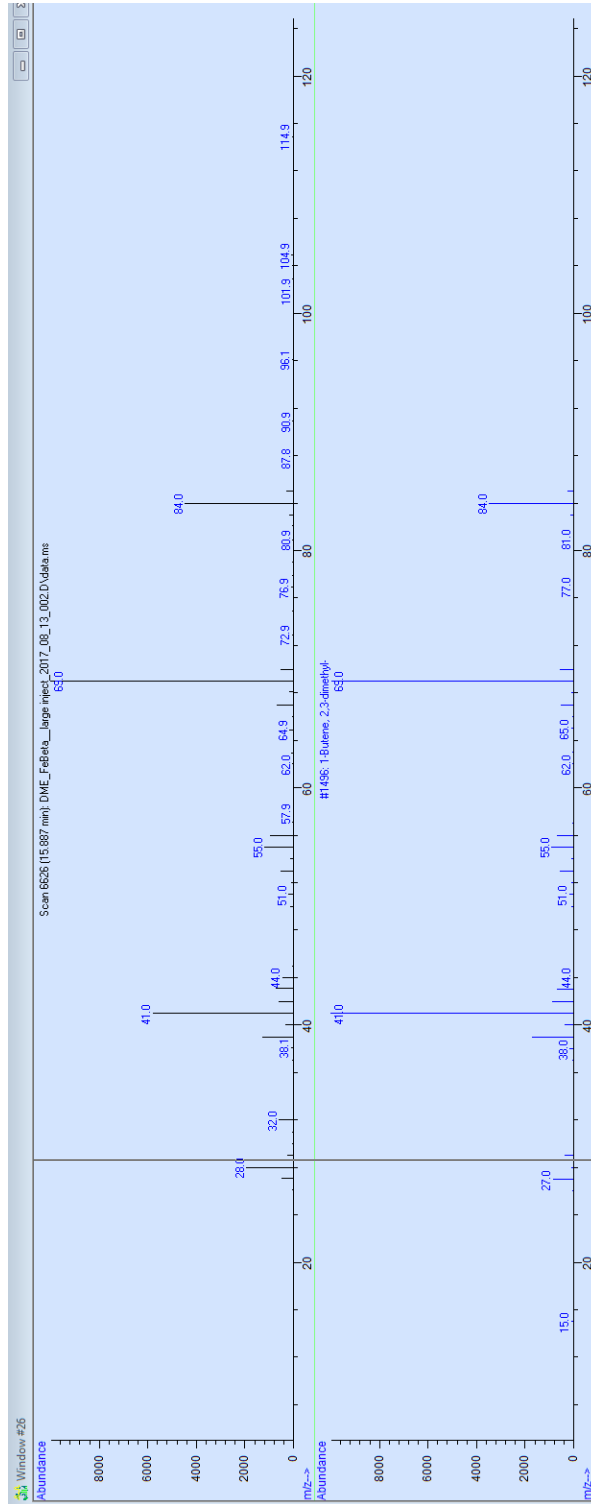


Figure C.11: Mass spectrometer fragmentation pattern for 2,3-dimethyl-1-butene peak

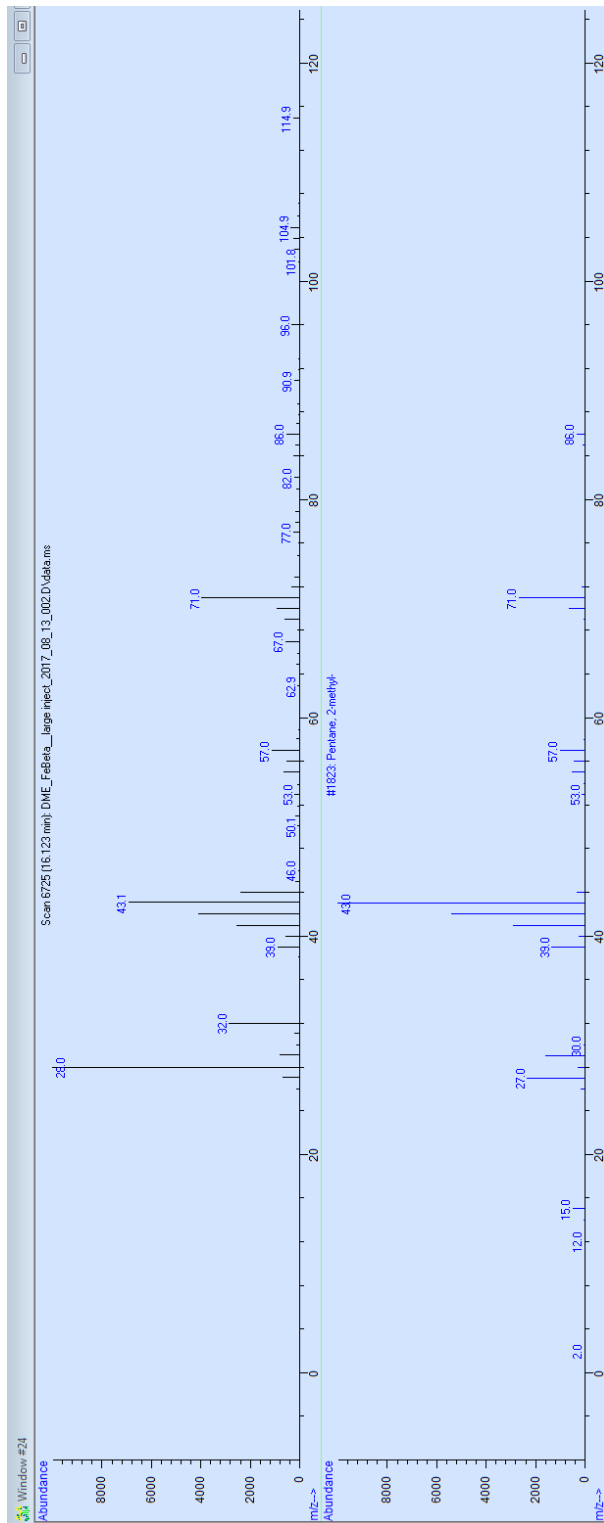


Figure C.12: Mass spectrometer fragmentation pattern for 2-methylpentane peak

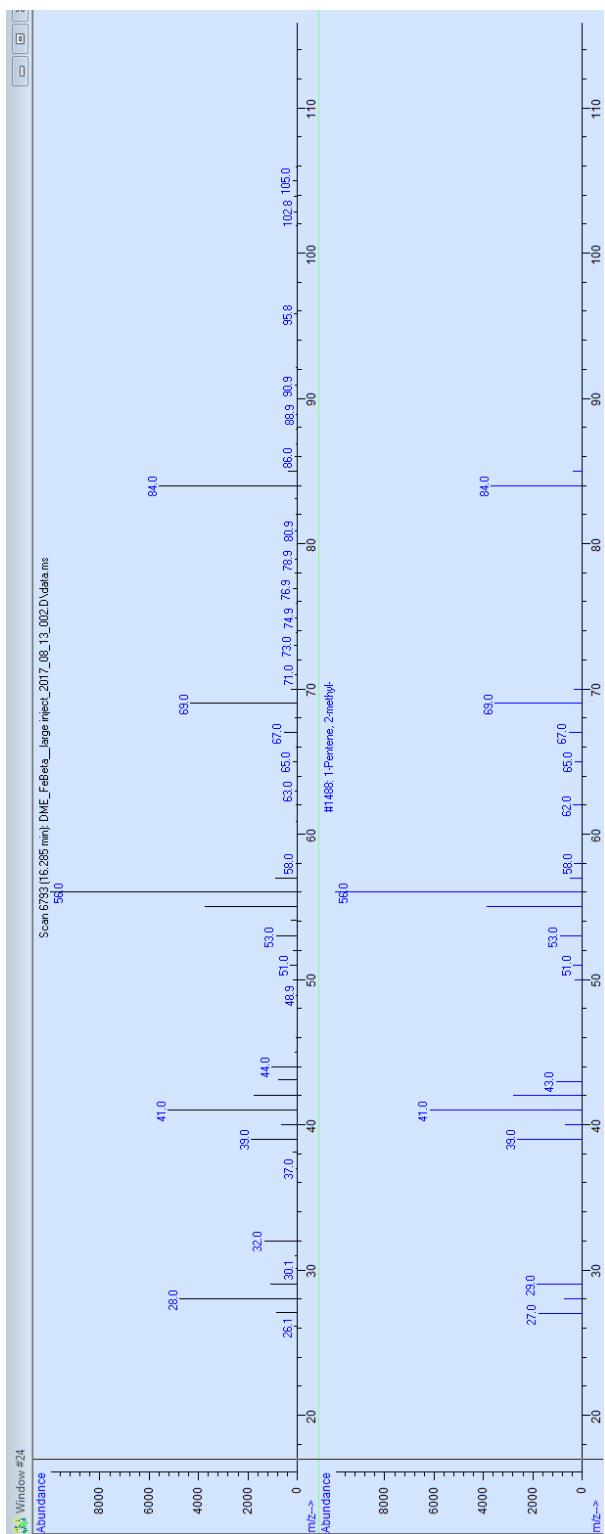


Figure C.13: Mass spectrometer fragmentation pattern for 2-methyl-1-pentene peak

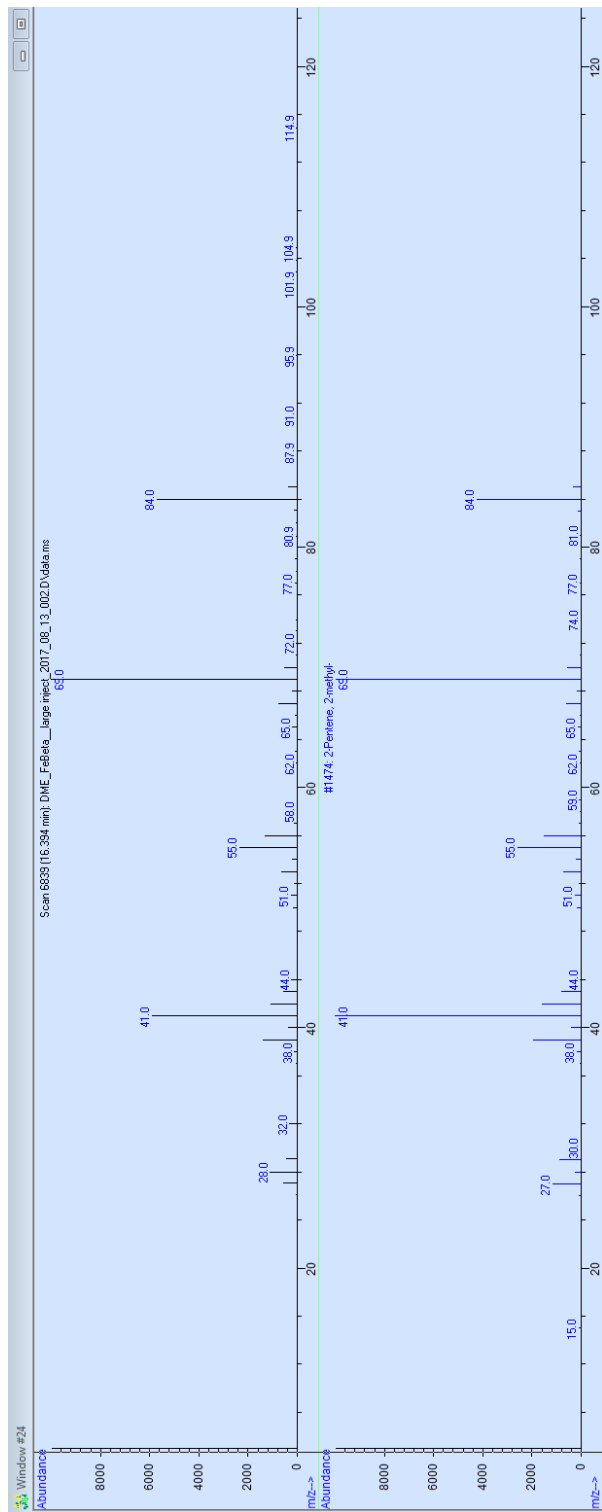


Figure C.14: Mass spectrometer fragmentation pattern for 2-methyl-2-pentene peak

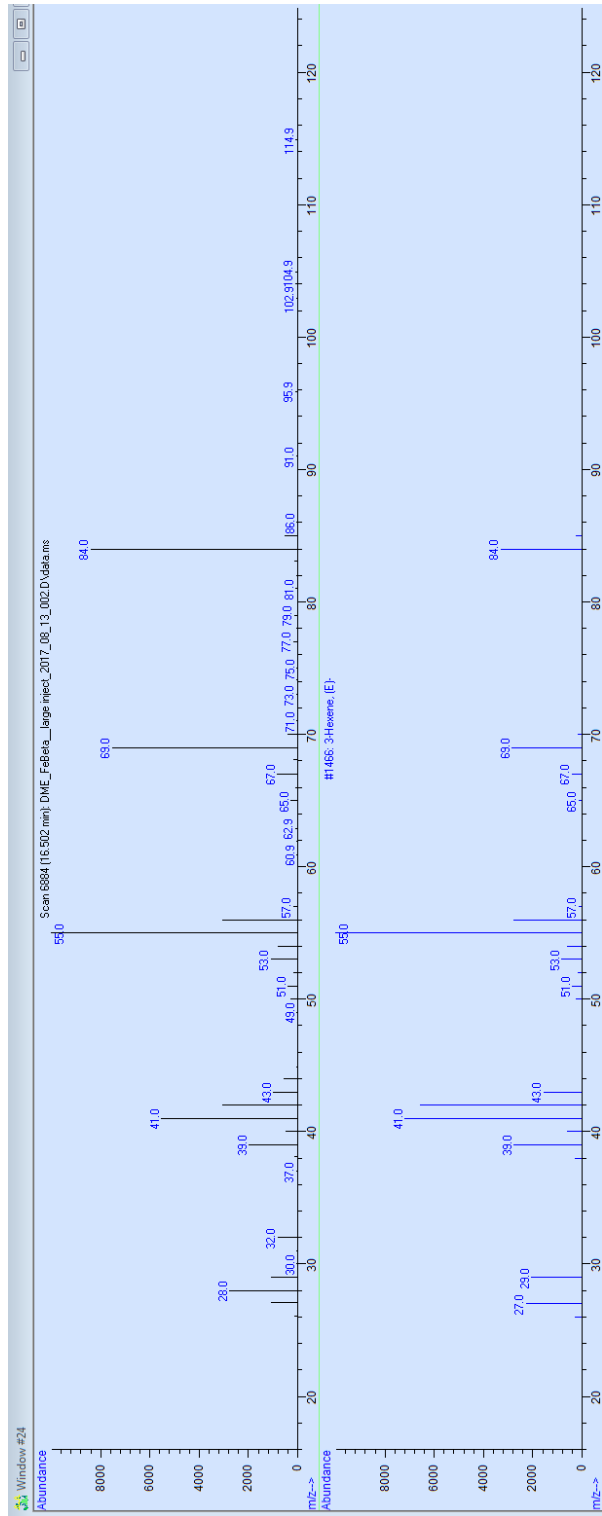


Figure C.15: Mass spectrometer fragmentation pattern for 3-hexene peak

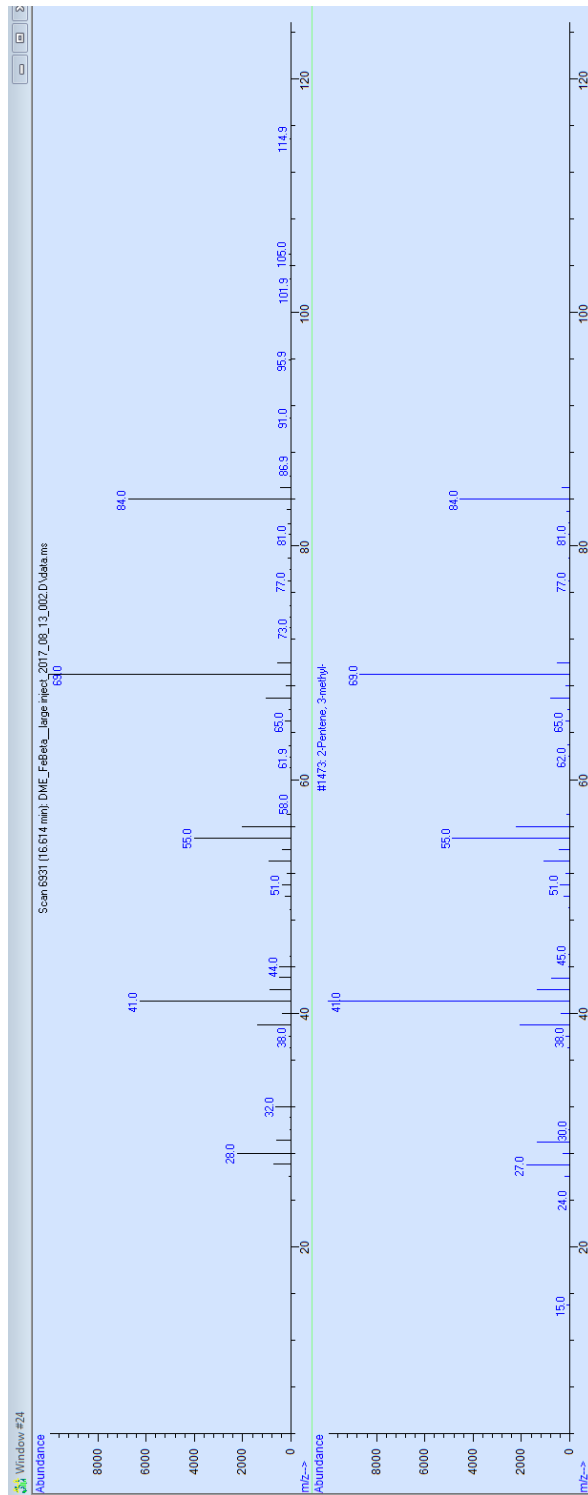


Figure C.16: Mass spectrometer fragmentation pattern for 3-methyl-2-pentene peak

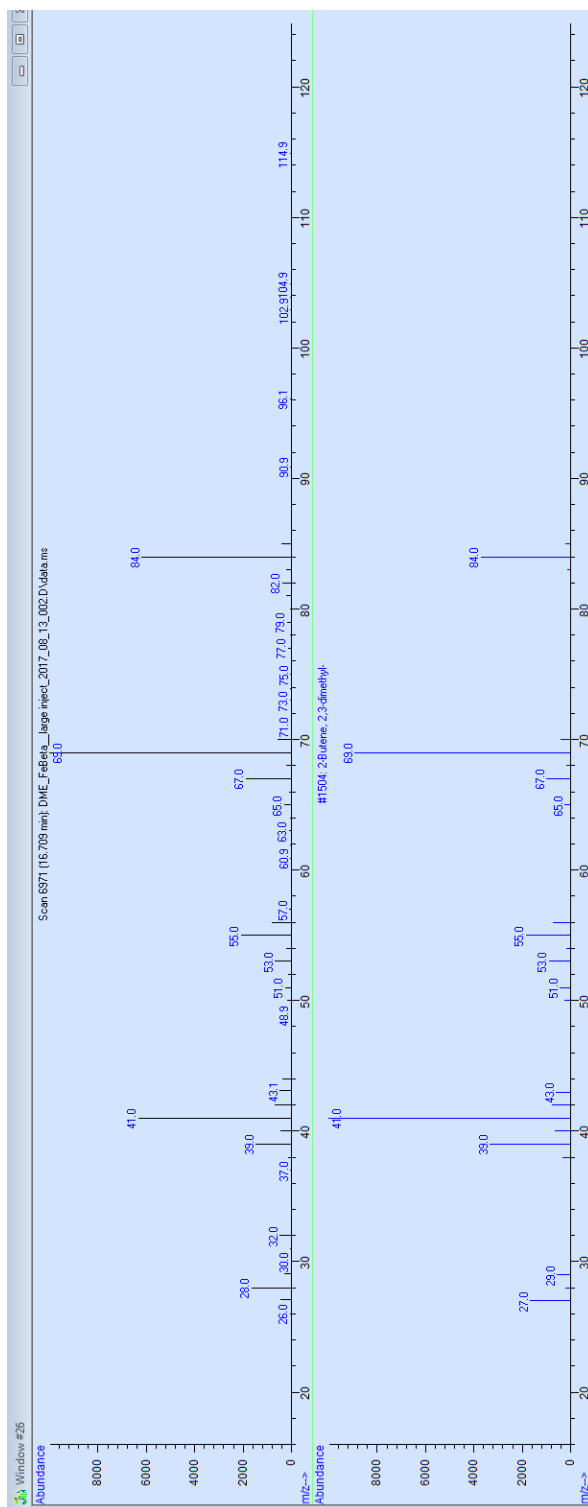


Figure C.17: Mass spectrometer fragmentation pattern for 2,3-dimethyl-2-butene peak

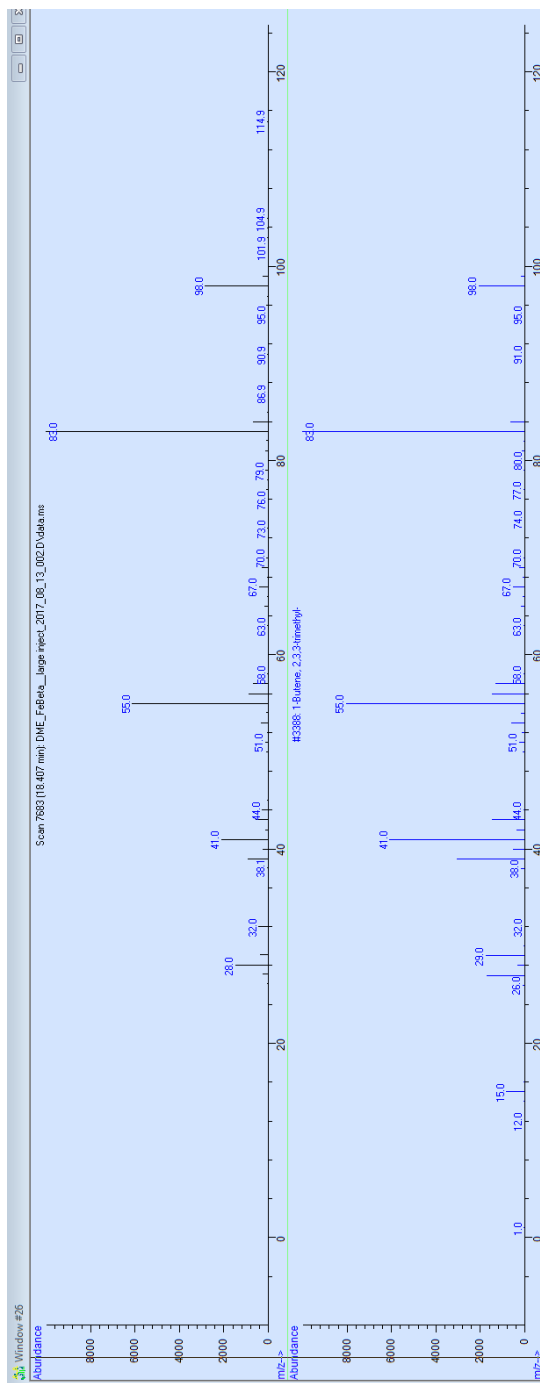


Figure C.18: Mass spectrometer fragmentation pattern for 2,3,3-trimethyl-1-butene peak

## **Appendix D**

### **REPRODUCTION OF MATERIAL RIGHTS**

*Catalytic n-pentane conversion on H-ZSM-5 at high pressure* [98] reproduced by permission of The Royal Society of Chemistry (RSC) on behalf of the Centre National de la Recherche Scientifique (CNRS) and the RSC.